To the Graduate Council:
I am submitting herewith a thesis written by Ryan C. Savery entitled "A Computational Analysis of Hypersonic Store Separations." I have examined the final paper copy of this thesis for form and content and recommend that it be accepted in partial fulfillment of the requirements for the degree of Master of Science, with a major in Aerospace Engineering.

Dr. James G. Coder, Major Professor

We have read this thesis
and recommend its acceptance:

Dr. Phillip A. Kreth

Dr. Devina P. Sanjaya

Accepted for the Council:

Dixie Thompson

Vice Provost and Dean of the Graduate School

To the Graduate Council:
I am submitting herewith a thesis written by Ryan C. Savery entitled "A Computational Analysis of Hypersonic Store Separations." I have examined the final electronic copy of this thesis for form and content and recommend that it be accepted in partial fulfillment of the requirements for the degree of Master of Science, with a major in Aerospace Engineering.

Dr. James G. Coder, Major Professor

We have read this thesis
and recommend its acceptance:

Dr. Phillip A. Kreth

Dr. Devina P. Sanjaya

Accepted for the Council:

Dixie Thompson

Vice Provost and Dean of the Graduate School

(Original signatures are on file with official student records.)

A Computational Analysis of Hypersonic Store Separations

A Thesis Presented for the

Master of Science

Degree

The University of Tennessee, Knoxville

Ryan C. Savery

August 2023

To all those who provided love and support which allowed me to grow and persevere even through the most difficult moments.

Acknowledgements

I would like to thank Dr. James Coder and my other colleagues in the VolAIR lab for providing a warm welcome and support during my time at The University of Tennessee. Their help developing and running codes along with distilling results and understanding concepts was invaluable to the completion of this document.

Abstract

Many current hypersonic vehicles involve shrouds, fairings, boosters, or ejectable payloads separating during flight. It is imperative that they do not strike each other after separation as this typically results in damage or loss of vehicle. This requires a detailed understanding of the flow features involved such as shock waves, expansion waves, shock reflections, and shock wave boundary layer interactions influencing the vehicles' attitude and trajectory. Experimental and flight tests of these scenarios are costly and need massive infrastructure which require difficult measurement techniques to characterize the flow field. Alternatively, numerical simulations can provide accurate, low-cost, and efficient predictions of hypersonic separations.

This study looks at the scenarios of a smaller vehicle or store in the flow field of a larger vehicle. Computational fluid dynamics simulations are performed on a 7° cone crossing an oblique shock wave at Mach 7 using NASA's OVERFLOW 2.3e Reynolds-averaged Navier Stokes solver. Trajectory and attitude is tracked along with capturing flow features and their imposed forces. The vehicle's dynamics when passing through a shock appears to predominantly the result of differential flow incidence angles causing a strong shock leading to a large pressure increase over a fraction of the vehicle which influences pitch. The vehicle appears to follow conventional longitudinal stability theory and becomes more stable during the interaction with the center of pressure moving aft and the peak pitching moment happening when the shock passes through the center of gravity if allowed to continue through the body. Complex shock wave boundary layer interactions are seen which could complicate specific separation scenarios. Nonphysical anomalies are seen in the flow field which are theorized to be the result of OVERFLOW's implicit solution algorithm but are shown to have little influence on results. Likewise, the applied forces and moments along with center

of pressure in this scenario are shown to be unaltered by hybrid Reynolds-averaged Navier-Stokes and Large eddy simulations in the form of delayed detached eddy simulation.

Table of Contents

Nomenclature

A	area
a	speed of sound
AoA	angle of attack
C_f	force coefficient
C_m	moment coefficient
CoG	center of gravity
CoP	center of pressure
e_0	total energy
ρ	air density
F	force
I	moment of inertia
m	mass
M	Mach number
P, p	pressure
C_p	pressure coefficient
Q	dynamic pressure ($\frac{1}{2}\rho V^2$)

Re	Reynolds number
T	temperature
t	time
ν	kinematic viscosity
V	velocity
ω	rotational velocity
u_i	velocity component
L	vehicle length
τ	shear stress
y^+	wall-normal non-dimensional grid spacing
x, y, z	Cartesian coordinate components

Subscripts

$_{ref}$	reference quantity
$_\infty$	free stream reference

Chapter 1: Introduction

Hypersonic vehicles fly in the most extreme conditions with high dynamic and thermal loads under complex flow fields. Speeds above Mach 5 are a necessity for space travel and beneficial to the modern war-fighter as they are a property of returning vehicles to and from orbit and/or used to quickly deliver integrated or separated packages to a location. Many current hypersonic vehicles involve a main vehicle with components separating during flight that present a number of simulation challenges such as shock-shock interactions, highly nonlinear interactions, and shock wave-boundary-layer interactions. These aerodynamic phenomena influence the attitude and trajectory of each object which needs to be understood before large scale experiments can be run. The single body case has been studied extensively [1–3] while having a smaller payload (or store/child) delivered from a larger vehicle (or parent) is relatively understudied. This process of detaching a child vehicle from a parent vehicle is known as store separation. A classic example of store separation can be seen in Fig. 3 showing a GBU-31 munition separating from an F-18c.

Strong shocks and complex flow features close to the vehicle's surface along with highly integrated propulsive elements dictate the design and geometry of hypersonic vehicles. An example of a hypersonic test vehicle can be seen in Fig. 1 showing NASA's Hyper-X/X-43A Research vehicle which used an integrated propulsive element underneath the vehicle. The fore end of the vehicle can be approximated by a wedge creating an oblique shock wave and the aft end approximated by a expansion corner. The X-43A uses horizontal and vertical stabilizers for static stability and control which also induce shocks and expansions into the flow field. Store separations will need to pass through these features and it is fundamental for the child and parent vehicles to not make contact after separation which could cause catastrophic damage or loss of one or body vehicles. Early efforts for subsonic aircraft [4] were able to use a combination of flight and wind tunnel tests to understand the trajectory after release as the force of gravity was greater than any lift force which could cause the store to move upwards after release. As speeds increased into the transonic, supersonic, and hypersonic regime, payload/vehicle configurations are more complex and the applied forces

on the store become great enough to overcome any gravitational force; these are the driving factors determining trajectories. The store's attitude is influenced by unbalanced forces and moments acting on the body caused by flow field features (boundary layers, shear layers, shocks, and expansions for example) along with the stability characteristics of the vehicle [5, 6]. Store carrying location plays a major role in determining these factors which can be split into two categories: external carry with the store typically carried underneath the wing or fuselage of the parent vehicle and internal carry where the store is typically held within a cavity in the fuselage of the parent covered with doors which are opened for release.

Stores are typically axisymmetric shapes that are statically stable in free flight meaning the attitude of the vehicle will restore with no control inputs if its angle is slightly perturbed [7]. Static stability is a product of the center of gravity's (CoG) location relative to the neutral point (NP), or the point where the aerodynamic moment does not change with pitch angle relative to the flow or angle of attack (AoA). A Statically stable vehicle has the CoG location forward of the NP. The corrective force returning the vehicle to its neutral position can be characterized by the static stability margin which is based on the distance of the NP from the CoG to the total vehicle length. A positive stability margin would indicate a stable configuration returning to neutral if disturbed where a negative margin would indicate an unstable configuration. A zero stability margin indicates the vehicle is statically neutral or no moments are applied to the vehicle from the flow in free flight. The aerodynamic forces (lift, drag, and side) act through the center of pressure: the average point where the total surface pressure acts on the body. Depending on the geometry of the vehicle, the the CoP can change with AoA. Because this study is interested in the fundamental forces acting on the vehicle apart from influencing flow features, it is advantageous to decompose the stability forces from the applied forces. Conical bodies have been experimentally and numerically shown [8, 9] to have an unchanging CoP with AoA at supersonic speeds where the shock is attached to the apex of the cone. In this case, the CoP and NP are essentially at the same location while in free air. This makes conical bodies a good candidate as all moments on the vehicle will theoretically be the result of flow features not found in free air.

Hypersonic vehicle stability and control properties can vary from lower speed vehicles in a number of ways [5]: The CoP changes relatively little with changes in AoA and altitude;

maximum lift to drag ratios are small typically in the 1-5 range and are nonlinear with AoA; and stability margin is a less effective measure of true vehicle stability. Contrary to popular dynamics theory, when examining a two stage to orbit hypersonic wave-rider, Johnson et al. [6] showed that, "air vehicles flown with significant levels of static instability indicated that the conventional static margin is not a valid indicator for these vehicles. In one case, 30% unstable was flyable, while in another 15% unstable was completely unacceptable. Many of the differences are due to the strong shocks near the surfaces and effect vehicles of all shapes, not just conical geometries." Atmospheric properties can also play a role in determining the controllablility of vehicles with ground tests not reflecting actual flight aerodynamics making accurate predictions difficult even for free flight and wind tunnel due to flow property constraints.

Analyzing hypersonic vehicle configurations using wind-tunnels and flight tests require an immense amount of infrastructure, time, energy, and money. While these methods are needed for flight vehicles, use of simulations tools such as computational fluid dynamics (CFD) and six degree-of-freedom (6DOF) rigid body dynamics codes allow for reduced-cost testing while capturing high fidelity data. Starting in the late 1970s and early 1980s CFD methods were able to capture the flow field around a representative vehicle and store configuration of the time [10, 11] and have since improved greatly providing more accurate and efficient codes capable of simulating the current hypersonic vehicles of interest. These combined CFD/6DOF simulations have been shown in low speed external store separation test campaigns [12] to be accurate but late stage vehicle designs should still be combined with experimental flight tests to verify these models. Cenko [13] has shown that an, "Integrated Test and Evaluation" approach, depicted in Fig. 2, provides adequate and efficient feedback where all three approaches improve each other. However, collaborations of this scale can only be done with the large budgets allotted for production flight vehicles.

1.1 Research Overview

In order to gain a better understanding of the fundamental dynamics, this study will focus on a CFD analysis of simplified hypersonic store separation scenarios. First, it will analyze

the scenario of a store passing downward through an oblique sock wave. This scenario is representative of a few possible situations where an understanding of the vehicles applies force and moments along with it's trajectory is crucial: an internal store held within the parent vehicle's fuselage crossing the shock created off the leading edge of the parent; an internal store ejected out of the rear of a parent vehicle and crossing the recompression shock; or a vehicle separating a subset (e.g. stage separation or a vehicle bifurcating.) Because this study is focused on fundamental interactions and is not vehicle specific, a flowfield with a generic 20° oblique shock wave is used to eliminate the influence of any additional flow features created by the parent vehicle. This case is analogous to a store or shroud separating and passing back through the bow shock of a vehicle or shock created from a control surface or vehicle appendage. To identify the forces applied to the vehicle apart from the stability forces, a 7° cone with a sharp leading edge is chosen as the applied forces from the shock are easily dissociated forces found in free air. The cone's half-angle is also chosen for its ubiquity in hypersonic studies. Scenarios in this study are specifically selected to not represent any real world vehicle which could be used, but to generically quantify the associated phenomena. It is also selected to be easily repeatable by future computational studies or experimental tests.

NASA's OVERFLOW 2.3e [14] CFD code is used to preform simulations using the time-accurate Reynolds-averaged Navier-Stokes (RANS) equations combined with an integrated 6DOF rigid body dynamics solver to output the vehicles position and attitude. Force and moment coefficients are tracked along with the flow field quantities. These are analyzed to gain a better understanding of the process in order design and predict future hypersonic vehicles. This study will accomplish the following objectives:

1. Discretize the vehicle geometry and preform a simulation in free flow from 0° to 45° AoA to verify its stability characteristics against theory and experiments.

2. Preform a dynamic simulations where a store crosses an oblique shock wave and analyze the attitude and trajectory data along with force and moment coefficients.

3. Examine the sensitivity of the scenario to changes in initial attitude.

4. Discuss influential factors for the store separation process.

5. Analyze the numerical assumptions and constraints associated with hypersonic store separations.

There are a few singular studies on hypersonic store separations [15, 16]; however, the techniques used in these are dated and an understanding on applications of current numerical methods applied to a hypersonic store separation scenario is not currently openly discussed in literature. State of CFD techniques including high order flux schemes, shock capturing mechanisms, hybrid Reynolds-averaged Navier-Stokes/large eddy simulations, and implicit algorithms will be used to analyze the dynamics of a store separation scenario, and consequently, the dynamics of a hypersonic vehicle passing through a shock where the surface will encounter differential flow incidence angles. The force, moment, and trajectory data produced during this study is not currently available and could be used for subsequent experimental tests or as a high resolution validation for any reduced fidelity methods. An analysis of current numerical methodologies can also guide future studies on the subject by showing when to expend computational cost for higher fidelity simulations and when the increased resolution is not needed. Overall, this study will provide an analysis of hypersonic store separations which is not currently available.

Chapter 2: Background

For some flight vehicles, it is advantageous to carry payloads which will separate from the carrier (or parent) vehicle during flight; this process is known as store separation. Stores can be carried by the vehicle externally, typically underneath the wing or fuselage, or internally to reduce drag or load limits. These stores are typically ammunition, fuel tanks, capsules, adversarial devices, or a combination thereof. It is critically important to understand the flow physics and body dynamics surrounding this process as a collision between the store and carrier vehicle can lead to a loss of both. To safely integrate stores, there is a need for predictable, fast, and accurate methods of simulating and testing trajectories. Preflight and inflight consideration of store separation can be done in a few different ways: wind tunnel tests, computational fluid dynamics analysis, and progressive flight tests. It is important for these analyses to resolve the structural, aerothermal, flutter, performance, stability, control, ballistics, and separation dynamics of the system in order to quantify the entire separation process.

2.1 Early Store Separation Predictions

Some of the earliest examples of store separation can be dated back to the early 1900s prior to World War I where grenades were thrown from the open cockpits of airplanes [17].This was done haphazardly with no need to consider possible collisions due to the low relative mass and velocities of the day. Preflight consideration and testing of stores was not preformed until around World War II , however, this was typically done to test the store effectiveness or to set sights used for accurate delivery [17]. It was only after World War II with the introduction of jet engine aircraft which could carry large payloads under their wings and fuselage that preflight testing became a necessity to guarantee a safe ejection. The need for analysis was also amplified as planes approached the transonic barrier where flow around the vehicle was not exactly known. The earliest flight tests focusing on body dynamics and collisions were done in a "hit or miss fashion" where stores would be dropped from the aircraft at gradually increasing speeds until the store finally came too close for comfort or actually hit the carrier

vehicle, sometimes causing a loss of one or both vehicles [13]. Predictably, test pilots were reluctant to fly in these test programs and engineers sought to develop safe techniques for analyzing store separation.

One of the first store separation analysis techniques developed was the Captive Trajectory System (CTS) for wind tunnel testing created by the Arnold Engineering Development Center (AEDC) in 1968 [18]. CTS typically uses a scale model of the parent aircraft with the store attached to a movable sting which is able to use the wind tunnel as a six-degree-of-freedom (6DOF) function generator to determine the aerodynamic coefficients of the store. An example of CTS hardware at AEDC's Tunnel 4T can be seen in Fig. 4. CTS was an improvement to the previous trial-and-error methods and went on to support many store integration programs, but it was not without it's limitations. Due to size constraints, many of the tunnel models were relatively small compared to flight articles which could cause predictions to not match flight tests. To exacerbate the issue, there was little effort to quantify the trajectory errors between the wind tunnel and flight tests to resolve the discrepancies as groups conducting the CTS wind tunnel tests were typically separate from the flight test division which would determine the save separation envelope [13].

Another issue of the time was the dissociation between weapon contractors, which preformed separate analysis to ensure a clean separation, and the aircraft contractors. Collaboration between the two typically ended when the aircraft contractors entered the flight test phase and no further analysis was done on the store separation prediction methodology to improve their accuracy. In addition, the separate weapons contractors used different methodologies to predict safe separation events disallowing the share of information. The Naval Air Systems Command (NAVAIR) decided to respond by creating a processes to analyze store separation flight test programs and employ the best techniques contractors had to offer at the time [19]. Resulting programs used an integrated approach combining preflight analyses, wind tunnel, and flight test data (ideally managed by one group) to inform each other and provide accurate and less costly store separation predictions. The final goal was to have trajectory simulations match flight tests to allow safe and consistent separations [4].

During the late 1970s, the Influence Function Method (IFM) was developed allowing for predictions store loads with regard to the carrier aircraft flowfield impingement [20]. IFM uses previous wind tunnel data from another store in the same flow field to predict the forces and moments of a store of interest. This is done by using a grid survey of static force and moment data (an approach conventional for the time) and parameter identification analysis to determine the localized angle-of-attack distribution in relation to the carrier aircraft. IFM could be used for subsonic to supersonic flight speed and provided predictions in good agreement to wind-tunnel tests of the time; however, it was not widely accepted and was not used in an integrated and evaluation approach.

Wind tunnel testing took a "grid method" approach assuming the free stream aerodynamics are solely a property of the store while the carrier vehicle's aerodynamics are mostly a function of its own flow field [19]. The aerodynamic interference between the two is assumed to only be a minor influence on the system. Store loads at a certain orientation would be subtracted from the total loads at the same orientation in a grid under the carrier vehicle in order to get the incremental aerodynamic coefficients. If values of the store load are known while still attached the aircraft, a six-degree-of-freedom (6DOF) solver can be used to calculate the stores updated position and attitude over some time step. The incremental grid coefficients are then added to the free stream values at the updated orientation and used to calculate updated aerodynamic coefficients. this process is iterated until the store is no longer in the vicinity of the carrier vehicle.

Around the same time as the introduction of CTS, numerical solutions based on linear theory and potential flow were being developed. While accurate potential flow codes existed, they were always backed/validated with wind tunnel tests and required enormous computational resources. Computational fluid dynamics (CFD) approaches also started to be able to handle the complexities associated with store separation from a vehicle during this time, however, due to the limited computer resources and linear computational techniques, the complex simulations were too costly to be a viable option. The introduction of the chimera grid scheme (technique of using multiple body-conforming grids to adapt finite-difference procedures to complex vehicle configurations)[11] in the early 1980s and updated computing practices would eventually lead CFD techniques to be invaluable for

test campaigns and hence have improved in both computational time and accuracy. The following sections will show the evolution of CFD standards to use time-accurate solvers to calculate the store's applied forces and moments combined with a body dynamics solver (typically a 6DOF module) to calculate the rigid-body equations of motion.

2.2 Flight Hazards

Before looking at computational methods and techniques to simulate store separation, it is important to understand the potential flight hazards so areas of interest can be addressed. Before the introduction of the fighter aircraft, stores were carried with the intention to pack as many as possible within bombers to maximize their effectiveness and were expected to clear the aircraft with the low flight speeds. These fighters carried stores externally on pylons similar to Fig. 5 where an F-16 carries a single store on an inboard pylon and multiple stores on the same outboard pylon. With jet aircraft reaching the transonic regime (above Mach 0.8) and carrying as many stores as possible, store/aircraft collisions became imminent. Purely gravity assisted releases were no longer possible leading to pneumatic powered ejection systems becoming commonplace. Some issues were alleviated or prolonged but with the increasing energetic systems, collisions remained risking loss of vehicles and stores. A study by AEDC Identified the three most common collision types: store-to-pylon, store-to-aircraft, and store-to-store [17].

Store-to-pylon collisions typically happen just after release when the aerodynamic pitch, roll, and yaw rates exceed those dictating the movement away from the pylon. These collisions typically happen just after ejection when the store is intentionally closest to the carrier vehicle. A collision here can result in damage to the pylon/release mechanism and/or the store itself. While this is minimal in the transonic regime and typically does not lead to a loss of vehicle, supersonic and hypersonic flow fields can create catastrophic damage to both vehicles. Stochastic trajectory studies have shown typical store-to-pylon collisions happen when the store is released and pitches nose-down causing the aft aerodynamic control surfaces to rise up and impact the pylon resulting in bending or breaking [12, 17]. This scenario can

cause the store to become unstable and follow an erratic trajectory which is unacceptable when working in close proximity to ground operations.

Store-to-aircraft collisions happen when stores impact the carrier aircraft after clearing the pylon and are typically on the wings, fuselage, or empennage. Because the store is allowed to gain speed relative to carrier aircraft, the collision is much more energetic and can cause serious damage to both vehicles. This type of collision needs special attention as it can be the most catastrophic. Stores must clear the vehicle's flowfield without significantly upsetting its attitude as to cause movement towards its carrier. It is also important for stores to clear in a timely manner as they can create strong aerodynamic and thermal loads from shock waves and turbulent wakes on the carrier as speeds increase into the hypersonic regime. An ideal ejection would push the store safely away at a slight nose down attitude allowing it to consistently accelerate away from the vehicle, however, this can depend on store shape and ejection mechanism [12, 17].

Finally, when multiple stores are carried or released at the same time, store-to-store collision avoidance needs to be addressed. This collision mechanism is becoming less common as vehicles are moving towards singular internal store release, but is still an issue on many modern delivery systems. There two main ways stores can collide with each other: side collisions on a simultaneous release and stores being released simultaneously or in quick succession so that the leading store is impacted by the following store while tracking in its wake. Depending on the intention of the store, these collisions can decide fuse timing as arming bombs immediately after release could cause premature detonation if contact is made [12, 17]. Likewise, if a store impacts another store still attached to a carrier vehicle, all the concerns of a store-to-aircraft collision apply.

These three collision mechanisms must be accounted during simulations or flight tests in order to ensure a safe release. Stores historically proven to be difficult to separate are low density, unstable, with folding fins, liquid filled, the jettison of fuel tanks, pylons, and racks along with quick succession (ripple) release of stores [17]. Aerothermal loads must also not be overlooked as speeds increase to supersonic and hypersonic as can be the primary design constraint of pylons, store covers, and the vehicles them self. A prime example of this oversight happened on October 3, 1967 where an X-15A-2 flew with a pylon mounted

experimental ramjet engine. As the vehicle reached a maximum velocity of Mach 6.70, the strong shock shock interactions caused damage to pylon, as seen in Fig. 6, eventually leading to the engine to separate and crash into the desert below [21, 22]. Finally, the accuracy of the store to its target location after clearing the parent vehicle must be analyzed to ensure that residual forces, moments, or upset attitudes can be account for.

2.3 Computational Fluid Dynamics Analysis of Store Separations

2.3.1 Subsonic and Transonic Flight

A CFD approach to simulate the complex flow fields associated with store separations first became feasible in the 1970s with the introduction of novel solution techniques. One of the fires numerical solutions was provided by the team at Nielsen Engineering & Research Inc. (NEAR) using a vortex lattice method to model the wings with the fuselage modeled by sources and doublets [23]. The store was put in the aircraft's flowfield and loads were calculated using slender body theory. This code allowed for timely predictions in good agreement with experiments and went on to have many improvements and a long service life.

In 1980 Cenko et al. published a paper describing the PAN AIR code: a higher order panel method to solve a variety of boundary value problems in steady subsonic or supersonic inviscid flows [10, 24]. With only minor simplifications, the group was successfully able to match subsonic numerical models to experimental tests accurately capturing the applied forces and moments on the stores. As speeds approached transonic, some corrections were necessary to account for a curved Mach line and local Mach number propagation effects. The PAN AIR code, however, took over a day to run on the supercomputer of the time (CDC 6600) making its use as part of a time dependant code out of the question and leading to hybrid techniques, like IFM, to be used. A combination of PAN AIR, IFM, and a 6DOF program were used to predict store trajectories for the F/A-18c and F/A-18E with results

in good agreement to tests, although, some small discrepancies were found in the yawing moment when looking at stores on the inboard pylons.

Later in the 1980s, It was becoming possible to solve the full potential, Euler, and simplified Navier-Stokes equations, like the thin-layer Navier-Stokes equations, with the advancement of computers and computing techniques along with novel numerical schemes. As Previously mentioned, the chimera grid technique [11] allowed complex geometries to be resolved with unsteady versions [25] and unstructured grid techniques [26] developed in the late 1980s able to handle the entire store separation process. Several efforts were done to validate CFD methods and employ them in external store certification campaigns by using a generic configuration of wing, pylon, and store. A computational grid for this is shown in Fig. 7. The first campaign was done in 1992 verifying wind tunnel tests on this specific configurations documented by Heim [27]. The Euler solutions were done by Newmann and Baysal [28] with thin-layer Navier-Stokes solutions provided by Meakin [29]. Both solutions were in good agreement with tests even in areas of high aerodynamic interference but compute times were on the order of days. A higher order, full-potential, code named TranAir was later developed by Madson [30] which could bring the computational time down to a fraction of the original allowing for routine use. Madson also showed that in the transonic regime, inviscid codes were not adequate to predict the wing and pylon flow field, but could handle the store loads and pressure fields. These studies also showed that while predictions were agreeing with wind tunnel tests, precise store pressure coefficients were difficult to attain with results being more qualitative than quantitative.

In the 1990s, the Office of the Secretary of Defense funded the Applied Computational Fluid Dynamics (ACFD) group and tasked them with creating CFD analysis tools that could certify store separations which would reduce the dependence on wind tunnel and flight-tests by the Department of Defense [19]. To encourage involvement, there were two challenges proposed by ACFD: challenge I was an analysis of an F-16 with a generic finned store and challenge II was for the F/A-18C JDAM configuration for two different release scenarios. The first challenge's results were heavily skeptic as flight test data was not provided and wind tunnel tests were questionable. Challenge II provided flight and wind tunnel tests at Mach 0.962 and Mach 1.05 with a dive angle of 45° and forced ejection. The conclusions

[31] showed that wind tunnel certification programs would still be needed as CFD solutions, while being just as accurate in most cases, were too costly with respect to time required. They found CFD analysis still had a place in the form of requirements definition and systems engineering trade-off studies that could reduce the risk of expensive redesigns after hardware was made. There was also a consensus that finer ejector/store interaction modeling was needed to accurately model the body dynamics. Challenge II did have some unanswered questions about the cost to benefit ratio of using simpler Euler simulations compared to Navier-Stokes solvers prompting a call for a third challenge which was not funded.

During this time, Lijewski and Suhs were also able to show the merits of a CFD approach [32] on a generic transonic wing/pylon/store configuration similar to that of Fig. 7 with the store having an additional aft cylindrical sting. They concluded that Euler simulations could capture all major motions of the store, although angular orientations and rates were not precise. Three sources of error were identified in their work: the inviscid nature of Euler codes resulted in errors in the x location of the trajectory, approximate modeling of the ejector sequence contributed to errors in the Euler angles and angular rates, and the quasisteady nature of wind tunnel data is different from time accurate computations.

Until the late 1990 most studies were focused on external stores for their simplicity, but with the introduction of aircraft like the F-117 and F-22, internal carry became a necessity. This was driven by military aircraft transforming from primarily air-to-air and air-to-ground attack vehicles to stealth reconnaissance and precise attack vehicles. The new generation of stealth vehicles required clean angular surfaces, most evident in the F-117 shown in Fig. 8, in order to evade radar detection and external carries would negate this design. As aircraft became faster pushing further into the supersonic regime, the drag and loads from an external store also helped in making internally carried stores more common. Internal stores are most commonly carried within the fuselage of the aircraft near the center of gravity (to maintain stable flight characteristics after separation) with movable doors covering the cavity. Internal stores introduce complex flows with strong gradients, shear layers, pressure fluctuations, and shock interactions in addition to clearance and ejection issues not seen with external carries making analysis difficult.

Atwood provided a study looking an actively controlled store ejected from a cavity at Mach 1.2 coupling the Reynolds-averaged Navier-Stokes (RANS) equations with rigid body dynamics and pitch-attitude control laws, all in two and three dimensions [33]. The study showed modeling could be done with good agreement to experiments but the same issues with minor quantitative differences persisted as well as computational times being unreasonable for rapidly changing designs. Load coefficients on the store were oscillatory as a result of turbulence coming from the the cavity/free stream shear layer which one can deduce could cause attitude variations depending on release time. These resulting stochastic trajectories will be addressed in future studies. In order to reduce the complexity of solutions and computational time, the AEDC took action around the same time to formulate approximations for computational trajectory predictions of stores released from a bay [34]. Several methods were identified which could reduce time from 5% to 70% but carried varied unknowns and risks associated with their use. They concluded that more studies would need to be done in order to fully understand the methods along with quantifying the aforementioned trajectory variances associated with release time.

Coleman [35] was able to present a study of fully time accurate inviscid store separation trajectory simulations in support of the F-111's flight test program. Unsteady carriage loads were monitored and multiple release times associated with the maximum and minimum aerodynamic loads on the store were chosen. Although they used a large ejection velocity, causing an artificial insensitivity to aerodynamic loads, it was shown that translation was only slightly effected by release time, but the orientation showed a large sensitivity. Additionally, Freeman et al. [36] Provided a report on fully viscous, time accurate GBU-12B gravity separation trajectories from a B-52H. They showed by varying the release time, large variances in the store trajectory and attitude, shown in Fig. 9, were possible. The only difference in the four stores in Fig. 9 are the relative position of the unsteady weapons bay flowfield and shear layer at release. Other studies [37] have shown this phenomenon exists in wind tunnel tests as well. Roughen et al. [38] sought to capture unsteady effects using databases of steady and unsteady aerodynamic information to determine probability distributions of significant events in a program named Rapid Unsteady Store Analysis Tool (RUSAT). Results were shown to have a reasonable correlation to tests with the explanations

for the discrepancies identified. External stores are not plagued by unsteady effects caused by cavity flows but varying trajectories depending on release time can still be possible. One example from Mizrahi and Raven [39] showed that wing elasticity can cause nonuniform ejection force vectors leading to, most significantly, a roll motion in the store.

The state of the art CFD approach to simulating subsonic and transonic store separations has been shown in the previous studies [19, 39] to be a viscous RANS equation solver using rigid body equations of motion in a 6DOF solver. Future approaches could include large eddy simulations (LES) or Hybrid RANS/LES techniques using a flexible body approach in the 6DOF solver but their feasibility have not yet been shown at the time of writing.

Transonic CFD trajectory studies date back to the 1970s allowing for over 50 years of lessons learned; many of these have been summarized by Keen et al., Perillo, and Atkins [4, 40]. One of the most important lessons is that trajectory simulations need to match flight tests. It has been shown multiple times that, while the CFD and wind tunnel tests are in good agreement, agreement between simulations and flight tests are less common. Other lessons include: not decreasing simulation effectiveness in the name of efficiency, properly modeling ejections and pylons, understanding the effect of restraint flexibility, matching aircraft flight maneuver conditions, using easily understandable data visualization techniques, confirming wind tunnel techniques are accurate, using proper dynamic motion approximations, accurately capturing complex geometry, capturing dynamic flow fields, and using integrated test and evaluation methodologies. As Stores become faster, more complex, smaller, and more maneuverable, the future store separation engineers will need a highly multidisciplinary knowledge base to be able to adequately understand the store separation process.

2.3.2 Supersonic and Hypersonic Flight

In the 1970s, around the same time as the emergence of subsonic and transonic CFD simulation techniques, prediction of supersonic store separation being worked on. While the physical process is similar, working in the realm of compressible fluids makes the challenge of accurately capturing the store's trajectory a much harder task.

In 1976, A team at Nielsen Engineering and Research, Inc. [41, 42] made an effort to take subsonic methods and extend them into the supersonic regime. Using generic aircraft and store shapes, they applied linear potential flow modeling to the aircraft components and adapted legacy methods used to predict flow before the store is immersed. These methods were tested against wind tunnel results and were found to be "generally good" [41] with respect to total forces and moments on the store. Their method did require corrections due to additional perturbations caused by multiple shock reflections taking place between the store and the wing along with making loading calculations three dimensional as the axial velocity gradients were too large to be accurate while using slender body theory. A succeeding report [43] would show improvements made to their methods as well as adding additional functionality to their code such as pylon ejectors and the capability to analyze stores of non-circular cross section.

Later, in 1981, Waskiewicz, DeJongh, and Cenko [44] applied panel methods to external tangent ogive stores with and without wings at Mach 1.5 and 1.9. Results showed an oscillatory behavior when the store was in close proximity to the carrier thought to be caused by either Mach wave reflection effects or a lack of resolution in the panels near the effected area. This study did show the that the previously discussed PANAIR code was superior to other codes of the time in predicting store forces and moments at supersonic speeds. During a similar time frame, Marconi conducted a study of interfering bodies in supersonic streams [45] by creating a finite-difference Euler flow solver using a novel shock fitting scheme able to predict complex interactive shock patterns. This study was done with the explicit intend to be used with externally carried stores. For his tests, he chose moderately supersonic flow (Mach 2) using an inviscid assumption which was found to be accurate enough as the viscous regions were confined to the boundary layers of each vehicle. It was also shown that the fluid mechanics of the system are dominated by the reflection of a shock system making detailed nonlinear calculations necessary. Effects of shock reflections on the store were found to be extremely sensitive. One important question that Marconi formulated that was unanswered, which would be the subject of his following papers [46], was how does a regular shock reflection transition into a mach disc. He concluded with some general recommendations to make future predictions more accurate: improvements should

be made to load distribution calculation methods, store-to-aircraft interference accounts, and flowfield prediction methods.

As a result of the extreme environment around an aircraft, internal store separation studies were of more prevalent at supersonic speeds than in the subsonic/transonic regime. 1983 saw one of the first experimental studies of finned supersonic stores separating from cavities by Stallings [47]. An important physical phenomenon identified was the effect of cavity depth to length ratio (D/L) had on the release characteristics. A $D/L = 0.088$ showed large interactions between the cavity and external flat plate causing unfavorable separation characteristics while a $D/L = 0.255$ had the flow over the place bridging the cavity and allowing for a satisfactory separation. These results match previous studies [48] into characteristics of empty supersonic cavities showing that the flow features found cannot be ignored if a store is also in the cavity.

In 1986, Baysal provided a report on the computational analysis of cavity flow fields with regard to store separation [49]. A notable flow feature identified around cavities include oscillations caused by a highly vortical shear layer at the upper corner of the cavity and counter rotating eddies near the bottom corners. The shear layer also has the the option of bridging over the cavity, usually seen with deeper geometries, or deflecting inwards and possibly reattaching with the bottom of the cavity. Oscillatory resonant effects were found to be caused by the fluid's compressibility, surface wave phenomena, and solid boundaries coupling with oscillations. Taylor-Görtler like vortices can also form around the cavity in zones between the primary eddy and downstream secondary eddy which resonates providing or extracting mass from the cavity. When combined, these oscillations can cause extreme forces on both vehicles along with altering stores' trajectories as they cross through the shear layer. Baysal's work in this report and later papers [50] also looked into two different mathematical models of the conservative Navier-Stokes equations with turbulence modeled algebraically: the line-Gauss-Seidel relaxation scheme and the MacCormack scheme. They showed that an upwind relaxation scheme is the best for overall efficiency.

Until the late 1980s, almost all supersonic store separation studies were done with flow less than Mach 4, however, as vehicles became capable, flow phenomenon in the hypersonic regime (above around Mach 5) were becoming of interest. Due to the extreme complexity

and cost needed to conduct real world experiments on hypersonic vehicles, CFD analysis was preferred. One of the first computational looks into hypersonic store separation was done by Chow and Marconi at the Grumman Corporation [15] using a Navier-Stokes solution based on the ARC3D code. Calculations required for a practical problem were shown to require many an excessive number of points and convergence was only possible for simple problems. Qualitative results could be had from their solutions with aerodynamic force calculations good enough for some engineering applications but similar issues to supersonic studies with capturing bow shock/boundary layer interactions and reflected shock waves still persisted. An impact theory methodology was also being investigated during the same time period by Newman et al. [16] for the aerodynamic coefficients with trajectories calculated using a 6DOF dynamics code. This method provided valuable engineering insights into high Mach number (Mach 10 through Mach 20) store separations but, like others, was not accurate in the near body region when the two vehicles are in close proximity creating a reflected shock systems. Hypersonic store separation was also being studied experimentally by a group at the General Dynamics Convair Division in collaboration with the Air Force Armament Laboratory [51]. This team looked at separation phenomenon of a store ejected from the aft plane of an axisymmetric vehicle launched from an light gas gun along with non-intrusive flowfield measurements techniques. They displayed that interferometry was a useful tool in correlating experimental data to CFD techniques.

Navier-Stokes based CFD solutions in the mid 1990s matured to the point of being a valuable tool for engineering design work of supersonic vehicles. During this time, major collaborative computational efforts and resources were being allocated toward understanding launch and reentry aerodynamics of the current space shuttle [52, 53] along with correlating previous X-15 hypersonic flight tests with current CFD methodologies [54]. This decision was driven by the United Stated demand for a reusable launch vehicle capable of providing routine and affordable access to space. The only vehicles capable were powered by rocket engines which were limiting as a result of the specific impulse limit of chemical rocket engines [55]. Airbreathing engines were desired as a single-stage-to-orbit (SSTO) airbreathing vehicle were thought to be able to lower costs significantly. The National Aero-Space Plane Program (NASP) was an attempt at a SSTO airbreathing vehicle, however, was canceled in 1995 due

to a lack of funding and increasing complexity. NASP was not a total loss as it provided methodologies and technology to manufacture a viable scramjet (supersonic combustion ramjet) engine along with other technologies for hypersonic flight. Scramjet engines were thought of as the answer to high specific impulse propulsion but needed a flight demonstration for wide acceptance leading to the creation of the NASA's Hyper-X program. The Hyper-X program would use a low cost hypersonic vehicle with an integrated scramjet engine which would be dropped from a B-52 and propelled by a Pegasus first stage in order to reach speeds necessary for engine ignition and operation. The separation analysis of the vehicle from the Pegasus booster is of interest to the store separation process as methodologies and data can be interchangeable between the two.

Baysal and Luo in the late 1990s provided some of the first Hyper-X separation studies [56, 57] preformed at or above Mach 5 using a dynamic unstructured mesh technique done as a proof of concept. They employed a finite-element method to solve the three-dimensional Euler equations combined with a 2 DOF trajectory simulation. A method for aerodynamic interference was created by solving static cases using prescribed motion then applying resulting interaction forces to test cases. Results showed a strong dependence of the unsteady forces and moments on aerodynamic interference between the two vehicles and appeared to be a highly nonlinear function of the separation distance. Issues were identified with their method including accounting for viscous effects and and studying realistic separation scenarios, but Baysal and Luo were able to show that this computational approach could be used to decrease the amount of ground and flight testing needed allowing for cheaper and faster analysis campaigns.

Buning et al. provide an additional computational study [58] in 2001 on stage separation of the Hyper-X which was correlated with a wind tunnel test campaign [59] to provide a extensive database. Both viscous and inviscid techniques were used to understand the unsteady effects and the impact of interference between the booster and research vehicle. Results showed that, while intense, the initial aerodynamic transients are short in duration. Analyses were shown to be possible for the interfering bodies and a quasi-steady modeling approach for separation aerodynamics was deemed appropriate. This study was also instrumental in understanding the accuracy available with inviscid and viscous

CFD techniques along with providing insights into expanding wind tunnel results into flight conditions.

An additional notable project to develop the computational analysis capability for unsteady, viscous, and hypersonic vehicles with internal store separation was published in 2001 from David Marcum [60]. Their method used an "advanced implicit high-resolution flow field solution algorithm" combined with a novel unstructured grid generation procedure called the Advancing-Front/Local-Reconnection. Their methodology was preformed on a generic hypersonic vehicle with a small kinetic energy weapon separating from within a cavity on top of the vehicle, however, results were just to demonstrate the basic capabilities of the tools developed.

While store separation typically involves a relatively small vehicle being separated from a much larger parent vehicle, it is beneficial to look at cases where two vehicles of similar size are separated from each other in order to see if the vehicle size has an influence over prior results. NASA led a research effort to support the stage separation and ascent aerothermodynamics research program where two Langley Glide-Back Boosters (a generic wing-body configuration) would be separated at speeds from Mach 2.3 to Mach 10 [61, 62]. The Euler and Navier-Stokes simulation results were in good agreement to wind tunnel tests in both qualitative trends and absolute values with small discrepancies being accounted for. These results further show the merit of using similar Navier-Stokes based flow solutions applied to hypersonic store separations to acquire accurate trajectories and body forces.

The early 2000s also saw improvements to CFD technology applied to hypersonic aerothermodynamics from Gnoffo who presented a paper addressing several challenges of the time regarding grid generation and adaption, solution algorithms, and code validation [63]. An adjoint approach to grid generation was shown to be justified as it would provide feedback on the quality of the grids and whether refining or coarsening should be done. Unstructured grid approaches were also shown to be slightly inferior to other techniques, especially regarding heating, as it is difficult to provide high-order accuracy of gradients. Code validation techniques based on experimental data of "unit" flow problems were shown to be ideal as initial and boundary conditions are complicated as a result of an increasing push for higher enthalpy hypersonic flows. Flight tests and direct numerical simulation

(DNS) are the best sources of validation data, but as these methods are not always possible, uncertainty quantification is often necessary. Many points of divergence can be identified using simple geometry code validation cases (such as cylinders and flared cones) which can be corrected when studying more complex geometries.

Higher fidelity research has been done on the flow physics around a cavity at supersonic speeds and an engineer's ability to potentially alter their characteristics to achieve more desirable store separation dynamics. A number of different techniques to control the shear layer over the cavity allowing for it to not impinge on the rear wall have been theorized; however, the main area of study has been non-mechanical devices as to minimize forces acting on the carrier vehicle. A group from The Boeing Company experimented with slot-jet/micro-jet to lift the shear layer over the cavity [64]. They used RANS and LES computations to analyze the Mach 2 flow over a shallow cavity to check viability as well as understand the altered acoustic states. Results showed a significant suppression of the acoustic loads (in the range of 20 dB difference) when implementing the slot-jet along with lifting the shear layer over the back wall of the cavity. The computational methods used in this study, while accurate, are computationally costly leading others to study low-order modeling of micro-jets in attempt to minimize development time. Sahoo et al. [65] derived a low-order model to capture the dominate mechanisms determining the store trajectory with and without using micro-jets. Their method was able to match qualitative trends with experiments showing that the micro-jet pressure can effect the separation dynamics: small pressure micro-jets allow for clean separation compared to no control with high pressure jets. Other non-intrusive methods for shear layer control have been studied, using energy deposition [66] for example, although minimal research has been performed on their effectiveness at hypersonic speeds.

More recent studies in 2015 have looked into the effect of pressure fluctuations within a supersonic cavity with and without a store to determine the structural impacts on the carrier vehicle. Robertson et al. [67] provides a comprehensive study using experiments and CFD on a relatively shallow cavity using Mach 2 flow and a range of Reynolds numbers to understand these processes. Resonant flow features and pressure fluctuations were shown to be well predicted with the presence of a generic store in the cavity altering resonance characteristics. Other more advanced hybrid RANS/LES computational methods [68] would

also be studied, finding similar conclusions. While the aeroacoustics for hypersonic cavities have been studied to some degree thanks to flame holding mechanisms in scramjet engines, the impact of a store placed in a cavity with hypersonic flow is not well studied.

As has been shown, CFD and experimental analysis of realistic hypersonic store separation is still in its infancy due to technological requirements not being met and a focus on operational store separations (typically in the transonic and supersonic regime,) along with some information being closely guarded for national security reasons. Recently, hypersonic vehicles have seen a resurgence in popularity due to new requirements in the modern battlefield and needs for the future of spaceflight; an understanding of the processes associated are paramount for a safe, low risk operation. High fidelity viscous Navier-Stokes CFD solvers have been shown to be the most accurate prediction method currently available and will be utilized in this study.

Chapter 3: Analysis Methodologies

3.1 Store Model

A representative geometry was chosen that does not mimic any geometry which would be used in the real word but could still provide useful data trends of use to the hypersonics field. The seven degree half angle cone sown in Fig. 10 was chosen for its prior ubiquity in hypersonic fundamental work and static CoP according to previous work of Ostapenko [9] and Hyslp et al. [8]. The non-dimensional model uses a length of one with a nose radius 0.1% of it's length that meets tangentially with the conical section. To dimensionalize the store for calculating 6DOF trajectories, an experimental model from Hyslp et al. [8] was closely matched resulting in the geometric and inertial properties found in Table 1 that are non-dimensionalized using the vehicle's length and free stream dynamic pressure of each run. The model is 250 mm long and weighs 669.73 g. The center of gravity was chosen to be 66.59% aft of the nose which coincides with the center of pressure calculated from the 6DOF CFD simulation at it's initial position (a discussion on this will be provided in the results section). This was done to minimize any applied moments on the model due to stabilizing forces. while at an angle-of-attack behind the shock along with exemplifying any forces caused by passing through the shock.

3.2 Computational Methodology

3.2.1 Governing Equations

All simulations were performed using the OVERFLOW 2.3e [14] code developed and maintained by NASA. This is a structured, overset, Reynolds-averaged Navier-Stokes (RANS) solver using a density-based, node-centered, and finite-difference approach. OVERFLOW 2.3e is capable of simulating two-dimensional, axisymmetric, and three-dimensional geometries, and supports six degree-of-freedom (6DOF) motion along with off-body grid

adaptation. The Reynolds-averaged Navier-Stokes equations (RANS) are separated into a mean and fluctuation parts given in Cartesian coordinates as

$$\rho\bar{u_j}\frac{\partial\bar{u_i}}{\partial x_j} = \rho\bar{f_i} + \frac{\partial}{\partial x_j}\left[-\bar{p}\delta_{ij} + \mu\left(\frac{\partial\bar{u_i}}{\partial x_j} + \frac{\partial\bar{u_j}}{\partial x_i}\right) - \rho\overline{u_i'u_j'}\right] \tag{3.1}$$

where the left hand side is the change in momentum, $\rho\bar{f_i}$ represents the mean body force, and the rest is the isotropic stress due to the mean pressure field ($\bar{p}\delta_{ij}$), viscous stresses ($\mu\left(\frac{\partial\bar{u_i}}{\partial x_j} + \frac{\partial\bar{u_j}}{\partial x_i}\right)$), and Reynolds stresses ($\rho\overline{u_i'u_j'}$) [69]. The Reynolds stress term is a result of fluctuations in the flow field and requires additional modeling, typically in the form of turbulence models, to close the RANS equations for solving.

3.2.2 Coordinate Transformation

The Navier-Stokes equations are solved implicitly once transformed into an arbitrary curvilinear space. This can be examined by using a different formulation of the equations given as [70],

$$\frac{\partial\vec{q}}{\partial t} + \frac{\partial}{\partial\xi}\left(\vec{E} - \vec{E}_\nu\right) + \frac{\partial}{\partial\eta}\left(\vec{F} - \vec{F}_\nu\right) + \frac{\partial}{\partial\zeta}\left(\vec{G} - \vec{G}_\nu\right) = 0 \tag{3.2}$$

where $\vec{q}$ is the vector of conserved variables and $\vec{E}$, $\vec{F}$, and $\vec{G}$ are the inviscid fluxes which are

$$\vec{q} = J^{-1}\begin{bmatrix}\rho\\ \rho u\\ \rho v\\ \rho w\\ \rho e_0\end{bmatrix}, \quad \vec{E} = J^{-1}\begin{bmatrix}\rho U\\ \rho uU + \xi_x P\\ \rho vU + \xi_y P\\ \rho wU + \xi_z P\\ U(\rho e_o + P) - \xi_t P\end{bmatrix}, \quad \vec{F} = J^{-1}\begin{bmatrix}\rho V\\ \rho uV + \eta_x P\\ \rho vV + \eta_y P\\ \rho wV + \eta_z P\\ V(\rho e_o + P) - \eta_t P\end{bmatrix},$$

$$\vec{G} = J^{-1} \begin{bmatrix} \rho W \\ \rho u W + \zeta_x P \\ \rho v W + \zeta_y P \\ \rho w W + \zeta_z P \\ V(\rho e_o + P) - \zeta_z P \end{bmatrix} \tag{3.3}$$

The contravariant velocities U, V, and W in Eq. 3.3 are written as

$$\begin{aligned} U &= \xi_t + \xi_x u + \xi_y v + \xi_z w \\ V &= \eta_t + \eta_x u + \eta_y v + \eta_z w \\ W &= \zeta_t + \zeta_x u + \zeta_y v + \zeta_z w \end{aligned} \tag{3.4}$$

The viscous flux terms are given by

$$\vec{E}_\nu = J^{-1} \begin{bmatrix} 0 \\ \xi_x \tau_{xx} + \xi_y \tau_{xy} + \xi_z \tau_{xz} \\ \xi_x \tau_{yx} + \xi_y \tau_{yy} + \xi_z \tau_{yz} \\ \xi_x \tau_{zx} + \xi_y \tau_{zy} + \xi_z \tau_{zz} \\ \xi_x \beta_x + \xi_y \beta_y + \xi_z \beta_z \end{bmatrix}, \quad \vec{F}_\nu = J^{-1} \begin{bmatrix} 0 \\ \eta_x \tau_{xx} + \eta_y \tau_{xy} + \eta_z \tau_{xz} \\ \eta_x \tau_{yx} + \eta_y \tau_{yy} + \eta_z \tau_{yz} \\ \eta_x \tau_{zx} + \eta_y \tau_{zy} + \eta_z \tau_{zz} \\ \eta_x \beta_x + \eta_y \beta_y + \eta_z \beta_z \end{bmatrix},$$

$$\vec{G}_\nu = J^{-1} \begin{bmatrix} 0 \\ \zeta_x \tau_{xx} + \zeta_y \tau_{xy} + \zeta_z \tau_{xz} \\ \zeta_x \tau_{yx} + \zeta_y \tau_{yy} + \zeta_z \tau_{yz} \\ \zeta_x \tau_{zx} + \zeta_y \tau_{zy} + \zeta_z \tau_{zz} \\ \zeta_x \beta_x + \zeta_y \beta_y + \zeta_z \beta_z \end{bmatrix} \tag{3.5}$$

where

$$\tau_{xx} = \lambda\left(u_x + v_y + w_z\right) + 2\mu u_x \qquad \tau_{xy} = \tau_{yx} = \mu\left(u_y + v_x\right)$$

$$\tau_{yy} = \lambda\left(u_x + v_y + w_z\right) + 2\mu v_y \qquad \tau_{yz} = \tau_{zy} = \mu\left(v_z + w_y\right)$$

$$\tau_{zz} = \lambda\left(u_x + v_y + w_z\right) + 2\mu w_z \qquad \tau_{xz} = \tau_{zx} = \mu\left(u_z + w_x\right)$$

$$\beta_x = \gamma\kappa Pr^{-1}\partial_x e_1 + u\tau_{xx} + v\tau_{xy} + w\tau_{xz} \qquad \beta_y = \gamma\kappa Pr^{-1}\partial_y e_1 + u\tau_{yx} + v\tau_{yy} + w\tau_{yz}$$

$$\beta_z = \gamma\kappa Pr^{-1}\partial_z e_1 + u\tau_{zx} + v\tau_{zy} + w\tau_{zz} \qquad e_1 = e\rho^{-1} - 0.5\left(u^2 + v^2 + w^2\right)$$

λ is from the Stokes' hypothesis given as $-2/3\mu$, the dynamic viscosity is $\mu = \nu/\rho$, the ratio of specific heats is γ, the coefficient of thermal conductivity is κ, and Pr is the Prandtl number. The terms u, v, and w are the traditional Cartesian velocity components. The Cartesian derivatives (u_x, v_y, w_z, etc.) are expanded in the curvilinear coordinates using the chain rule as show in

$$u_x = \xi_x u_\xi + \eta_x u_\eta + \zeta_x u_\zeta \tag{3.6}$$

The pressure P term in Eq. 3.3 is defined using the ideal gas law as

$$P = (\gamma - 1)\left[e - 0.5\rho\left(u^2 + v^2 + w^2\right)\right] \tag{3.7}$$

The transformation derivatives in Eq. 3.4 and Eq. 3.5 are found from chain-rule expansion as

$$\xi_x = J\left(y_\eta z_\zeta - y_\zeta z_\eta\right) \qquad \eta_x = J\left(z_\xi y_\zeta - y_\xi z_\zeta\right)$$

$$\xi_y = J\left(z_\eta x_\zeta - x_\eta z_\zeta\right) \qquad \eta_y = J\left(x_\xi z_\zeta - x_\zeta z_\xi\right)$$

$$\xi_z = J\left(x_\eta y_\zeta - y_\eta x_\zeta\right) \qquad \eta_z = J\left(y_\xi x_\zeta - x_\xi y_\zeta\right)$$

$$\eta_x = J\left(y_\xi z_\eta - z_\xi y_\eta\right) \qquad \xi_t = -x_t\xi_x - y_t\xi_y - z_t\xi_z$$

$$\eta_y = J\left(x_\eta z_\xi - x_\xi z_\eta\right) \qquad \eta_t = -x_t\eta_x - y_t\eta_y - z_t\eta_z$$

$$\eta_z = J\left(x_\xi z_\eta - y_\xi x_\eta\right) \qquad \zeta_t = -x_t\zeta_x - y_t\zeta_y - z_t\zeta_z$$

and the Jacobian J from Eq. 3.3 and Eq. 3.5, as well as the spatial transformation derivatives, is given as

$$J^{-1} = x_\xi y_\eta z_\zeta + x_\zeta y_\xi z_\eta + x_\eta y_\zeta z_\xi - x_\xi y_\zeta z_\eta - x_\eta y_\xi z_\zeta - x_\zeta y_\eta z_\xi \tag{3.8}$$

3.2.3 Flux Calculations

All simulations were run using a 5th-order spatial weighted essentially non-oscillatory (WENO5) reconstruction scheme [71] with a Godunov type scheme, as formulated by Harten, Lax, and Van Leer (HLL) [72], to calculate the convective fluxes at the computational grid cell interfaces from Eq. 3.2.

The generic Godunov flux scheme can be examined by simplifying Eq. 3.2 to just the 1-D Euler equation in the ξ direction:

$$\frac{\partial \vec{U}}{\partial t} + \frac{\partial \vec{F}}{\partial \xi} = 0 \tag{3.9}$$

where $\vec{U}$ is the vector of conserved variables and $\vec{F}$ is the inviscid flux vector in the ξ direction given as

$$\vec{U} = \begin{bmatrix} \rho \\ \rho u \\ \rho e_0 \end{bmatrix}, \quad \vec{F} = \begin{bmatrix} \rho u \\ \rho u^2 + P \\ (\rho e_0 + P)u \end{bmatrix} \tag{3.10}$$

Eq. 3.9 is discretized to get

$$\vec{U}_i^{n+1} = \vec{U}_i^n - \frac{\Delta t}{\Delta x}(\vec{F}_{i+1/2} - \vec{F}_{i-1/2}) \tag{3.11}$$

where Δt and Δx are the temporal and spatial increments respectively. The left and right running waves on both sides of the interface must first be solved by using the WENO5 scheme. The WENO scheme achieves a higher order approximation by taking the sum of three third-order approximations. Each of these third-order reconstructions stencils are

weighted in a way to minimize oscillations common in higher-order schemes in regions of high gradients such as shocks. Using q_j to represent the flux value in the current cell and $q_{j+\frac{1}{2}}$ as the interface value, the fifth-order left and right variables can be written as

$$\begin{aligned} \hat{q}^L_{j+\frac{1}{2}} &= w^L_1 \hat{q}^{L1}_{j+\frac{1}{2}} + w^L_2 \hat{q}^{L2}_{j+\frac{1}{2}} + w^L_3 \hat{q}^{L3}_{j+\frac{1}{2}} \\ \hat{q}^R_{j+\frac{1}{2}} &= w^R_1 \hat{q}^{R1}_{j+\frac{1}{2}} + w^R_2 \hat{q}^{R2}_{j+\frac{1}{2}} + w^R_3 \hat{q}^{R3}_{j+\frac{1}{2}} \end{aligned} \tag{3.12}$$

where the three flux reconstructions for the left and right-running waves are

$$\begin{aligned} \hat{q}^{L1}_{j+\frac{1}{2}} &= \tfrac{1}{3} q_{j-2} - \tfrac{7}{6} q_{j-1} + \tfrac{11}{6} q_j \\ \hat{q}^{L2}_{j+\frac{1}{2}} &= \tfrac{-1}{6} q_{j-1} + \tfrac{5}{6} q_j + \tfrac{1}{3} q_{j+1} \\ \hat{q}^{L3}_{j+\frac{1}{2}} &= \tfrac{1}{3} q_j + \tfrac{5}{6} q_{j+1} - \tfrac{1}{6} q_{j+2} \\ \hat{q}^{R1}_{j+\frac{1}{2}} &= \tfrac{1}{3} q_{j+3} - \tfrac{7}{6} q_{j+2} + \tfrac{11}{6} q_{j+1} \\ \hat{q}^{R2}_{j+\frac{1}{2}} &= \tfrac{-1}{6} q_{j+2} + \tfrac{5}{6} q_{j+1} + \tfrac{1}{3} q_j \\ \hat{q}^{R3}_{j+\frac{1}{2}} &= \tfrac{1}{3} q_{j+1} + \tfrac{5}{6} q_j - \tfrac{1}{6} q_{j-1} \end{aligned} \tag{3.13}$$

The modified weights in Eq. 3.12 are given by

$$\omega_k = \frac{\tilde{\omega}_k}{\sum_{i=1}^{3} \tilde{\omega}_i} \tag{3.14}$$

and

$$\begin{aligned} \tilde{\omega}_k &= \frac{\gamma_k}{(\epsilon + \beta_k)^2} \\ \gamma_1 = \frac{1}{10}, \quad \gamma_2 &= \frac{3}{5}, \quad \gamma_3 = \frac{3}{10} \end{aligned} \tag{3.15}$$

The γ_k terms are the optimal weights for each stencil, and the β_k terms are smoothness indicators shown as

$$
\begin{aligned}
\beta_1^L &= \tfrac{13}{12}\left(q_{j-2} - 2q_{j-1} + q_j\right)^2 + \tfrac{1}{4}\left(q_{j-2} - 4q_{j-1} + 3q_j\right)^2 \\
\beta_2^L &= \tfrac{13}{12}\left(q_{j-1} - 2q_j + q_{j+1}\right)^2 + \tfrac{1}{4}\left(q_{j-1} - q_{j+1}\right)^2 \\
\beta_3^L &= \tfrac{13}{12}\left(q_j - 2q_{j+1} + q_{j+2}\right)^2 + \tfrac{1}{4}\left(3q_j - 4q_{j+1} + q_{j+2}\right)^2 \\
\beta_1^R &= \tfrac{13}{12}\left(q_{j+3} - 2q_{j+2} + q_{j+1}\right)^2 + \tfrac{1}{4}\left(q_{j+3} - 4q_{j+1} + 3q_{j+1}\right)^2 \\
\beta_2^R &= \tfrac{13}{12}\left(q_{j+2} - 2q_{j+1} + q_j\right)^2 + \tfrac{1}{4}\left(q_{j+2} - q_j\right)^2 \\
\beta_3^R &= \tfrac{13}{12}\left(q_{j+1} - 2q_j + q_{j-1}\right)^2 + \tfrac{1}{4}\left(3q_{j+1} - 4q_j + q_{j-1}\right)^2
\end{aligned}
\tag{3.16}
$$

The HLL scheme, HLLE++ [73, 74] specifically, approximates the Riemann problem with two propagating waves of speeds S_L and S_R representing the smallest and largest signal speeds in which information is passed. The single state Riemann solution is given by

$$
\vec{U}_{HLLE++} = \left\{ \begin{array}{lll} \vec{U}_L & if & S_L > 0 \\ \vec{U}^* & if & S_L \leq 0 \leq S_R \\ \vec{U}_R & if & S_R < 0 \end{array} \right\} \tag{3.17}
$$

Where $\hat{U}_L$ and $\hat{U}_R$ are found by Eq. 3.12 and the intermediate state $\vec{U}^*$ is

$$
\vec{U}^* = \frac{S_R\vec{U_R} - S_L\vec{U_L} - (\vec{F}_R - \vec{F}_L)}{S_R - S_L} \tag{3.18}
$$

The flux term found by the HLLE++ scheme is written as

$$
\vec{F}_{HLLE++}(\vec{U}_L, \vec{U}_R) = \frac{S^+\vec{F}(\vec{U}_L) - S^-\vec{F}(\vec{U}_R)}{S^+ - S^-} + \frac{S^+S^-}{S^+ - S^-}(\vec{U}_R - \vec{U}_L - \sum_p \delta^p \hat{\alpha}^p \hat{R}^p) \tag{3.19}
$$

where

$$
\begin{aligned}
S^+ &= MAX\{S_R, 0\} \\
S^- &= MIN\{S_L, 0\}
\end{aligned}
\tag{3.20}
$$

$$
S_R = MAX\{\hat{\lambda}_2, (u+a)_R\}
$$

$$S_L = MIN\{\hat{\lambda}_3, (u-a)_L\} \tag{3.21}$$

The Roe-averaged eigenvalues of the inviscid flux Jacobians are

$$\hat{\lambda}_{1,2,3} = [\hat{u}, \hat{u}+\hat{a}, \hat{u}-\hat{a}] \tag{3.22}$$

$\hat{\alpha}^p$ represent the coefficients associated with the linear degenerated and nonlinear fields of characteristic waves which expand $\vec{U}_R - \vec{U}_L$ in terms of the right eigenvectors fo the Roe averaged flux Jacobians $\hat{R}^p$ given as

$$\hat{\alpha}^p = \hat{L}^p(\vec{U}_R - \vec{U}_L) \tag{3.23}$$

$\hat{L}^p$ represents the left eigenvalue matrix of the Roe averaged flux Jacobian. δ^p is the anti-diffusion term used to remove excess numerical dissipation in the linear degenerated fields and can be defined as

$$\begin{aligned} \delta^1 &= \frac{\hat{a}}{|\overline{u}| + \hat{a}} \\ \delta^2 &= \delta^3 = 0 \end{aligned} \tag{3.24}$$

$\overline{u}$ is the approximated speed of the contact discontinuity. This term is found using a switching function based of a pressure sensor k_p calculated along grid lines in order to minimize encountering the "carbuncle" phenomenon when in the presence of strong shocks while still maintaining the low numerical dissipation scheme in boundary layers. This switch is controlled by taking the maximum value of the pressure sensor function in each computational direction (ξ, η, ζ) defined as

$$k_p = ABS\left(\frac{p_{i+1} - 2p_i + p_{i-1}}{p_{i+1} + 2p_i + p_{i-1}}\right) \tag{3.25}$$

with contact discontinuity speed found by

$$|\overline{u}| = \beta|\hat{u}| + (1-\beta)\hat{a} \tag{3.26}$$

Where the switching function β is

$$\beta = \left\{ \begin{array}{rll} 0.0 & if & S_{w_{i,j,k}} > 1.0/DELTA \\ 1 - tanh(10\phi_p^3) & & otherwise \end{array} \right\} \tag{3.27}$$

$$\phi_p = MAX\left(S_{w_{i,j,k}}/DELTA, 0\right)$$

$$S_{w_{i,j,k}} = MAX_{\substack{l=i-1,i+1 \\ m=j-1,j+1 \\ n=k-1,k+1}} \left(k_{p_{i,m,n}}\right)$$

$S_{w_{i,j,k}}$ is the maximum of k_p for all of the neighboring points in all directions. The term $DELTA$ is used in OVERFLOW to control the sensor sensitivity usually in the range of 1 to 10. To find the eigenvalues, the switching function is used to combine the HLLE eigenvalues (λ_{HLLE}) and a version of the eigenvalues from the Roe approximate Riemann solver (λ_{Roe}) employing an entropy fix. The entropy fix is done because the Roe scheme can cause nonphysical expansion shocks near sonic or stagnation points which requires limiting eigenvalues to enforce the entropy condition [73]. These eigenvalues are formulated as

$$\lambda_{HLLE++} = \beta\lambda_{HLLE} + (1-\beta)\lambda_{Roe} \tag{3.28}$$

Where the Roe eigenvalues are

$$\begin{aligned} \lambda_{Roe,1} &= MAX(|\hat{u}|, \hat{a}) \\ \lambda_{Roe,2} &= H(|\hat{u} + \hat{a}|, \epsilon) \\ \lambda_{Roe,3} &= H(|\hat{u} - \hat{a}|, \epsilon) \end{aligned} \tag{3.29}$$

ϵ is chosen as $0.3(|\hat{u}| + \hat{a})$ where H is an entropy fix defined as

$$H(|\lambda|, \epsilon) = \left\{ \begin{array}{rll} |\lambda| & if & |\lambda| > \epsilon \\ \frac{\lambda^2+\epsilon^2}{2\epsilon} & if & |\lambda| \leq \epsilon \end{array} \right\} \tag{3.30}$$

and the HLLE eigenvalues are

$$\begin{aligned}
\lambda_{HLLE,1} &= ((S^+ + S^-)\hat{u} - 2.0(1-\delta^1)(S^+S^-))/(S^+ - S^-) \\
\lambda_{HLLE,2} &= ((S^+ + S^-)(\hat{u} + \hat{a}) - 2.0(1-\delta^2)(S^+S^-))/(S^+ - S^-) \\
\lambda_{HLLE,3} &= ((S^+ + S^-)(\hat{u} - \hat{a}) - 2.0(1-\delta^3)(S^+S^-))/(S^+ - S^-)
\end{aligned} \tag{3.31}$$

This HLLE++ scheme is used over other flux schemes due to its reduced susceptibility to carbuncles, reduced dissipation for boundary layers, and not allowing nonphysical expansion shocks.

3.2.4 Time Discretization

In order to Discretize the Navier-Stokes equation shown in Eq. 3.2, the general matrix form is assumed to be $Ax = b$. Eq. 3.2 can be written in a linearized implicit form, including subiterations, as [14, 75]

$$\begin{aligned}
\left[I + \frac{\Delta t}{(1+\theta)\Delta\tau} + \frac{\Delta t}{1+\theta}\left(\frac{\partial A}{\partial \xi} + \frac{\partial B}{\partial \eta} + \frac{\partial C}{\partial \zeta}\right)\right]\Delta q^{n+1,m+1} = \\
- \left[\left(q^{n+1,m} - q^n\right) - \frac{\theta}{1+\theta}\Delta q^n + \frac{\Delta t}{1+\theta} RHS^{n+1,m}\right]
\end{aligned} \tag{3.32}$$

Where $\theta = 0$ for first order time differencing, and $\theta = \frac{1}{2}$ for second order time differencing. Δt is the user chosen time-step, and $\Delta\tau$ is a pseudo time that may change depending on location when using a local time step. The artificial time term $\frac{\Delta t}{(1+\theta)\Delta\tau}$ is added for dual time stepping and is not included when performing Newton subiterations. In order to maintain time accuracy when using dual time-stepping, this artificial time must converge at each physical time step. The viscous and inviscid fluxes of Eq. 3.2 are represented in the RHS term. $\Delta q^{n+1,m+1}$ is the change in the conserved variables at the latest time step $(n+1)$ and subiteration $(m+1)$. The number of subiterations are defined by an input by the user and used to increase convergence rates when using multiple overset grids.

To solve the assumed general matrix form, A must be inverted. If a direct inversion method were used, the computational time and physical memory allocation required would be a hindrance. Instead, many solution methods approximately factor this matrix in

space which can greatly decrease memory requirements as well as solution time per time-step, however, minimum required time-steps for unsteady problems can become excessive. Another unfactored method is available using relaxation procedures such as the Symmetric Successive Over-Relaxation (SSOR) algorithm and is used for this work. This unfactored approach allows for non-prohibitive time-steps at the cost of more physical memory as the entire implicit flux jacobian matrix must be stored. The SSOR algorithm implemented in OVERFLOW [75] can be written as

$$\Delta q_{j,k,l}^{mm+1} = (1-\Omega)\Delta q_{j,k,l}^{mm} + \Omega(\overline{RHS} - \overline{A_L}\Delta q_{j-1,k,l}^{mm-1} - \overline{A_R}\Delta q_{j+1,k,l}^{mm-1} \\ - \overline{B_L}\Delta q_{j,k-1,l}^{mk1} - \overline{B_R}\Delta q_{j,k+1,l}^{mk2} - \overline{C_L}\Delta q_{j,k,l-1}^{ml1} - \overline{C_R}\Delta q_{j,k,l+1}^{ml2} \quad (3.33)$$

Where the L and R subscripts represent the left and right blocks of the tridiagonal matrices respectively. Ω is the relaxation parameter which is typically 0.9. The overbar represents a premultiply by the inverse of the diagonal matrix $A_D + B_D + C_D$ with the diagonal block of the tridiagonal matrices denoted by the D subscript. The update level of Δq during the iterative matrix solution is denoted as mm. A forward Jacobi sweep is used in j and a symmetric Gauss-Seidel sweep in k and l with the forward and backward sweeps defined as

$$mk1 = mm + 1, \quad mk2 = mm, \quad ml1 = mm + 1, \quad mk2 = mm \quad (3.34)$$

and

$$mk1 = mm, \quad mk2 = mm + 1, \quad ml1 = mm, \quad mk2 = mm + 1 \quad (3.35)$$

respectively. Multiple symmetric sweeps are done for each subiteration.

3.2.5 Turbulence Modeling

OVERFLOW's RANS model is based on the Boussinesq eddy-viscosity hypothesis which assumes the Reynolds stresses have a linear relation to the mean strain rate tensor [76] given as

$$\tau_{ij} = 2\tilde{\mu_t}\left(\tilde{S_{ij}} - \frac{1}{3}\frac{\partial \tilde{u_k}}{\partial x_k}\delta_{ij}\right) - \frac{2}{3}\bar{\rho}k\delta_{ij} \tag{3.36}$$

where τ_{ij} is approximately the Reynolds stress term and $\tilde{\mu_{ij}}$ is the eddy viscosity which will be found from the turbulance model. The strain tensor ($\tilde{S_{ij}}$) is equivalent to $\left(\frac{\partial \tilde{u_i}}{\partial x} + \frac{\partial \tilde{u_j}}{\partial x_k}\right)/2$. OVERFLOW will compute the strain tensor in the turbulence model and outputs $\overline{u'v'}$ by rearranging the previous equations to get

$$\overline{u'v'} \approx -\frac{\tilde{\mu_t}}{\bar{\rho}}\left(\frac{\partial \tilde{u}}{\partial y} + \frac{\partial \tilde{v}}{\partial x}\right) = -2\frac{\tilde{\mu_t}}{\bar{\rho}}\tilde{S_{12}} \tag{3.37}$$

Turbulence modeling was done using the Spalart-Allmaras (SA) model [77] variant, SA-neg-noft2 [75, 78, 79]. The base Spalart-Allmaras formulation models eddy viscosity using a single-equation turbulence model that computes the transport of the working variable $\tilde{\nu}$. The Boussinesq eddy-viscosity assumption is used to evaluate the Reynolds stresses where the eddy viscosity ν_t is

$$\nu_t = \tilde{\nu} f_{v1}, \quad f_{v1} = \frac{\chi^3}{\chi^3 + c_{v1}^3}, \quad \chi \equiv \frac{\tilde{\nu}}{\nu} \tag{3.38}$$

χ is the turbulent Reynolds number and ν is the kinematic viscosity. The transport equation can be formulated as

$$\frac{D\tilde{\nu}}{Dt} = c_{b1}\tilde{S}\tilde{\nu} + \frac{1}{\sigma_s}[\nabla((\nu + \tilde{\nu})\nabla\tilde{\nu}) + c_{b2}(\nabla\tilde{\nu}\cdot\nabla\tilde{\nu})] - c_{w1}f_w\left[\frac{\tilde{\nu}}{d}\right]^2 \tag{3.39}$$

where $c_{b1}\tilde{S}\tilde{\nu}$ and $c_{w1}f_w\left[\frac{\tilde{\nu}}{d}\right]^2$ are the production and wall destruction terms respectively. $\tilde{S}$ is the modified vorticity where Ω will represent the vorticity magnitude and d the distance to the closest wall as show in

$$\tilde{S} = \Omega + \frac{\tilde{\nu}}{\kappa^2 d^2} f_{\nu 2} \qquad \Omega = \sqrt{2W_{ij}W_{ij}}$$

$$d = y \qquad f_w = g\frac{1 + c_{w3}^6}{g^6 + c_{w3}^6}^{\frac{1}{6}}$$

$$f_{\nu 2} = 1 - \frac{\chi}{1 + \chi f_{\nu 1}} \qquad g = r + c_{w2}(r^6 - r)$$

$$r = \frac{\tilde{\nu}}{\tilde{S}k^2 d^2}$$

where the remaining terms are calibrated constants given by

$$\kappa = 0.41 \qquad c_{b1} = 0.1355$$

$$\sigma_s = \frac{2}{3} \qquad c_{b2} = 0.622$$

$$c_{w1} = \frac{c_{b1}}{k^2} + \frac{1 + c_{b2}}{\sigma} \qquad c_{w2} = 0.3$$

$$c_{w3} = 2 \qquad c_{\nu 1} = 7.1$$

with κ being the Kármán constant.

3.2.6 Rigid-Body Dynamics

In order to allow for six degree-of-freedom rigid body dynamics in OVERFLOW, the flow solver uses a separate body dynamics along with a collision detection and modeling solver to complete each full iteration [80]. The periodicity of the body dynamics solver is a user defined value relative to the flow solver's iteration (i.e. for every 10 flow solver iterations, the body dynamics are updated once). The collision detection and modeling was omitted from the process as any collisions were deemed not acceptable and would end the simulation. The flow solver will produce the surface stresses on the vehicle that are then combined with the possible impact forces of a collision to input the three transnational and rotational forces acting on the body into the body dynamics solver. All relations are derived from the

Newtonian linear momentum principle where the expression for translation of the body's center of mass is

$$\overline{F} = \overline{F}_{aero} + \overline{F}_{applied} + \overline{F}_{body} = m\ddot{x} \tag{3.40}$$

By assuming that forces are constant over the time step, Eq. 3.40 can be integrated twice to get an expression for the body's center of mass as a function of time

$$\overline{x}^{n+1} = \frac{1}{2m}\vec{F}^{n}\Delta t^2 + \overline{v}^{n}\Delta t + \overline{x}^{n} \tag{3.41}$$

Euler's equations are used to model the body's rotational motion. By using the body fixed coordinate system aligned with the body principal axes of inertia, the off-diagonal components of the body's inertia tensor are zero allowing Euler's equations to be written as

$$\begin{aligned} T_i &= I_{ii}\dot{\omega}_i - (I_{jj} - I_{kk})\omega_j\omega_k \\ T_j &= I_{jj}\dot{\omega}_j - (I_{kk} - I_{ii})\omega_k\omega_i \\ T_k &= I_{kk}\dot{\omega}_k - (I_{ii} - I_{jj})\omega_i\omega_j \end{aligned} \tag{3.42}$$

where the subscripts j, k, and l are the body-fixed coordinate frame directions. The equations in 3.42 are then solved numerically to get the angular velocities at the next time step. It must be noted that OVERFLOW stores the angular velocities in the inertial frame which are converted into the body-fixed frame for the body dynamics solver, then back into the inertial frame.

3.2.7 Computational Grids

Due to OVERFLOW [14] being a finite-difference solver, structured, overset computational grids are needed. These grids consist of two distinct regions: near-body grids and off-body grids. Near-body grids are those that define a surface's geometry and immediate surroundings defined and constructed by the user with grid generation tools (Pointwise [81] and Chimera Grid Tools [82] in this case.) Off-boy grids are then either automatically generated around surfaces of interest using built-in domain connectivity functions in

OVERFLOW or created manually. Off-body grids successively reduce in resolution until reaching the far-field boundaries. In order to use the fifth-order WENO stencil and get accurate flux reconstruction, three fringe points, or overlap layers, are used. X-RAYS [83] are then used in the domain connectivity process to remove grid points located within surfaces. The off-body grid generation and domain connectivity steps are done once every number of user defined flow-solver iterations during time accurate, moving body simulations to move refined regions in relation to the bodies they are trying to resolve along with preventing orphan points due to insufficient grid overlap.

Near and off-body grid generation followed the best practices outlined by Spalart [84] with initial y^+ values around 0.667 for surfaces and a smaller global maximum stretching ratio of 1.15. An additional user generated refinement region was added just aft of the geometry in-order to accurately capture the immediate wake region. The most refined level of off body-grid was chosen to closely match that of the outer region of the near-body grid. This level of refinement was extended at least one body length aft of the store to accurately capture the wake, and extended sufficiently radially of the vehicle to capture the shock. Grids extend sufficiently as to never interfere with the refined regions regardless of the vehicles location during the simulations.

Two grid systems were created that are specialized for each run. Each domain uses the same near-body grids pictured in Fig. 11. for sweeping the body through angle-of-attacks, an additional refinement region for the wake which uses built-in off-body grid generation that adapts based on the store's orientation shown in Fig. 12. For the 6DOF runs, two off-body grid levels were used extending the one body length aft of the vehicle and tracking it's location and orientation. For the run passing through an oblique shock, the top boundary needs refinement around the initial shock location. This grid was user defined along with a shock aligned refinement region roughly matching the resolution of the furthest layer of the near-body grids in order to minimize varying shock thicknesses caused changing grid spacing. An additional user generated refinement region was added just aft of the geometry in-order to accurately capture the immediate wake region. Due to the complexity of our refined grids, the coarsest grid levels were also user defined roughly capturing the vehicle's

predicted trajectory. These grids are shown for a position mid-run in Figs. 13 and 14. The grid systems roughly total 15 and 25 million points, respectively.

3.2.8 Simulation Inputs and Boundary Conditions

The prescribed motion was run using Mach 7 free flow with a Reynolds's number of 4.65×10^6 and temperature of 83.34 °R, matching wind tunnel conditions from a free flight experiment by Hyslop et al. [8] that will be used as a verification, and 6DOF simulations were run using a Mach number of 7 at a Reynolds number of 8.64×10^6. Solutions were started using a local time stepping to advect and damp start-up transients, then a static time-accurate static solution was found using a maximum of 30 Newton sub-iterations with convergence determined by steady force and moment coefficients. Motion was then activated and data was logged. A global physical time step of 1×10^{-7} was used determined by the time it takes a particle to flow roughly one grid unit on the surface of the vehicle. This value is small due to the high flow velocities associated with each run. Grid connectivity was updated every 100 iterations. The vehicle walls are modeled as viscous adiabatic walls.

For the shock crossing simulation, the upper domain boundary uses a prescribed inflow condition to generate an oblique shock wave. The wave angle was chosen to be 20° (resulting in a 13.52° flow deflection angle) to mimic a possible shock angle created by parent vehicle. This inflow condition is specified using oblique shock theory shown in Eqs. 3.43-3.47 to determine the flow properties behind a desired wave angle with the upstream Mach number set to the free-stream Mach number.

$$cot(a) = tan(s)\left[\frac{(\gamma+1)M^2}{2(M^2 sin^2(s)-1)} - 1\right] \tag{3.43}$$

$$M_1^2 sin^2(s-a) = \frac{((\gamma-1)M^2 sin^2(s))+2}{(2\gamma M^2 sin^2(s)) - (\gamma-1)} \tag{3.44}$$

$$\frac{T_1}{T_0} = \frac{[(2\gamma M^2 sin^2(s)) - (\gamma-1)][((\gamma-1)M^2 sin^2(s))+2]}{(\gamma+1)^2 M^2 sin^2(s)} \tag{3.45}$$

$$\frac{p_1}{p_0} = \frac{(2\gamma M^2 sin^2(s)) - (\gamma - 1))}{\gamma + 1} \tag{3.46}$$

$$\frac{\rho_1}{\rho_0} = \frac{(\gamma + 1)M^2 sin^2(s))}{((\gamma - 1)M^2 sin^2(s)) + 2} \tag{3.47}$$

The subscripts 0 and 1 represent the upstream and downstream conditions respectively with s denoting the shock angle and a the flow deflection angle. The left and right far field boundaries relative to the vehicle are set to symmetry with no reflection planes to continue the oblique shock wave and Riemann characteristic inflow/outflow are used for all other far-field boundary conditions.

Force and moment calculations were handled using MIXSUR [85] and calculated every 10 iterations using the Eqs. 3.48 with 6DOF trajectory handled internally by OVERFLOW.

$$\begin{aligned} C_{lift} &= \frac{\hat{F_{lift}}}{\hat{Q_\infty} \hat{A_{ref}}} & C_{mx} &= \frac{\hat{M_x}}{\hat{Q_\infty} \hat{L_{ref}} \hat{A_{ref}}} \\ C_{drag} &= \frac{\hat{F_{drag}}}{\hat{Q_\infty} \hat{A_{ref}}} & C_{my} &= \frac{\hat{M_y}}{\hat{Q_\infty} \hat{L_{ref}} \hat{A_{ref}}} \\ C_{side} &= \frac{\hat{F_{side}}}{\hat{Q_\infty} \hat{A_{ref}}} & C_{mz} &= \frac{\hat{M_z}}{\hat{Q_\infty} \hat{L_{ref}} \hat{A_{ref}}} \end{aligned} \tag{3.48}$$

C_{lift}, C_{drag}, and C_{side} are the force coefficients in each direction. C_{mx}, C_{mx}, and C_{mx} are the moment coefficients in each direction. Q_∞ is the free stream dynamic pressure, L the reference length, and A the reference area with the hat representing a non-dimensional value. In these equations, M represents the applied moment. Coefficients use the length of the vehicle as the reference length and the total integrated area as the area reference with moments being taken at either the nose or CoG. Body motion is defined based on the Geometry Manipulation Protocol [14] which uses body force and moment coefficients combined with user defined inputs for 6DOF simulations. for the 6DOF simulations, an initial downward ejection velocity of 2.5 m/s was given on the first iteration then 6DOF dynamics selected for the remaining iterations.

3.3 Postprocessing

The force and moment, residual, and trajectory data outputs from OVERFLOW were exported using Chimera Grid Tools [82]. All plotting, visualization, and data manipulation was preformed using a combination of MATLAB [86] and FieldView 21 [87].

Chapter 4: Results

4.1 Store Aerodynamic Properties

Before running complex simulations with multiple influential forces on the vehicle, it is advantageous to understand and validate our model in free flight against experiments and theory. To get a reference point, A simulation was run using Mach 7 free flow with a Reynolds's number of 4.65E6 and temperature of 83.34 °R. The AoA was swept by rotating the vehicle around its center from 0° to 45° with force and moment coefficients logged every 0.01°. The resulting force and moment coefficients along with lift to drag ration are plotted in Figs. 18, 19, and 20 respectively. This simulation was run at similar flow conditions to a free flight wind tunnel experiment of the same geometry performed by Hyslop and McGilvary [8] which tested tested AoAs from -7° to 7°. When comparing our simulation results in the same AoA range, we see good agreement in lift, drag, and pitching moment coefficients.

CoP is calculated using Eq 4.1 where x represents the length from the nose to grid node location in the x direction . The CoP location is plotted in Fig. 21 at 4.5° AoA increments.

$$CoP = \frac{\int x\, p(x)\, dx}{\int p(x)\, dx} \tag{4.1}$$

A numerical integration is done using FieldView which takes the sum of average pressure values over each surface area segment. This method is done for all following CoP calculations unless otherwise stated. To verify CoP measurements, a modified Newtonian model is used as it has been shown to produce satisfactory results with hypersonic vehicles [88]. Newtonian flow assumes that particles when contacting the surface of the vehicle will impart their normal inertial component while retaining the tangential component and moving parallel to the surface. The CoP location is calculated by finding the pressure coefficient at discrete locations along the surface as follows:

$$C_p = C_{p_{max}}\, sin^2(\theta) \tag{4.2}$$

where

$$C_{p_{max}} = \frac{p_{t_2} - p_\infty}{\frac{1}{2}\rho_\infty V_\infty^2} \tag{4.3}$$

$C_{p_{max}}$ is the maximum pressure coefficient, θ is the flow deflection angle, and p_{t_2} it the stagnation pressure behind the shock. Wake regions are assumed to be a perfect vacuum. Pressures are then found and Eq. 4.1 is used to calculate the CoP. A code developed in Matlab [86] is used for these calculations which can handle most simple axisymmetric geometries at any attitude. Other methods exist to predict CoP such a the tangent cone method which is a semi-empirical method that constructs a conical shock at each discrete location along the vehicle using the flow incidence angle then conditions behind the shock are then used to determine surface pressures. Hyslop and McGilvary use this method on the same geometry which produced similar results. From both studies, CoP location is shown to be approximately 66.6% of the vehicles length aft of the nose in regardless of AoA. These results validate our method in the range of AoAs and provides confidence for our force, moment, and surface pressure calculations outside of the experimental range.

The peak lift to drag ratio occurs at approximately 10.5° AoA with a constant lift force gradient from 0° to 25° which decreases to near zero at 45° AoA. The drag forces show a parabolic trend as expected. This design has a low peak lift to drag ratio just shy of 2 making it not particularly desirable for sustained flight as it would have little vertical and lateral controllability. However, many stores do not require control as they simply need to separate cleanly from the parent to accomplish their mission. When referenced from the nose of the vehicle, the pitching moment shows a positive restorative force which grows linearly until the maximum lift to drag point at roughly 10° AoA then continues to grow parabolically. The CoP does move minutely forward at high AoAs according to the RANS data, seen in Fig. 22, and is assumed to be caused by separation and recirculation regions increasing in intensity. Because of the constant CoP location, the dynamic simulations can set the CoG to the same position allowing applied forces to be studied devoid of any variations due to static stability forces.

4.2 Dynamic Simulations

4.2.1 Oblique Shock Wave

In order to check that our oblique shock-wave boundary condition is implemented correctly, a single grid domain was constructed using identical boundary conditions to the dynamic simulation domain but with the top boundary creating a 30° wave angle oblique shock. The domain was created to be a low CPU time run consisting of 147x101x67 grid points with clustering near the top boundary and leading shock location as in Fig. 17. Mach number, pressure, temperature, and density profiles are plotted in the middle of the domain in Fig. 15 with a center-line cut Mach number plot shown in Fig. 16. Fig. 15 shows the boundary condition creates an oblique shock with properties that match those found by theory in Table 2 at the inlet and outlet of the domain. There are notable variances in the flow properties between $X/L = 0.1$ and $X/L = 0.5$ that are believed to be caused by changes in the shock width near the top boundary propagating through the flow field. The shock width is directly related to the grid spacing as the numerical scheme captures the shock over two grid points. To minimize this effect in following simulations, care is taken to minimize varying grid spacing near the shock along with creating refinement regions that are shock aligned.

4.2.2 Shock Crossing

For the dynamic simulation, the vehicle is initially placed at a location above the shock that will not create any interactions between the two. A downward velocity of 2.5 m/s was prescribed on the first time step, after which, the built in 6DoF dynamics solver was used to iterate location and attitude. Instantaneous Mach number on the $y = 0$ plane is plotted every 12 non-dimensional time steps in Fig. 24 with density plotted in Fig. 23. The vehicle's attitude and CoG location are plotted in Figs. 27 and 25 with the CoG trajectory plotted in Fig. 26. As a result of careful grid refinement around the shock, There are minimal flow anomalies behind the shock due to grid spacing changes. Flow properties behind the shock at a location without the influence of the vehicle were probed and matched those values

found from theory. The shocks and wake region also appear to be appropriately captured with no visible steps in the solution.

As shown in Figs. 24 and 23, The store appears to move downward while maintaining its attitude until encountering the shock where it starts to pitch up continuously. The trajectory and attitude plots agree showing the downward motion dominating the velocity component with the pitch slowly increasing until encountering the shock; the pitch quickly increases while passing until clearing the shock where it continues to linearly increase. At the starting location, the vehicle is at an 13.52° AoA relative to the flow vector creating a strong shock on top of the vehicle which can be seen in the density plot. As the vehicle passes through the shock, the flow incidence angle varies across the length of the body dependent on the location relative to the shock; in front of the shock, the Mach 7 flow is parallel to the x-axis; behind the shock, the Mach 4.5 flow is $-13.52°$ from the X-axis. If the vehicle was halfway through the shock at a 0° AoA, the front of the vehicle would have no lift force and only drag acting on it, whereas, the rear of the vehicle would be pushed down causing the total moment on the vehicle to be a product of the back half. The force and moment coefficients were calculated every 10 iterations using the vehicle length as the reference length and the total integrated area as the reference area. Force coefficients are plotted in Fig. 28 with moment coefficients in Fig. 29 relative to the CoG. There is a negative lift as expected at the initial location which gradually turns into a positive lift passing through the shock. Looking the the plot of moments, an initial positive moment (moment is a restorative force turning the vehicle towards the incoming flow vector) showing that the vehicle has some stability forces correcting the AoA. The moment is small but shows the CoG is slightly in front of the true aerodynamic center. This is also true after the vehicle passes through the shock shown by the negative moment. This restorative moment has a maximum value of around 12.5% of the peak moment seen when passing through the shock and is theorized to be caused by viscous and momentum effects pushing the CoP slightly back. It was shown post-run that moving the CoG location 0.1% of the vehicle's length aft would neglect the initial moment variance. Due to the small force relative to the entirety of the run, it is thought to have little impact on results. The applied moment as the vehicle passes through the shock gradually increases, peaks at around 0.014, then decreases gradually until passing the shock where the stability

force dominates. The location of peak moment appears to happen at the location where the shock would pass through the CoG if continued through the vehicle. After passing the shock, the vehicle is at an AoA in free flow with the force an moments matching those found in the previous section when comparing similar positions. Translational and rotational velocities are plotted in Figs. 30 and 31 respectively. The translational velocities are as expected matching the forces applied on the vehicle. The pitch velocity shows acceleration before encountering the shock caused by the stability margin with peak change in velocity at the location of peak applied moment. The vehicle pitch rate slows until passing the shock where it decelerates as expected. Because of the small stability margin in free flow, the vehicle will continue to pitch at close to the same rate continuously after the interaction which is seen in Fig. 27.

As it has already been confirmed, the CoP does not change with AoA in free flow. The differential in flow incidence angle across the vehicle along with a pitch change implies the CoP is not constant through the run as the average force vector is not passing through the NP which causes a rotation. to test this theory, CoP was calculated every 4 non-dimensional time steps and plotted against the CoG location in Fig. 32. This initially shows the CoP located at the NP as expected, then as the vehicle starts to pass through the shock, the CoP moves rearward gradually peaking at 77.8% of the vehicle's length when measured from the nose. The CoP quickly returns to its original location as the rear clears the shock. The CoP location directly coincides with the peak moment on the vehicle CoP and movement is correlated with the area ratio on either side of the shock which dictates how much of the vehicle is exposed to the different flow incidence angles. The vehicle's dynamics when passing through a shock appear to predominantly be the result of differential flow incidence angles causing a stronger shock on the rear of the vehicle causing a higher pressure. The vehicle becomes more stable during the interaction with the CoP moving aft and the peak pitching moment occurring when the shock passes through the CoG if continued through the body. To test this theory, Normalized pressure in the $y = 0$ plane is plotted in Fig. 36 at the point of highest moment which shows a significantly higher pressure on the back half of the vehicle due to the stronger shock. Surface Pressures are shown in Fig. 39 with pressure gradient magnitude plotted solely to show the location of shocks, boundary layers, and expansions.

The the peak surface pressure due to the oblique shock occurs just behind the shock on top of the vehicle and gradually decreases moving back and to radially down. This shows that the strong reflected shock is the driving mode moving the CoP and influencing pitch.

While observing the surface pressure in Fig. 39, an unexpected higher pressure streak in front of the shock can be seen. The shock structure near this location (in black) shows that along the top of the vehicle, a typical oblique SBLI with a flat plate as shown in Fig. 38. The incident shock impacts the surface creating a separation bubble in front which leads to a reflected shock and larger boundary layer afterwards. looking at the shock system in the $z = 0$ plane, a much more complex shock system is seen with three reflected shocks and multiple intermediary features. Looking at Fig. 38; moving closer to the vehicle perpendicularly, the nose's bow shock meets the oblique shock; a reflected shock is created from a large separation bubble which raises the boundary layer off of the surface; finally, the boundary layer reconnects creating another compression shock. This separation region is clearly seen in Fig. 37 showing surface temperatures and in Fig. 40 showing the progression of the SBLI along the vehicle. While the influence on this vehicle's dynamics will be small as the pressure contribution is minimal relative to other areas, the separation region can impact hypersonic vehicle designs in two ways: thermal and structural constraints must be readdressed compared to free flight and subsections separating in this environment can have extremely complex flow fields influencing the trajectory. For example, if a small store such as a sensor cover was released in a region with SBLI, complex an stochastic trajectories are highly likely while passing through this region.

With this geometry, the time spent crossing the shock would have a large influence on the vehicle's attitude due to the solely positive moment applied. When there are two flow directions impacting the surface, there will be a equilibrium attitude of between the two flow angles that will be approached. With placing the CoP and CoG at the same location causing very low stabilizing moments at all AoAs, The equilibrium pitch angle will be whatever the pitch of the vehicle is in free flow, varying only when encountering the shock. The more time spent passing the shock increases the integrated moment applied to the vehicle. This shows that a higher ejection force could minimize upsetting the attitude of the store and lowering the corrective forces needed to return to stable flight. This would also lower the possibility of

a store with a low stability margin oscillating after being upset and recontacting the parent. The initial pitch of the vehicle would also effect the likelihood of movement upwards after the crossing. If there is an initial pitch down, the shock crossing would turn the vehicle back to level flight; the initial best pitch angle to achieve this would be geometry and scenario specific and is another aspect adding complexity to a controlled store separation. It should be noted that, contrary to this test geometry's aerodynamic properties, many other vehicle's CoP move forward with increasing AoA [5] which could negate the influence of the differential incident flows during the crossing. Further studies using a geometry with this phenomena should be conducted to understand the interaction between the two modes causing the CoP to change. There is no upward movement while crossing the shock but after passing through, the vehicle is decelerating downwards due to the pitch up attitude which if not corrected would cause the vehicle to lift upwards. If this vehicle were to have a larger static margin or active control, it could correct its attitude back parallel to the flow. Subsequent stability, control, and trajectory calculations in free flight are possible but outside the scope of this study.

4.3 Numerical Validation and Limitations

The most effective method of verifying computational methods is to compare against flight tests, experimental tests, and theory. This was done for the aerodynamic properties of the vehicle which closely matched as previously discussed, however, as there are no open analogous studies available at the time of writing, other means of verification are needed for other aspect of the study. The assumptions made for this simulation need to be addressed to back the results, the main subjects to analyze are grid refinement, numerical methods, and domain inputs. Regarding grid refinement for this study, the grid spacing was chosen based on available computational hardware resources and is an order of magnitude larger than other hypersonic multi-body studies using similar techniques [58, 62] which were tested against flight experiments to show good agreement. The grid systems used would be the most refined grid resolution if conducting a grid convergence study which was deemed not necessary as a result. For continued studies that might employ stochastic inputs, a smaller

grid system would be desired to shorten run times. In this case, a grid refinement study should be conducted to determine the minimum points required to obtain a desired accuracy. Boundary conditions were chosen such that any unintended or nonphysical influence on the vehicle would not be possible. The inlet boundary condition used to create the oblique shock in the domain does not account for altered flow propagating back through the flow field such as the shock created from the vehicle. Likewise, the left and right symmetry boundary conditions would introduce non-physical shocks if the vehicle shock was to contact them. To counter these impacting the vehicle's dynamics, the domain was created to extend far enough so that any nonphysical effects would be far enough downstream so that no effects could propagate back through the supersonic flow and impact the recirculation region nor the flow field around the vehicle.

To determine if the dynamic simulation has a sensitivity to disturbances in the initial attitude or three dimensional effects, an identical run was preformed where the vehicle would start with a yaw angle 1° to the left. The CoG location is plotted for the original and initially disturbed runs in Fig. 41 with the attitude in Fig. 42, the force coefficients in Fig. 43, and the moment coefficients in Fig. 44. The store shows movement to the left throughout the simulation which is a result of the side force applied due to the yaw angle. Minimal variances are seen in the X and Z directions with any differences thought to be the result of increased drag acting on the vehicle from the initial yaw angle. Likewise, the pitching moment and resulting attitude are almost identical between runs. The previously described residual stability moment can be seen influencing yaw as it does in pitch (increasing while passing through the shock); however, an unexpected roll moment was also induced during this run. This is thought to result from the top right of the store seeing a marginally higher pressure than the top left while the wake region remains relatively unaffected, moving the CoP off of the center line and inducing roll. While small in this run, simulations where the store has a larger yaw angle and are non-axisymmetric could amplify the roll moment which would rotate the lift vector and cause larger deviations in side movement. Further studies would be needed to understand this effect. All together, the findings from the sensitivity analysis imply that this specific scenario is not greatly influenced by three dimensional effects resulting from disturbances in the initial attitude of the store.

The use of hybrid RANS/LES simulations, also known as detached eddy simulation, is also tested to determine its impact on results when compared to RANS simulations. Delayed detached eddy simulation (DDES) is a slightly altered form of detached-eddy simulation (DES) that uses a hybrid system of RANS within the attached boundary layer and large-eddy simulation (LES) in the wake and separation regions. LES provides a direct numerical simulation of the Navier-Stokes equations where the smallest turbulence scales are passed through a low-pass filter to reduce the required computational expense. DDES is able to alleviate some of the issues with previous DES applications where premature switching between RANS and LES was seen in thick boundary layers by overriding the switching logic to maintain RANS behavior in certain regions. because the SA-neg-noft2 turbulence model relies heavily on the length scale d, modeling small scale wake behavior can become ineffective. DDES [89] uses a modified length scale $\tilde{d}$ in place of the Spalart-Allmaras length scale and is given by

$$\tilde{d} = d - f_d MAX(0, d - C_{DES}\Delta) \tag{4.4}$$

where

$$\begin{aligned} f_d &= 1 - \tanh([8r_d]^3) \\ r_d &= \frac{\nu_t + \nu}{\sqrt{U_{i,j}U_{i,j}}\kappa^2 d^2} \end{aligned} \tag{4.5}$$

$C_{DES} = 0.65$, Δ is the magnitude of the longest dimension in the current grid cell, $U_{i,j}$ represents the velocity gradients, and r_d is the ratio of characteristic turbulence model length scale to wall-distance length scale. f_d is the shielding function that when set to 0 yields RANS, whereas, 1 represents the LES regions. Two time-accurate static simulations were run with the vehicle at the same location and attitude as the point of peak moment during the dynamic simulation passing downwards through the shock. The vehicle is held statically with a pitch up angle of 5.64° and is partially through the shock as shown in Fig. 35. The simulations were run time-accurate using Newton subiterations with the force and moment coefficients allowed to stabilize, then run for 1000 iterations. Results were averaged over this time period to eliminate any variances due to oscillations in the coefficients (these oscillations

were deemed negligible after the fact.) Lift, drag, and pitch moment coefficients which dominate the dynamics are tabulated in Table 3 along with the CoP location. Comparing the two solution methods, RANS predicts slightly more lift and drag but with the CoP closer to the nose which causes a smaller pitching moment. These values, however, are small with the largest difference in drag at 0.4507% which should have a negligible impact on the results in this specific case. The DDES simulation was also shown to have a 10% to 15% increase in cpu time per iteration. These combines results show no need to expend the extra computational cost for the increased fidelity of DDES in this specific case, although, store separation simulations that have lower grid resolution or larger wake and flow separation regions can still benefit as in the study from Cui et al. [90] simulating hypersonic shroud separation.

As mentioned in the computational methodologies section, the numerical schemes selected are the best allowable for the scenario in OVERFLOW 2.3e, however, slow and stalled convergence was seen in the near body grid along the side of the vehicle during simulations. An instantaneous solution of a time accurate simulation at 0° AoA in Mach 7 flow is shown in Fig. 33 with surface pressures plotted on the surface and shock location using a filtered shock function relative to the grid in black off of the vehicle. Smaller shocks can be seen between the main attached shock and the vehicle's surface which are not physical and appear to be the result of a non-shock aligned grid. Because the shock angle varies from the The flow incident angle on the vehicle's surface and the near-body grid grows perpendicularly from the surface (ideally, the grid would be shock aligned but in dynamic simulations using Cartesian grids, this is not possible as the shock angle will vary,) the attached shock will continue at a height normal to the surface until jumping to the next level. These jumps appear to be at a similar location as the intermediary shocks and is a known issue; the HLLE++ approximate Riemann solver has been shown by Tramel et al. to cause these variations in flow [73] at low sensitivity (DELTA) values of the shock sensing function. All simulations in this study use a DELTA value of 1.5 to 3 which are much lower that those used by Tramel et al. to mitigate these effects. Larger DELTA values were attempted but caused instability in the solution and for the residuals to stall. This is suspected to be caused by a bug in OVERFLOW 2.3e's SSOR algorithm not using the HLLE++ inviscid flux algorithm,

but instead using a suboptimal version of the HLLE+ flux algorithm which does not use the pressure switch to determine the switching function and instead uses a constant value of 1. It is important understand the impact of these non-physical shocks on the dynamics of the vehicle. A selected range of surface pressures are plotted relative to the shock locations in Fig. 34 as it has the greatest influence on force and moments. There are variations in pressure coinciding with the intermediary shock locations, however, these are small relative to the mean surface pressure and should have little effect on results.

Chapter 5: Conclusions

Computational fluid dynamics was used to model a hypersonic store separation scenario in order to gain a fundamental understanding of associated physical phenomena and analyze current numerical analysis assumptions. A 7° cone was used for the store model as the applied forces and moments can easily be disassociated from those produced by the stability forces produced in free air. This is because the neutral point and CoP are at the same location for supersonic conical bodies where the shock is attached at the apex meaning the CoG can be set to the same location resulting in any rotational motion being to sole result of forces applied by the altered flowfield. Two separate simulations were run with NASA's OVERFLOW 2.3e using a free stream Mach number of 7. First, the store was placed in free air and swept from 0° to 45° AoA to confirm the aerodynamic properties against Newtonian theory and wind tunnel experiments. Next, the store was passed through an oblique shock wave which is analogous to a number of different separation scenarios. The shock wave was created using custom boundary conditions to eliminate any undesirable flow features resulting from a realistic carrier vehicle geometry. While validating the boundary condition against theory, slight anomalies propagating from grid spacing gradients were found. As a result, care was taken to eliminate these while creating the computational meshes. It is noted that this study is not analogous to any flight vehicles which could be used, but done to understand the phenomena associated with the process.

The aerodynamic properties simulation was run using flow conditions form a experimental free flight wind tunnel test performed by Hysolp et al. [8]. Both studiesw ere in good agreement between 0° and 7° AoA when comparing lift, drag, and pitching moment coefficients. The CoP location was also shown in both experiments to be stationary, resulting in the CoP and neutral point to be approximately at the some location. The maximum lift to drag ratio is approximately 1.95 occurring at 10.5° AoA. The CoP is at a point 66.6% of the store's length when measured from the nose and only minutely varies at the highest AoAs. A code was created using modified Newtonian theory to validate the CFD results providing a nearly identical CoP location.

The dynamic simulation passed the store through a 20° oblique shock using a small initial downward velocity then translation and rotation were calculated using OVERFLOW's 6DoF module. The store has small corrective moments at the initial location, counter to what was expected, theorized to be caused by viscous effects near the nose. The moment is relatively small compared to the maximum value and thought to have little impact on results. The store only pitches up while crossing the shock which is caused by the CoP moving aft resulting from a high pressure region on the surface behind the oblique shock. The pitching moment gradually increases, peaks when the shock would pass through the CoG if allowed to continue through the body, then sharply decreases until returning to free air. There appears to be a direct relation between the ratio of surface on either side of the oblique shock and the CoP's location. Large separation regions are seen in front of the shock impact location caused by shock wave boundary layer interactions. This shows that complex trajectories are possible in regions on the carrier vehicle containing SBLI such as near the empennage or engine cowling. Time spend crossing the shock is also shown to have a substantial impact on pitch angle with higher ejection velocities being desirable.

Because there are few available experimental studies on hypersonic store separation to validate conclusions, some large numerical assumptions were studied. The computational grid was created such that a grid resolution study was not needed in this case as an fine resolution was used. The effect of a hybrid RANS/LES solution was tested showing little variation from the RANS solution. A hybrid solution could still be beneficial in cases where the store is in a large separation region but not tested in this study. stalled convergence and stability issues were also seen in the solution theorized to be the result of an incomplete implicit solution algorithm in OVERFLOW 2.3e and from unsteadiness in the separation bubble along the surface. The SSOR solution algorithm does not use the multidimensional pressure switch used in the HLLE++ flux algorithm, but instead, is formulated in a way that is effectively the HLLE flux algorithm. This adds excessive dissipation throughout the domain unlike HLLE++ which only uses HLLE near strong pressure gradients such as shocks. To minimize stability issues duting simulations, the pressure switch sensitivity value was lower than desired causing the steps in the shock leading to altered flow. The effect on surface pressures was shown to be minimal, but it highlights the importance of

shock capturing methods for these cases. Due to the nature of hypersonic store separations, simulations will often have non-shock aligned grids, moving shocks, and moving SBLI; special attention is needed to properly capture these features while maintaining a stable solution.

This experiment was specifically designed to be easily repeatable computationally or experimentally. Ideally, computational studies are backed with experimental results to validate the numerical methods; however, hypersonic experiments require an immense amount of infrastructure and time. This results in many computational studies using nonspecific hypersonic methods applied to unique flight articles. Future studies could extend this fundamental research to other generic features related to store separation such as expansion regions, shear layers created by separation from a cavity, and being in close relation to a surface. A sensitivity analysis varying start location and time relative to cyclic flow features would also be beneficial in understanding major influences dictating trajectories. Parameter identifications could make reduced fidelity models possible. Reduction in computational time is always desired with moving body simulations and understanding fundamental principles can lead to more focused simulation campaigns.

References

[1] Thompson, M. O., At the Edge of Space: The X-15 Flight Program, Washington, DC, and London: Smithsonian Institution Press, 1992.

[2] Isakeit, D., Watillon, P., Wilson, A., and Cazaux, C., The Atmospheric Reentry Demonstrator, European Space Agency, 1998.

[3] McClinton, C., "X-43 - Scramjet Power Breaks the Hypersonic Barrier: Dryden Lectureship in Research for 2006," 44th AIAA Aerospace Sciences Meeting and Exhibit, American Institute of Aeronautics and Astronautics, Reno, Nevada, 2006. https://doi.org/10.2514/6.2006-1.

[4] Keen, K. S., Morgret, C. H., Langham, T. F., and Baker, W. B., "Trajectory Simulations Should Match Flight Tests and Other Lessons Learned in 30 Years of Store-Separation Analysis," 47th AIAA Aerospace Sciences Meeting Including The New Horizons Forum and Aerospace Exposition, American Institute of Aeronautics and Astronautics, Orlando, Florida, 2009. https://doi.org/10.2514/6.2009-99.

[5] Coleman, C. C., and Faruqi, F. A., "On Stability and Control of Hypersonic Vehicles," Tech. Rep. DSTO-TR-2358, Weapons Systems Division Defence Science and Technology Organisation, 2009.

[6] Johnson, D., Thomas, R., and Manor, D., "Stability and Control Analysis of a Wave-Rider TSTO Second Stage," 10th AIAA/NAL-NASDA-ISAS International Space Planes and Hypersonic Systems and Technologies Conference, American Institute of Aeronautics and Astronautics, Kyoto,Japan, 2001, pp. 1–8. https://doi.org/10.2514/6.2001-1834.

[7] Pamadi, B. N., Performance, Stbility, Dynamics, and Control of Airplanes, American Institute of Aeronautics and Astronautics, 2015.

[8] Hyslop, A. M., McGilvray, M., and Doherty, L. J., "Free-Flight Aerodynamic Testing of a 7 Degree Half-Angle Cone," AIAA SCITECH 2022 Forum, American Institute of Aeronautics and Astronautics, San Diego, CA & Virtual, 2022. https://doi.org/10.2514/6.2022-1324.

[9] Ostapenko, N. A., "On the Center of Pressure of Conical Bodies," . (Translation) Izvestiya Akademil Nauk SSSR, Mekhanika Zhidkosti i Gaza, Vol. No. 1, Jan-Feb, 1980, pp. 99–104.

[10] Moran, J., Tinoco, E. N., and Johnson, F. T., "User's Manual-Subsonic/Supersonic Advanced Panel Pilot Code," Tech. Rep. NASA CR-152047, Boeing Military Airplane Development, 1978.

[11] Steger, J. L., Dougherty, F. C., and Benek, J. A., "A Chimera Grid Scheme," 1983.

[12] Cenko, A., "Store Separation Lessons Learned During the Last 30 Years," 27th International Congress of the Aeronautical Sciences, Naval Air Systems Command Patuxent River MD, 2010.

[13] Cenko, A., "Store Separation Overview," Tech. Rep. STO-EN-SCI-277, NATO STO SCI Panel, 2016.

[14] Nichols, R. H., and Buning, P. G., "User's Manual for OVERFLOW 2.3; Version 2.3d," , Feb. 2021.

[15] Chow, R., and Marconi, F., "A Navier-Stokes Solution to Hypersonic Store Separation Flow Fields," 27th Aerospace Sciences Meeting, American Institute of Aeronautics and Astronautics, 1989. https://doi.org/10.2514/6.1989-31.

[16] Newman, G., Fulcher, K., Ray, R., and Pinney, M., "On the Aerodynamics/Dynamics of Store Separation from Hypersonic Aircraft," AIAA 10th Applied Aerodynamics Conference, American Institute of Aeronautics and Astronautics, Palo Alto, CA, 1992. https://doi.org/10.2514/6.1992-2722.

[17] Arnold, R. J., and Epstein, C. S., "AGARD Flight Test Techniques Series. Volume 5. Store Separation Flight Testing," Tech. Report, Advisory Group For Aerospace Research and Development Neuilly-Sur-Seine, France, Apr. 1986.

[18] Carman, J. B., Hill, D. W., and Christopher, J. P., "Store Separation Testing Techniques at the Arnold Engineering Development Center. Volume II. Description of Captive Trajectory Store Separation Testing in the Aerodynamic Wind Tunnel (4T)." Tech. Report AEDC-TR-79-1, Vol. II, Arnold Engineering Development Center, Jun. 1980.

[19] Cenko, A., "Experience in the Use of Computational Aerodynamics to Predict Store Release Characteristics," Progress in Aerospace Sciences, Vol. 37, No. 5, 2001, pp. 477–495. https://doi.org/10.1016/S0376-0421(01)00013-6.

[20] Meyer, R., Cenko, A., and Yaros, S., "An Influence Function Method for Predicting Store Aerodynamic Characteristics During Weapon Separation," Tech. Report AD-A111 777, Grumman Aerospace Corporation Bethpage NY, 1982.

[21] Camarda, C. J., "Space Shuttle Design and Lessons Learned," Tech. Rep. STO-AVT-234-VKI, von Karman Institute, Rhodes-St-Genese, Belgium, 2014.

[22] Jenkins, D., X-15: Extending the Frontiers of Flight, National Aeronautics and Space Administration, 2012.

[23] Goodwin, F. K., Nielsen, J. N., and Dillenius, M. F. E., "A Method for Predicting Three-Degree-of-Freedom Store Separation Trajectories at Speeds up to the Critical Speed:," Tech. Report AGARD-CP-71, Defense Technical Information Center, Fort Belvoir, VA, Jul. 1971. https://doi.org/10.21236/ADA004771.

[24] Cenko, A., Tinoco, E. N., Dyer, R. D., and Dejongh, J., "PAN AIR Applications to Weapons, Carriage and Separation," 18th Aerospace Sciences Meeting, American Institute of Aeronautics and Astronautics, Pasadena,CA,U.S.A., 1980. https://doi.org/10.2514/6.1980-187.

[25] Dougherty, F. C., "Development of a Chimera Grid Scheme with Applications to Unsteady Problems," Ph.D. thesis, Stanford University, California, 1985.

[26] Löhner, R., "Adaptive Remeshing for Transient Problems with Moving Bodies," 11th International Conference on Numerical Methods in Fluid Dynamics, Springer, Berlin, Heidelberg, 1989, p. 5.

[27] Heim, E., "CFD Wing/Pylon/Finned-store Mutual Interference Wind Tunnelexperiment," Tech. Report AEDC-TSR-91-P4, 1991.

[28] Newman III, J. C., and Baysal, O., "Transonic Solutions of a Wing/Pylon/Finned Store Using Hybrid Domaindecomposition," Astrodynamics Conference, American Institute of Aeronautics and Astronautics, Hilton Head Island,SC,U.S.A., 1992. https://doi.org/10.2514/6.1992-4571.

[29] Meakin, R., "Computations of the Unsteady Flow about a Generic Wing/Pylon/Finned-Store Configuration," Astrodynamics Conference, American Institute of Aeronautics and Astronautics, Hilton Head Island,SC,U.S.A., 1992. https://doi.org/10.2514/6.1992-4568.

[30] Madson, M., Moyer, S., and Cenko, A., "TranAir Computations of the Flow about a Generic Wing/Pylon/Finned-Store Configuration," 32nd Aerospace Sciences Meeting and Exhibit, American Institute of Aeronautics and Astronautics, Reno,NV,U.S.A., 1994. https://doi.org/10.2514/6.1994-155.

[31] Genko, A., Gowanlock, Capt. D., Lutton, M. M., and Tutty, M., "F/A-18C/JDAM Applied Computational Fluid Dynamics Challenge II Results," 38th Aerospace Sciences Meeting and Exhibit, American Institute of Aeronautics and Astronautics, Reno,NV,U.S.A., 2000. https://doi.org/10.2514/6.2000-795.

[32] Lijewski, L. E., and Suhs, N. E., "Time-Accurate Computational Fluid Dynamics Approach to Transonic Store Separation Trajectory Prediction," Journal of Aircraft, Vol. 31, No. 4, 1994, pp. 886–891. https://doi.org/10.2514/3.46575.

[33] Atwood, C. A., "Computation of a Controlled Store Separation from a Cavity," Journal of Aircraft, Vol. 32, No. 4, 1995, pp. 846–852. https://doi.org/10.2514/3.46800.

[34] Jordan, J. K., and Denny, A. G., "Approximation Methods for Computational Trajectory Predictions of a Store Released from a Bay," 15th Applied Aerodynamics Conference, American Institute of Aeronautics and Astronautics, Atlanta,GA,U.S.A., 1997. https://doi.org/10.2514/6.1997-2201.

[35] Coleman, L. A., "F-111/Small Smart Bomb Trajectory Predictions for Safe Separation Analysis Using Computational Fluid Dynamics," Aircraft-Stores Compatibility Symposium, Destin, FL, 2001.

[36] Freeman, J. A., Keen, J. M., and Jolly, B. A., ""Quick-Reaction" Computational Fluid Dynamics Support of Aircraft-Store Compatibility,," ITEA Aircraft Store Compatibility Symposium, FT Walton Beach, FL, 2006, pp. presentation slides 19–24.

[37] Johnson, R. A., Stanek, M. J., and Grove, J. E., "Store Separation Trajectory Deviations Due to Unsteady Weapons Bay Aerodynamics," 46th AIAA Aerospace Sciences Meeting and Exhibit, American Institute of Aeronautics and Astronautics, Reno, Nevada, 2008. https://doi.org/10.2514/6.2008-188.

[38] Roughen, K., Wang, X., Bendiksen, O., and Baker, M., "A System for Simulation of Store Separation Including Unsteady Effects," 47th AIAA Aerospace Sciences Meeting Including

The New Horizons Forum and Aerospace Exposition, American Institute of Aeronautics and Astronautics, Orlando, Florida, 2009. https://doi.org/10.2514/6.2009-549.

[39] Mizrahi, I., and Raveh, D. E., "Wing Elasticity Effects on Store Separation," Journal of Aircraft, Vol. 56, No. 3, 2019, pp. 1231–1249. https://doi.org/10.2514/1.C035204.

[40] Perillo, S. R., and Atkins, D. J., "Challenges and Emerging Trends in Store Separation Engineering – an Air Force SEEK EAGLE Office Perspective," 47th AIAA Aerospace Sciences Meeting Including The New Horizons Forum and Aerospace Exposition, 47th AIAA Aerospace Sciences Meeting including The New Horizons Forum and Aerospace Exposition, Orlando, Florida, 2009.

[41] Dillenius, M. F. E., Goodwin, F. K., and Nielsen, J. N., "Prediction of Supersonic Store Separation Characteristics Volume I. - Theroetical Methods and Comparisons with Experiments," Tech. Report AFFDL-TR-76-41, Vol. I, Nielsen Engineering and Research , Inc., Mountain Vier, CA, 1976.

[42] Goodwin, F. K., Keirstead, M. M., and Dillenius, M. F. E., "Prediction of Supersonic Store Separation Characteristics. Vol. II - Users Manual for the Computer Program." Tech. Report AFFDL-TR-76-41, Vol. II,, Nielsen Engineering and Research , Inc., Mountain Vier, CA, 1976.

[43] Goodwin, F. K., Dillenius, M. F. E., and Mulen, J., Jr., "Prediction of Supersonic Store Separation Characteristics Including Fuselage and Stores of Noncircular Cross Section. Volume I - Theoretical Methods and Comparisons with Experiment," Tech. Report AFWAL-TR-80-3032, Vol. I, Nielsen Engineering and Research , Inc., Mountain Vier, CA, 1980.

[44] Waskiewicz, J. D., Dejongh, J., and Cenko, A., "Application of Panel Methods to the Aerodynamic Analysis of Proximity and Mutual Interference Effects on Store Separation at Supersonic Speeds," Aircraft Systems and Technology Conference, American Institute of Aeronautics and Astronautics, Dayton,OH,U.S.A., 1981. https://doi.org/10.2514/6.1981-1653.

[45] Marconi, F., "Nonlinear Analysis of Interfering Bodies in Supersonic Flow." Tech. Report F49620-80-C-0044, Grumman Aerospace Corporation Bethpage NY Research Dept., Jul. 1981.

[46] Marconi, F., "Shock Reflection Transition in Three-Dimensional Steady Flow about Interfering Bodies," AIAA Journal, Vol. 21, No. 5, 1983, pp. 707–713. https://doi.org/10.2514/3.8137.

[47] Stallings, R. L., "Store Separation from Cavities at Supersonic Flight Speeds," Journal of Spacecraft and Rockets, Vol. 20, No. 2, 1983, pp. 129–132. https://doi.org/10.2514/3.28368.

[48] McDearmon, R. W., "Investigation of the Flow in a Rectangular Cavity in a Flat Plate at a Mach Number of 3.55," Tech. Note D-523, Langley Research Center, Langley Field, Va., 1960.

[49] Baysal, O., "Supersonic Aerodynamic Interference Effects of Store Separation, Part I: Computational Analysis of Cavith Flowfields," Tech. Report NASA-CR-180311, Old Dominion University, Norflok, Va, 1986.

[50] Baysal, O., "Supercomputing of Supersonic Flows Using Upwind Relaxation and MacCormac Schemes," Journal of Fluids Engineering, Vol. 110, No. 1, 1988, pp. 62–68.

[51] Butler, G., King, D., Abate, G., and Stephens, M., "Ballistic Range Tests of Store Separation at Supersonic to Hypersonic Speeds," 29th Aerospace Sciences Meeting, American Institute of Aeronautics and Astronautics, Reno, Nevada, 1991. https://doi.org/10.2514/6.1991-199.

[52] Ma, E., "A Transonic/Supersonic/Hypersonic CFD Analysis of the Entry Space Shuttle Orbiter," 10th Applied Aerodynamics Conference, American Institute of Aeronautics and Astronautics, Palo Alto,CA,U.S.A., 1992. https://doi.org/10.2514/6.1992-2614.

[53] Slotnick, J. P., Kandula, M., and Buning, P. G., "Navier-Stokes Simulation of the Space Shuttle Launch Vehicle Flight Transonic Flowfield Using a Large Scale Chimera Grid System," 12th Applied Aerodynamics Conference, American Institute of Aeronautics and Astronautics, Colorado Springs,CO,U.S.A., 1994. https://doi.org/10.2514/6.1994-1860.

[54] Hawkins, R., and Dilley, A., "CFD Comparisons with Wind Tunnel and Flight Data for the X-15," AlAA 4th International Aerospace Planes Conference, American Institute of Aeronautics and Astronautics, Orlando, FL, 1992. https://doi.org/10.2514/6.1992-5047.

[55] Freeman, D. C., Jr., Reubush, D. E., McClinton, C. R., Rausch, V. L., and Crawford, J. L., "The NASA Hyper-X Program," 48th International Astronautical Congress, International Astronautical Federation, Turin, Italy, 1997.

[56] Baysal, O., and Luo, X., "Staging of a Hypersonic Vehicle - Numerical Simulations Using Dynamic Unstructured Meshes," 16th AIAA Applied Aerodynamics Conference, American

Institute of Aeronautics and Astronautics, Albuquerque, NM, 1998. https://doi.org/10.2514/6.1998-2412.

[57] Luo, X., and Baysal, O., "Computational Simulation of Hypersonic Vehicle Separation from Its Booster," 9th International Space Planes and Hypersonic Systems and Technologies Conference, American Institute of Aeronautics and Astronautics, Norfolk,VA,U.S.A., 1999. https://doi.org/10.2514/6.1999-4807.

[58] Buning, P. G., Wong, T., Dilley, A. D., and Pao, J. L., "Computational Fluid Dynamics Prediction of Hyper-X Stage Separation Aerodynamics," Journal of Spacecraft and Rockets, Vol. 38, No. 6, 2001, pp. 820–827. https://doi.org/10.2514/2.3771.

[59] Woods, W. C., Holland, S. D., and DiFulvio, M., "Hyper-X Stage Separation Wind-Tunnel Test Program," Journal of Spacecraft and Rockets, Vol. 38, No. 6, 2001, pp. 811–819. https://doi.org/10.2514/2.3770.

[60] Marcum, D. L., "Computational Simulation of Unsteady, Viscous, Hypersonic Flow about Flight Vehicles with Store Separation," Technical Report AFOSR Grant No. F49620-95-1-0020, Mississippi State University, Feb. 2001.

[61] Murphy, K. J., Buning, P. G., Pamadi, B. N., Scallion, W. I., and Jones, K. M., "Overview of Transonic to Hypersonic Stage Separation Tool Development for Multi-Stage-To-Orbit Concepts," 24th AIAA Aerodynamic Measurement Technology and Ground Testing Conference, American Institute of Aeronautics and Astronautics, Portland, Oregon, 2004. https://doi.org/10.2514/6.2004-2595.

[62] Buning, P. G., Gomez, R. J., and Scallion, W. I., "CFD Approaches for Simulation of Wing-Body Stage Separation," 22nd Applied Aerodynamics Conference and Exhibit, American Institute of Aeronautics and Astronautics, Providence, Rhode Island, 2004. https://doi.org/10.2514/6.2004-4838.

[63] Gnoffo, P., "Computational Fluid Dynamic Technology for Hypersonic Applications," AIAA International Air and Space Symposium and Exposition: The Next 100 Years, American Institute of Aeronautics and Astronautics, Dayton, Ohio, 2003. https://doi.org/10.2514/6.2003-2829.

[64] Mani, M., Cary, A. W., and Bower, W. W., "Accurate Flow Prediction for Store Separation from Internal Bay," 3rd International Symposium on Integrating CFD and Experiments in Aerodynamics, U.S. Air Force Academy, CO, 2007. https://doi.org/10.1007/3-540-31801-1_38.

[65] Sahoo, D., Annaswamy, A., and Alvi, F., "Active Store Trajectory Control in Supersonic Cavities Using Microjets and Low-Order Modeling," AIAA Journal, Vol. 45, No. 3, 2007, pp. 516–531. https://doi.org/10.2514/1.18007.

[66] Lazar, E., Elliott, G., and Glumac, N., "Control of the Shear Layer Above a Supersonic Cavity Using Energy Deposition," AIAA Journal, Vol. 46, No. 12, 2008, pp. 2987–2997. https://doi.org/10.2514/1.32835.

[67] Robertson, G., Kumar, R., Doyle, S., Baker, M., Roughen, K., and Johnson, R. A., "Acoustics of a Supersonic Cavity with a Generic Store," 53rd AIAA Aerospace Sciences Meeting, American Institute of Aeronautics and Astronautics, Kissimmee, Florida, 2015. https://doi.org/10.2514/6.2015-1292.

[68] Sheta, E. F., Harris, R. E., Luke, E. A., and Ukeiley, L. S., "Hybrid RANS/LES Acoustics Prediction in Supersonic Weapons Cavity," 53rd AIAA Aerospace Sciences Meeting, American Institute of Aeronautics and Astronautics, Kissimmee, Florida, 2015. https://doi.org/10.2514/6.2015-0009.

[69] Tennekes, H., and Lumley, J. L., A First Course in Turbulence, MIT Press, 1972.

[70] Pulliam, T. H., and Steger, J. L., "Implicit Finite-Difference Simulations of Three-Dimensional Compressible Flow," AIAA Journal, Vol. 18, No. 2, 1980, pp. 159–167. https://doi.org/10.2514/3.50745.

[71] Nichols, R. H., Tramel, R. W., and Buning, P. G., "Evaluation of Two High-Order Weighted Essentially Nonoscillatory Schemes," AIAA Journal, Vol. 46, No. 12, 2008, pp. 3090–3102. https://doi.org/10.2514/1.36849.

[72] Harten, A., Lax, P. D., and Leer, B. V., "On Upstream Differencing and Godunov-Type Schemes for Hyperbolic Conservation Laws," SIAM Review, Vol. 25, No. 1, 1983, pp. 35–61. https://doi.org/10.1137/1025002.

[73] Tramel, R., Nichols, R., and Buning, P., "Addition of Improved Shock-Capturing Schemes to OVERFLOW 2.1," 19th AIAA Computational Fluid Dynamics, American Institute of Aeronautics and Astronautics, San Antonio, Texas, 2009. https://doi.org/10.2514/6.2009-3988.

[74] Park, S.-H., and Kwon, J., "An Improved HLLE Method for Hypersonic Viscous Flows," 15th AIAA Computational Fluid Dynamics Conference, American Institute of Aeronautics and Astronautics, Anaheim,CA,U.S.A., 2001. https://doi.org/10.2514/6.2001-2633.

[75] Nichols, R., Tramel, R., and Buning, P., "Solver and Turbulence Model Upgrades to OVERFLOW 2 for Unsteady and High-Speed Applications," 24th AIAA Applied Aerodynamics Conference, American Institute of Aeronautics and Astronautics, San Francisco, California, 2006. https://doi.org/10.2514/6.2006-2824.

[76] Jespersen, D. C., Pulliam, T. H., and Childs, M. L., "OVERFLOW Turbulence Modeling Resource Validation Results," Technical NAS-2016-01, NASA Ames Research Center, 2016.

[77] Spalart, P. R., and Allmaras, S. R., "A One-Equation Turbulence Model for Aerodynamic Flows," 30th Aerospace Sciences Meeting and Exhibit, American Institute of Aeronautics and Astronautics, Reno,NV,U.S.A., 1992. https://doi.org/10.2514/6.1992-439.

[78] Allmaras, S. R., Johnson, F. T., and Spalart, P. R., "Modifications and Clarifications for the Implementation of the Spalart-Allmaras Turbulence Model," Computational Fluid Dynamics, 2012, p. 11.

[79] Eça, L., Hoekstra, M., Hay, A., and Pelletier, D., "A Manufactured Solution for a Two-Dimensional Steady Wall-Bounded Incompressible Turbulent Flow," International Journal of Computational Fluid Dynamics, Vol. 21, No. 3-4, 2007, pp. 175–188. https://doi.org/10.1080/10618560701553436.

[80] Meakin, R., "Multiple-Body Proximate-Flight Simulation Methods," 17th AIAA Computational Fluid Dynamics Conference, American Institute of Aeronautics and Astronautics, Toronto, Ontario, Canada, 2005. https://doi.org/10.2514/6.2005-4621.

[81] "Pointwise," Cadence Design Systems, 2023.

[82] Chan, W. M., Pandaya, S. A., Rogers, S. E., Jensen, J. C., Lee, H. C., Kao, D. L., Buning, P. G., Meakin, R. L., Boger, D. A., and Nash, S. M., "Users Manual for Chimera Grid Tools," , 2018.

[83] Chan, W. M., Kim, N., and Pandya, S. A., "Advances in Domain Connectivity for Overset Grids Using the X-rays Approach," Seventh International Conference on Computational Fluid Dynamics (ICCFD7), American Institute of Aeronautics and Astronautics, Big Island, Hawaii, 2012, p. 20.

[84] Spalart, P. R., "Young-Person's Guide to Detached-Eddy Simulation Grids," Tech. Rep. NASA CR-2001-211032, Boeing Commercial Airplanes, Seattle, Washington, 2001.

[85] Chan, W. M., and Buning, P. G., "User's Manual for FOMOCO Utilities - Force and Moment Computation Tools for Overset Grids," 110408 Technical Memorandum 110408, NASA, 1996.

[86] "MATLAB R2018b," The MathWorks Inc., 2018.

[87] "FieldView 21," Vela Software International, 2022.

[88] Heybey, W. H., "Newtonian Aerodynamics for General Body Shapes with Several Applications," Technical Memorandum X-53391, Spdce Flight Center, Huntsville,AL,U.S.A., 1966.

[89] Spalart, P. R., Deck, S., Shur, M. L., Squires, K. D., Strelets, M. Kh., and Travin, A., "A New Version of Detached-eddy Simulation, Resistant to Ambiguous Grid Densities," Theoretical and Computational Fluid Dynamics, Vol. 20, No. 3, 2006, pp. 181–195. https://doi.org/10.1007/s00162-006-0015-0.

[90] Cui, P., Jia, H., Chen, J., Zhou, G., Wu, X., Ma, M., Li, H., and Tang, J., "Numerical Investigation on Unsteady Shock Wave/Vortex/Turbulent Boundary Layer Interactions of a Hypersonic Vehicle during Its Shroud Separation," Aerospace, Vol. 9, No. 619, 2022.

[91] Archives, U. N., "F-16 Pylon," https://nara.getarchive.net/media/a-view-of-the-stores-on-pylons-under-the-right-wing-of-an-f-16a-fighting-falcon-970e58, May 1990.

[92] Goode, D. C., "F-117," https://www.britannica.com/technology/F-117/images-videos, ????

[93] Mosele, JP., Gross, A., and Slater, J., "Numerical Investigation of Mach 2.5 Axisymmetric Turbulent Shock Wave Boundary Layer Interactions," Aerospace, Vol. 10, No. 159, 2023.

Appendix

Appendix A: Chapter 1 Figures and Tables

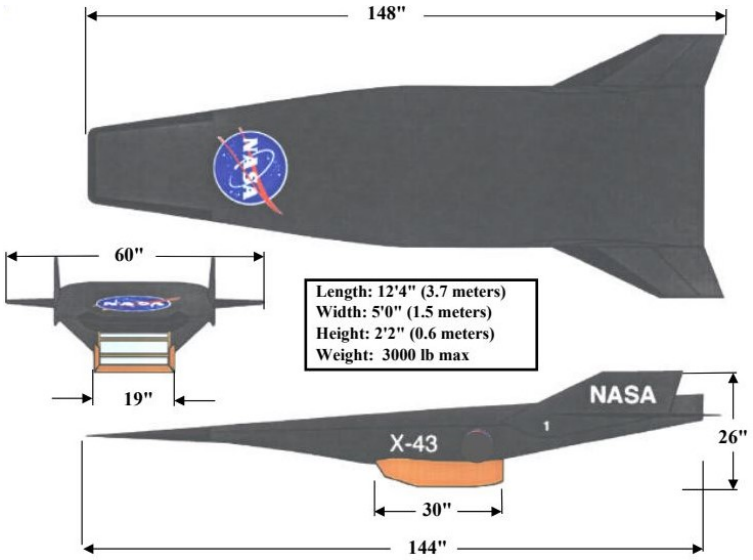

Figure 1: Hyper-X/X-43A research vehicle geometry [8]

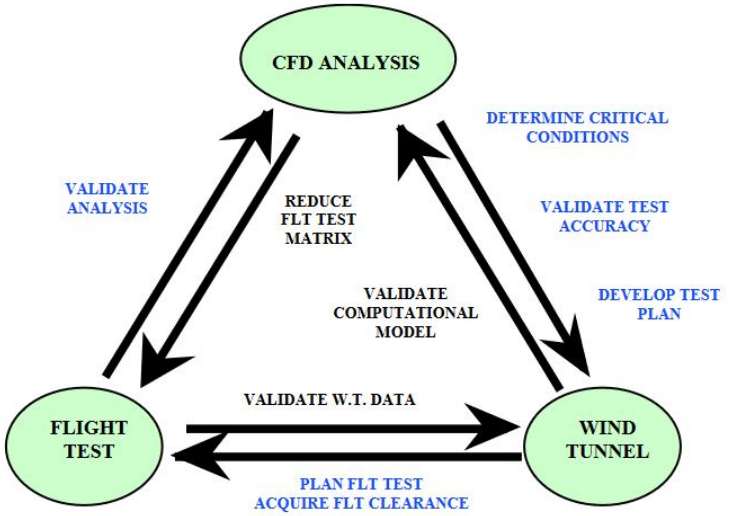

Figure 2: Integrated Test and Evaluation Approach to Store Separation [13]

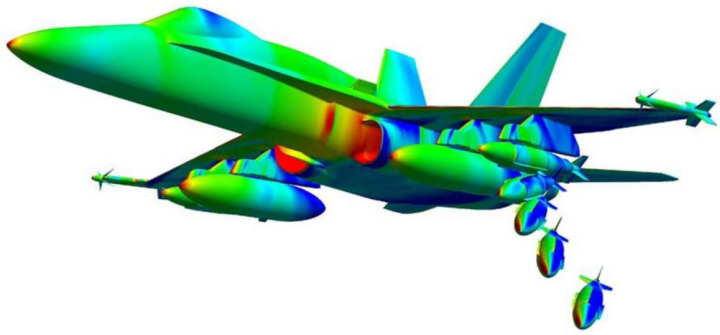

Figure 3: F-18C/GBU-31 Transonic Trajectory Simulation [12]

Appendix B: Chapter 2 Figures and Tables

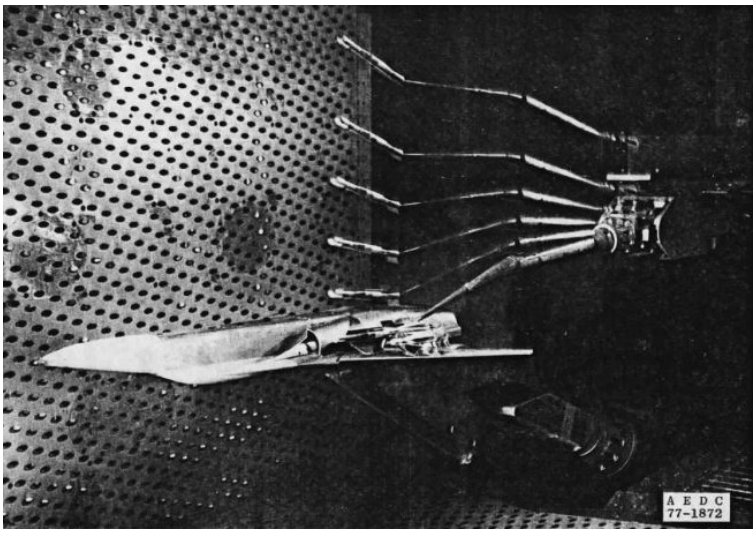

Figure 4: Captive trajectory system showing multiple locations of the released store [18]

Figure 5: F-16 pylon and store configuration [91]

Figure 6: Pylon Damage on the X-15 Caused by Shock Shock Interactions [22]

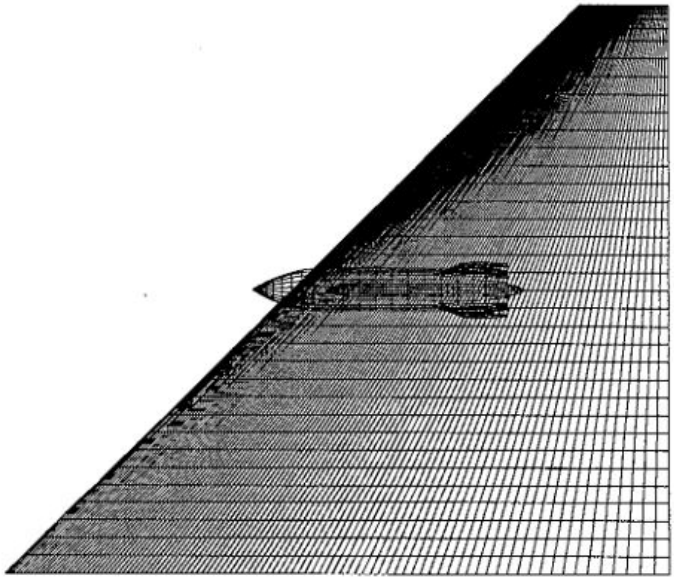

a) Top view

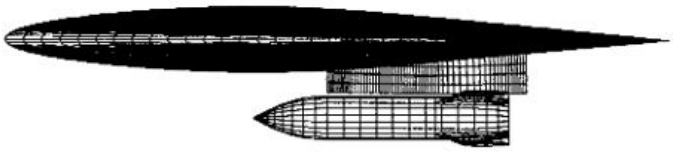

b) Side view

c) Front view

Figure 7: Generic Transonic Store Separation Test Configuration [30]

Figure 8: F-117 Stealth Aircraft [92]

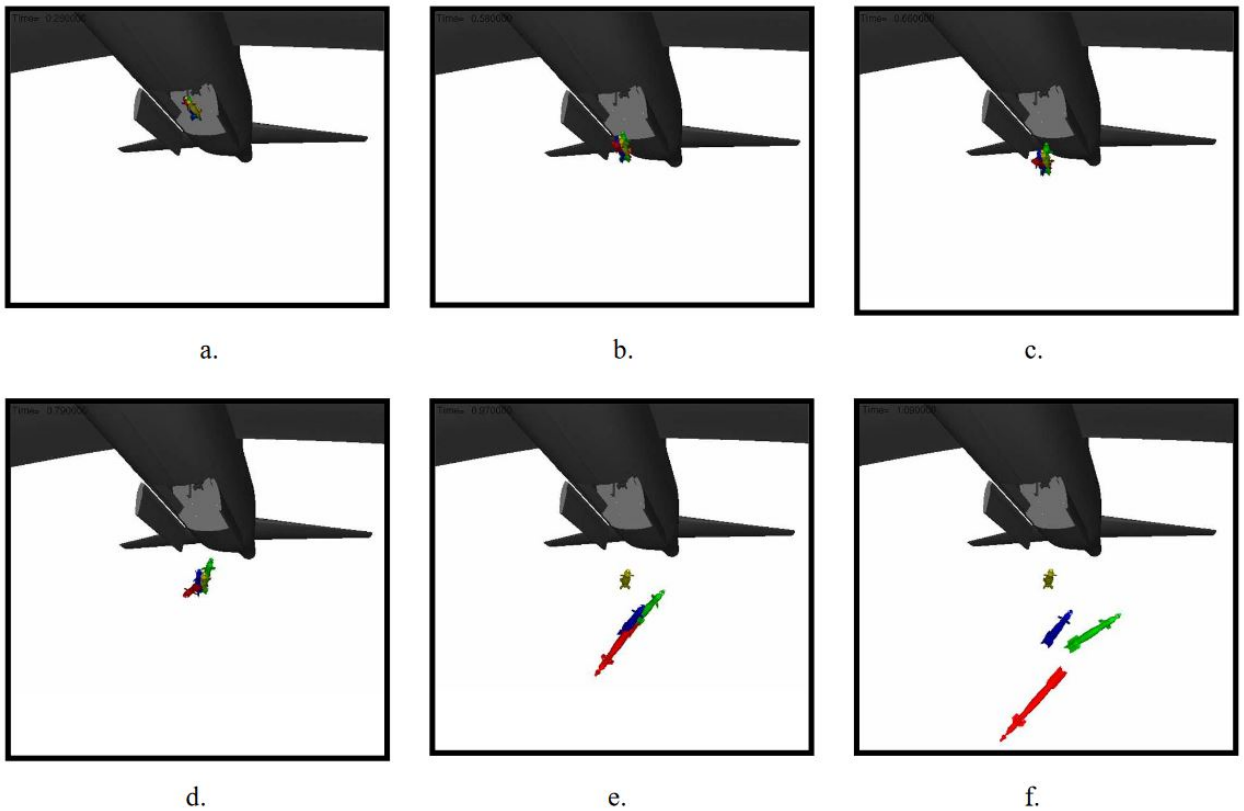

Figure 9: Superimposed GBU-12B trajectory images from four separation events [37]

Appendix C: Chapter 3 Figures and Tables

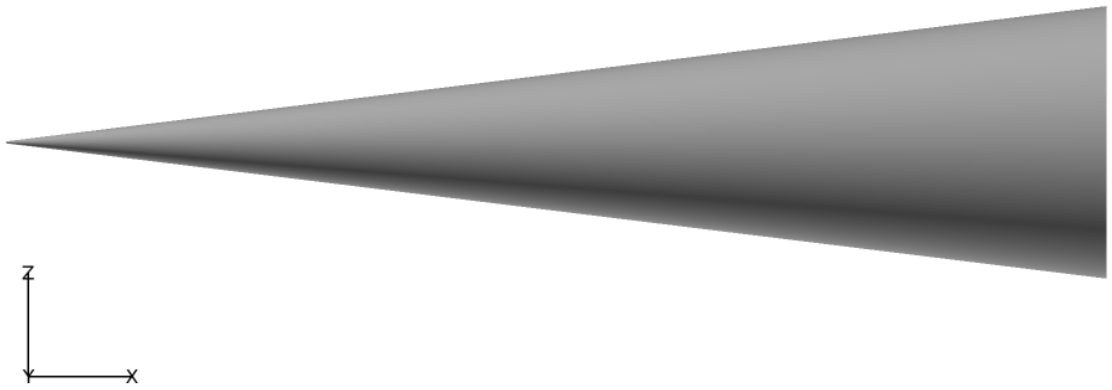

Figure 10: 7° Half-Angle Cone Geometry

Table 1: Representative Geometric and Inertial Properties

Length (mm)	250
Cone Half-Angle (°)	7
Nose Radius (mm)	0.25
Center of Gravity (mm from nose)	166.5
Mass (g)	669.73
Moment of Inertia I_{xx} (kgm^2)	5E-5
Moment of Inertia I_{yy} (kgm^2)	2.15E-3
Moment of Inertia I_{zz} (kgm^2)	2.15E-3

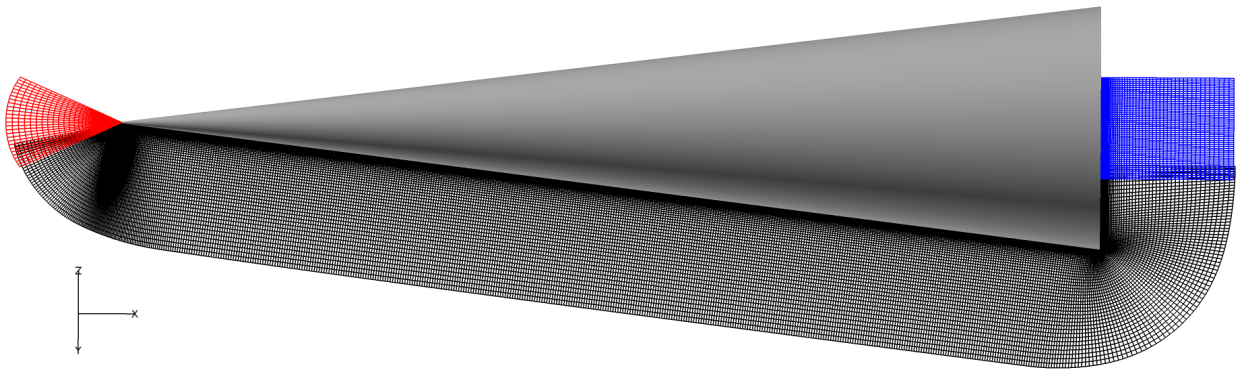

Figure 11: Near-Body Grids

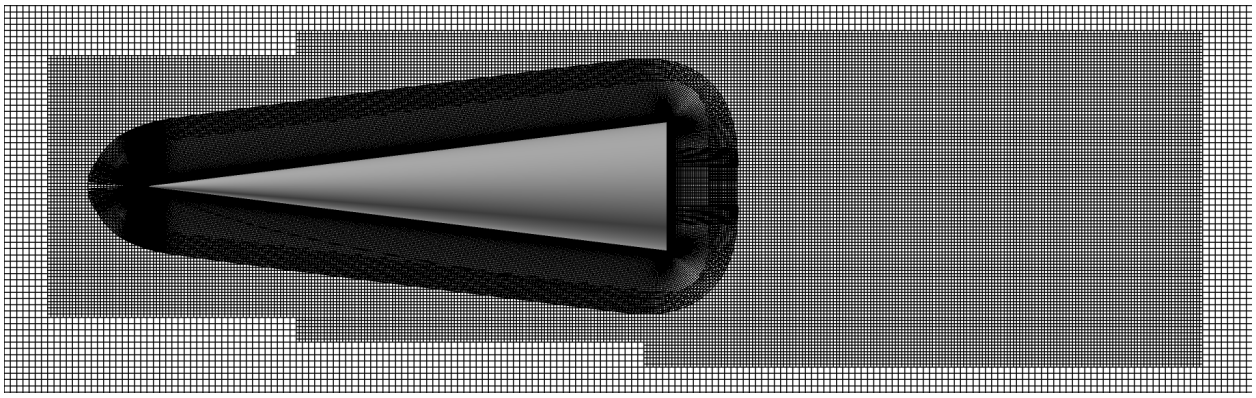

Figure 12: Automatically Generated Off-Body Grids

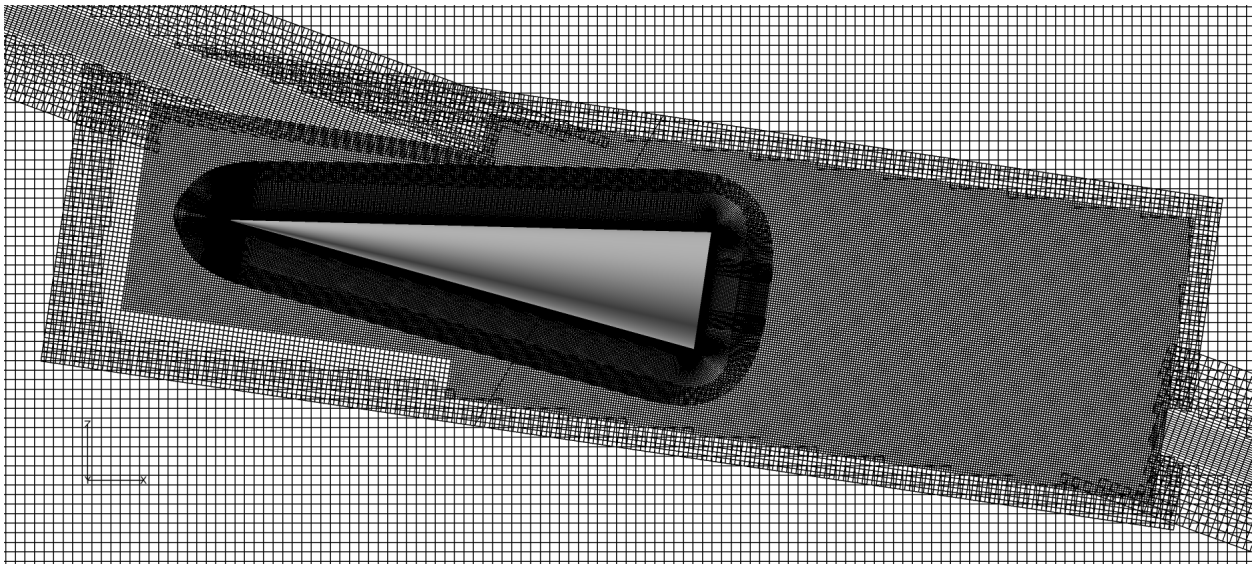

Figure 13: Off-Body Grids for Dynamic Simulation

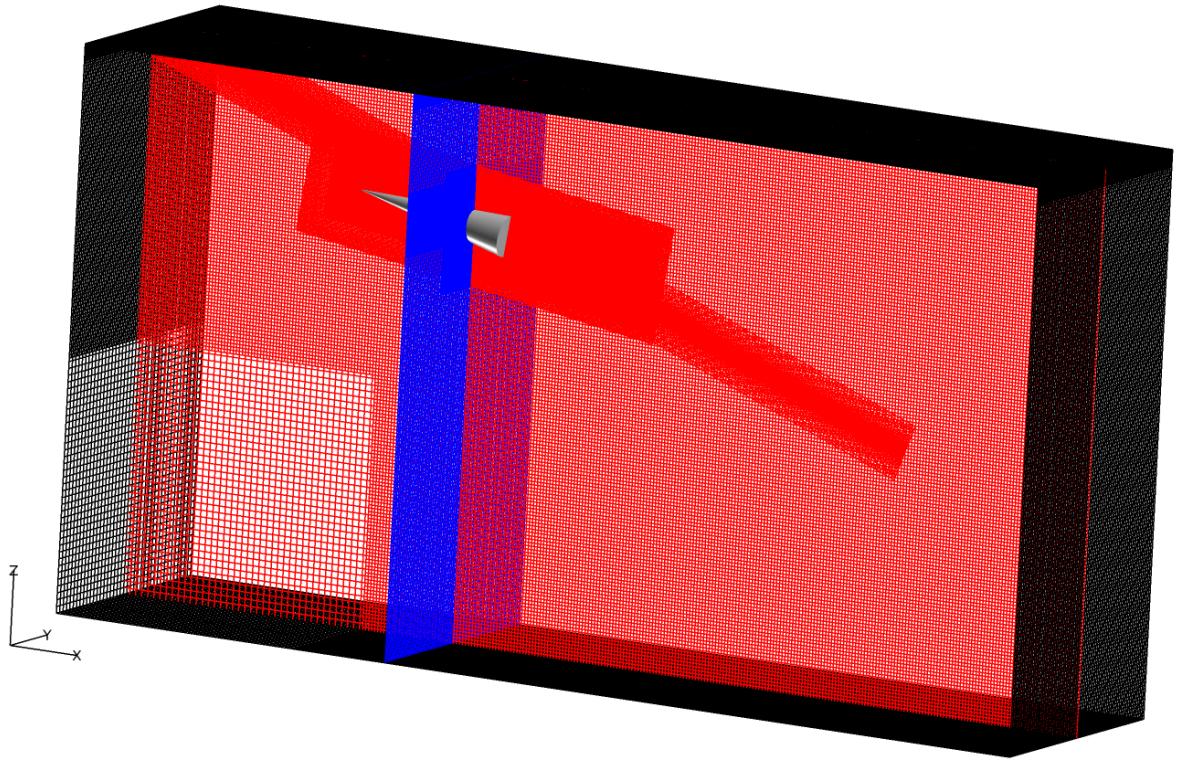

Figure 14: Computational Domain for Dynamic Simulation

Appendix D: Chapter 4 Figures and Tables

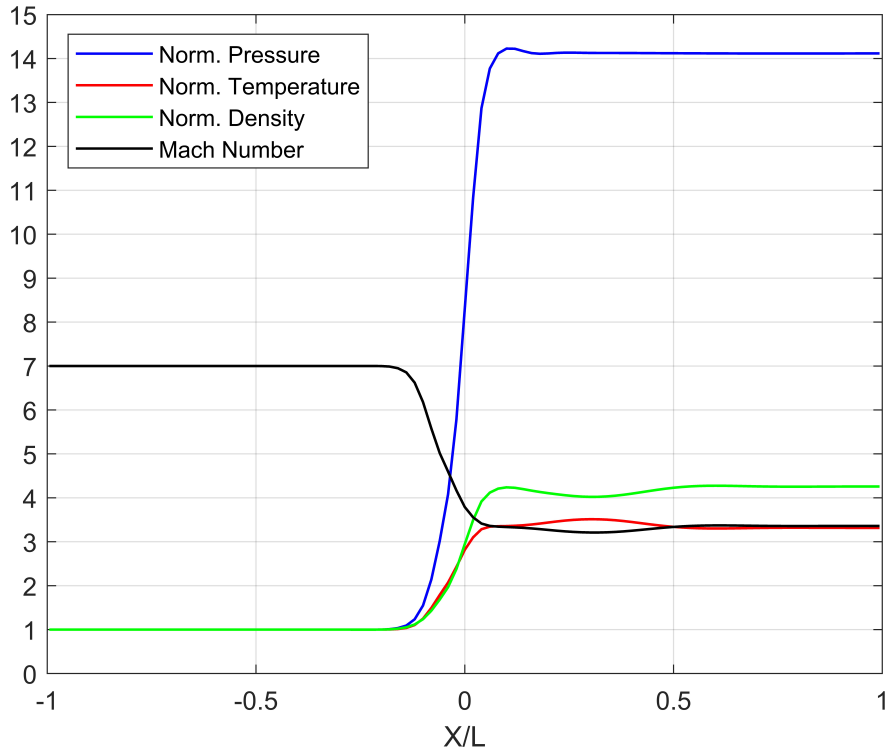

Figure 15: Flow Properties Over 30° Oblique Shock Created by Top Boundary Condition

Table 2: Theoretical Properties Over 30° Wave Angle Oblique Shock

M_2/M_1	3.360
P_2/P_1	14.125
T_2/T_1	3.315
ρ_2/ρ_1	4.261

Figure 16: Mach Number for 30° Oblique Shock Created by Top Boundary Condition

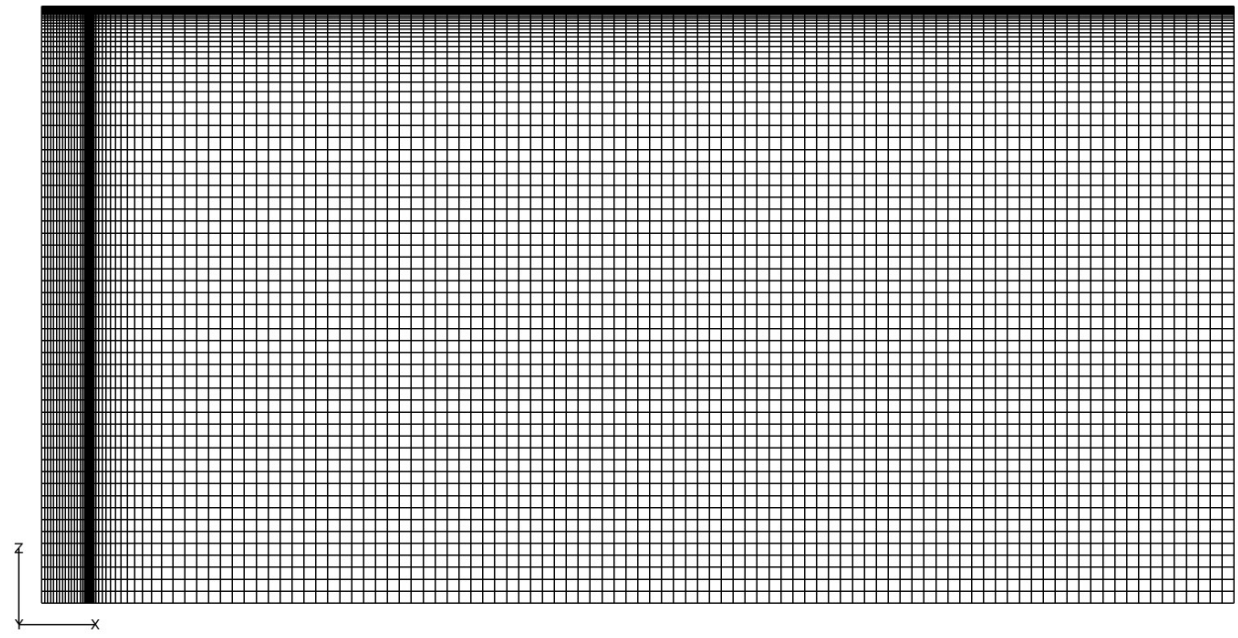

Figure 17: Grid for Oblique Shock Created by Top Boundary Condition

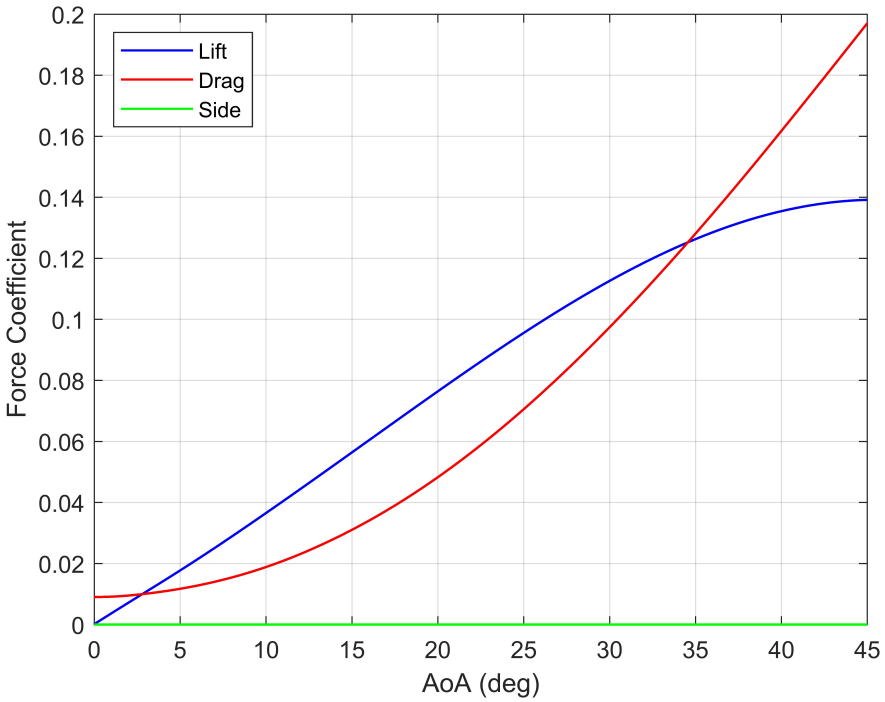

Figure 18: Force Coefficients in Free Air

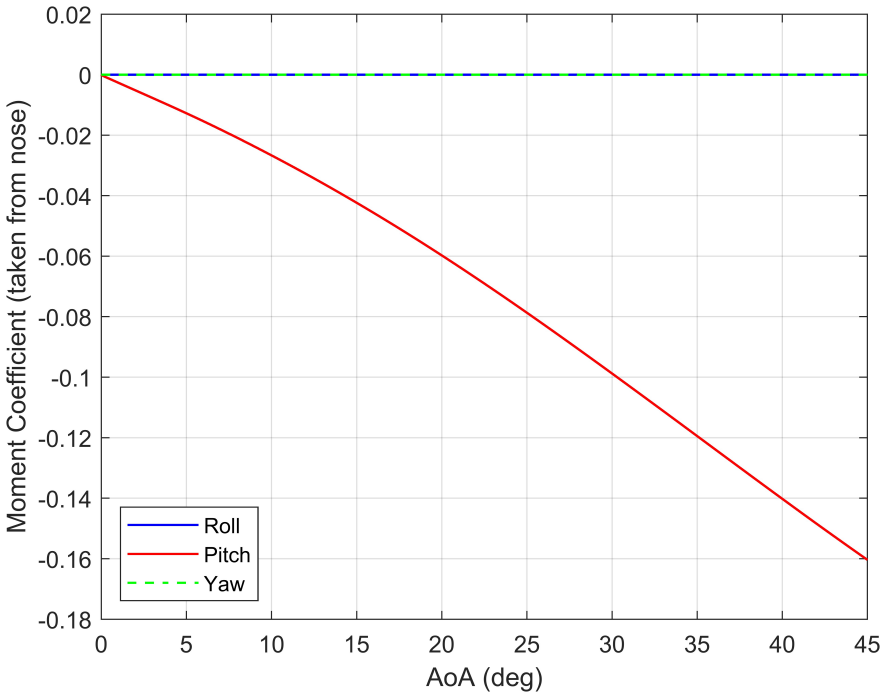

Figure 19: Moment Coefficients in Free Air

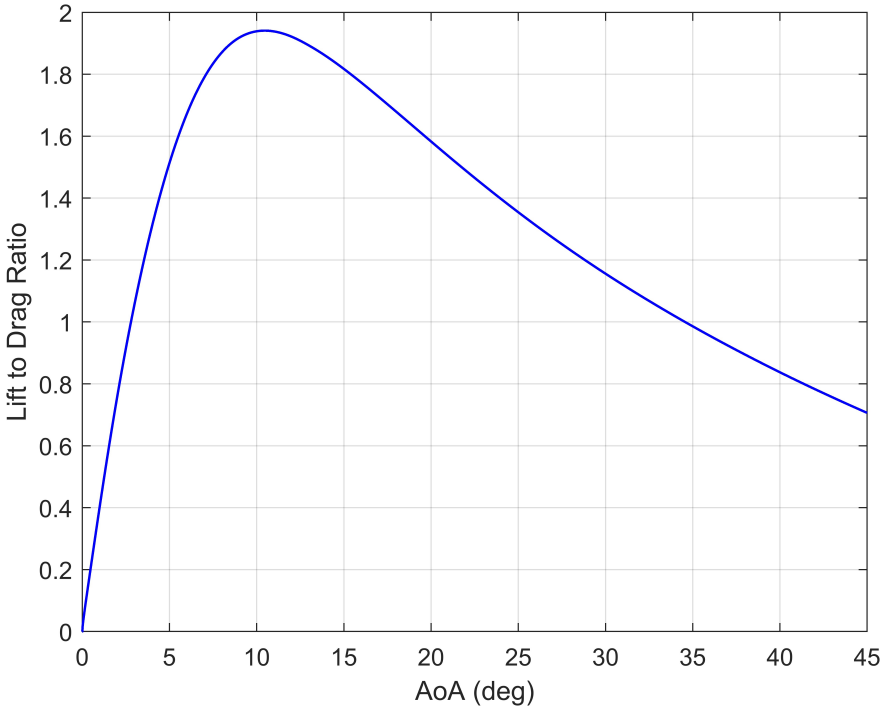

Figure 20: Lift to Drag Ratio in Free Air

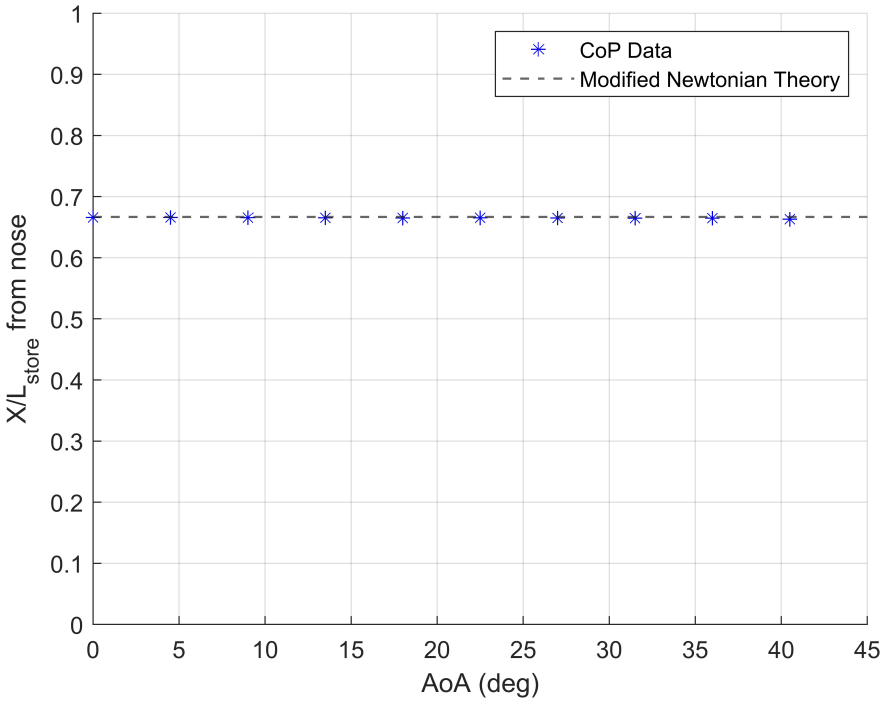

Figure 21: Center of Pressure Location for AoA Sweep

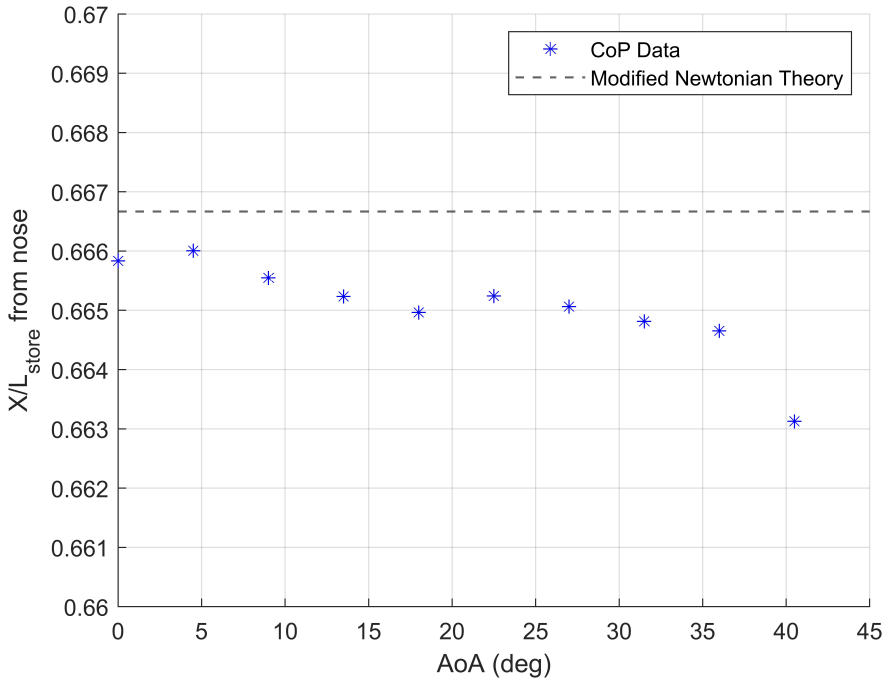

Figure 22: Center of Pressure Location for AoA Sweep: Specified Range

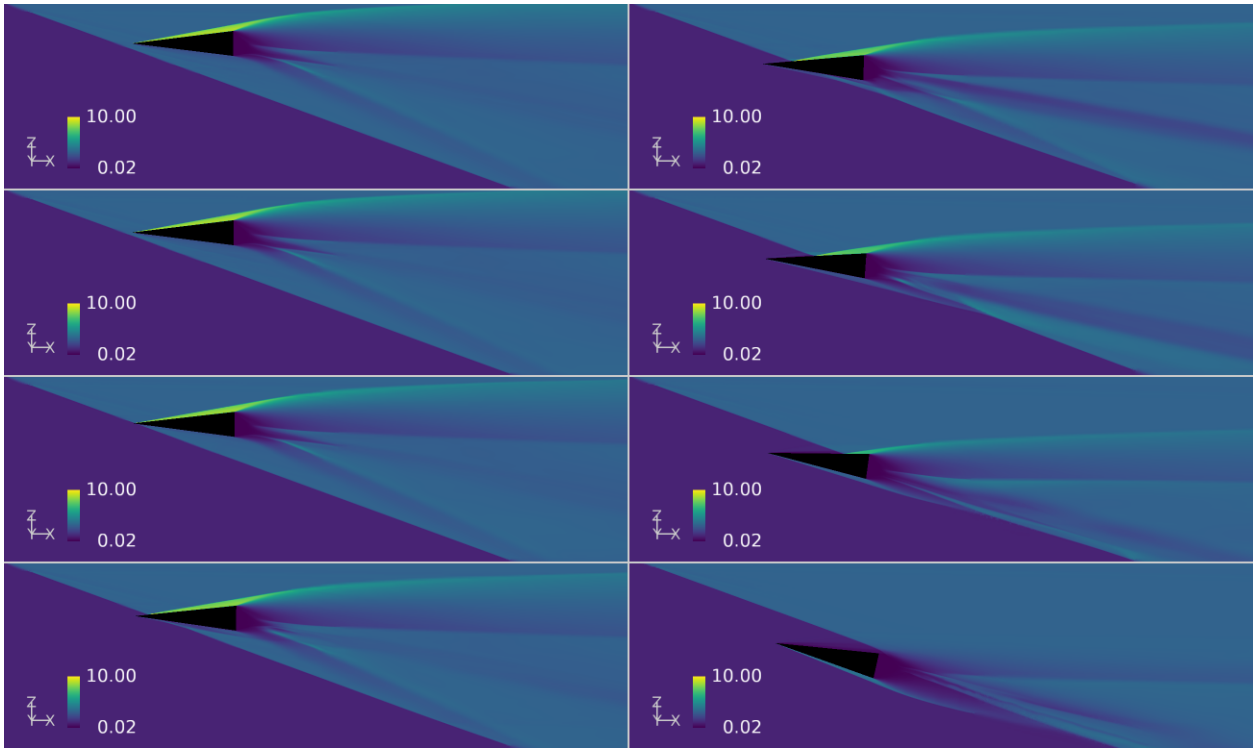

Figure 23: Instantaneous Normalized Density Sequence in $y = 0$ Plane

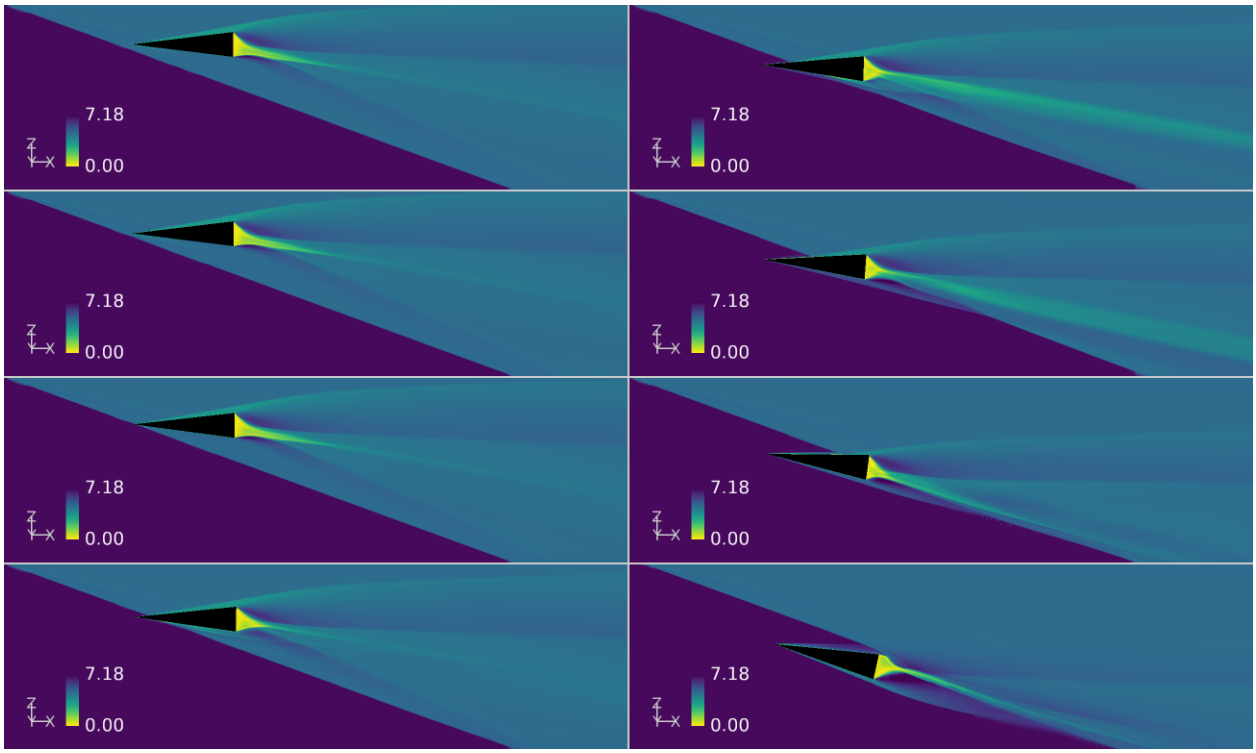

Figure 24: Instantaneous Mach Number Sequence in $y = 0$ Plane

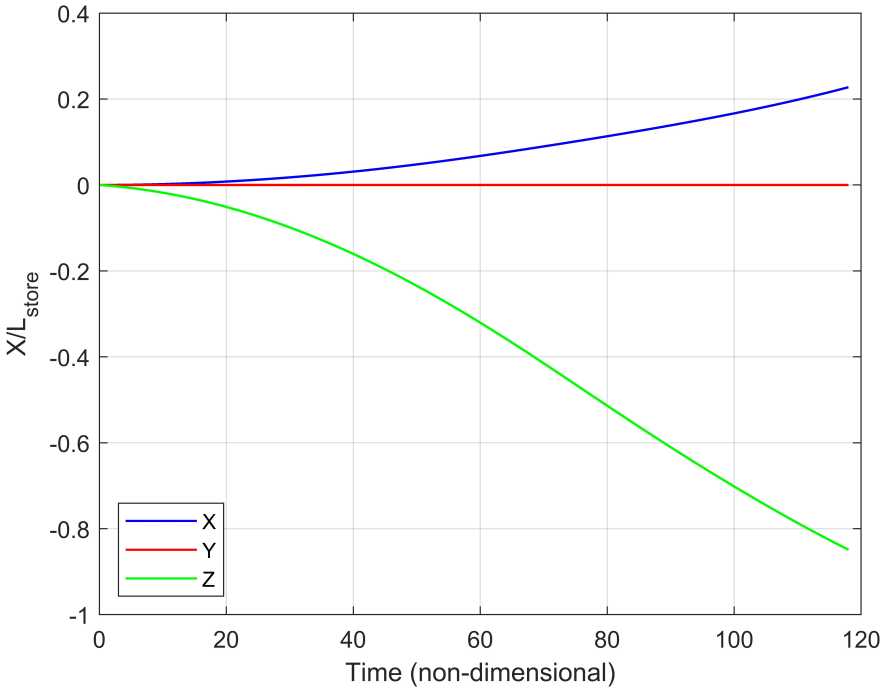

Figure 25: Dynamic Simulation CoG Location

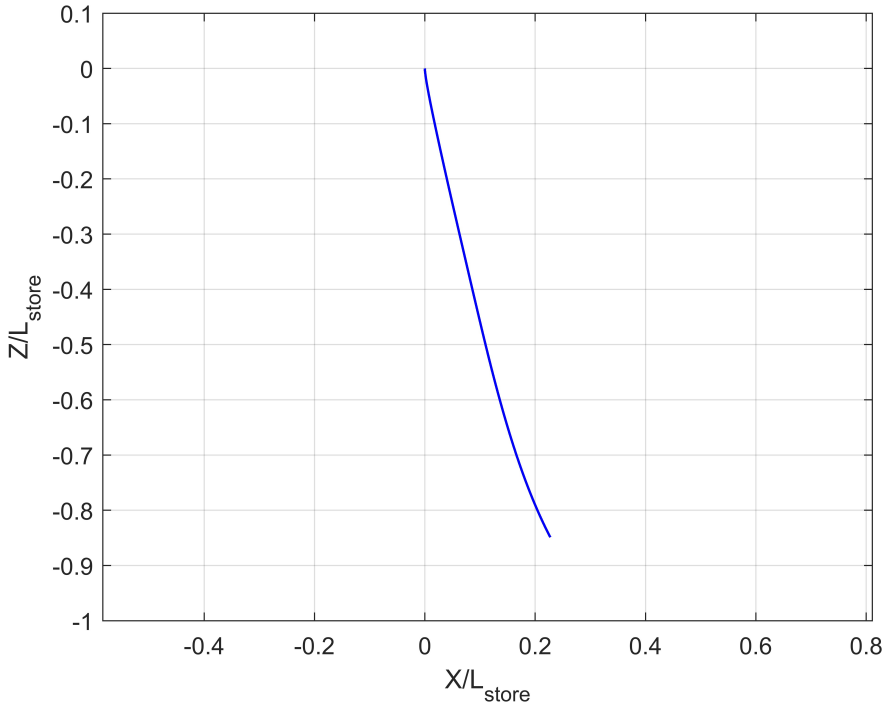

Figure 26: Dynamic Simulation CoG Trajectory

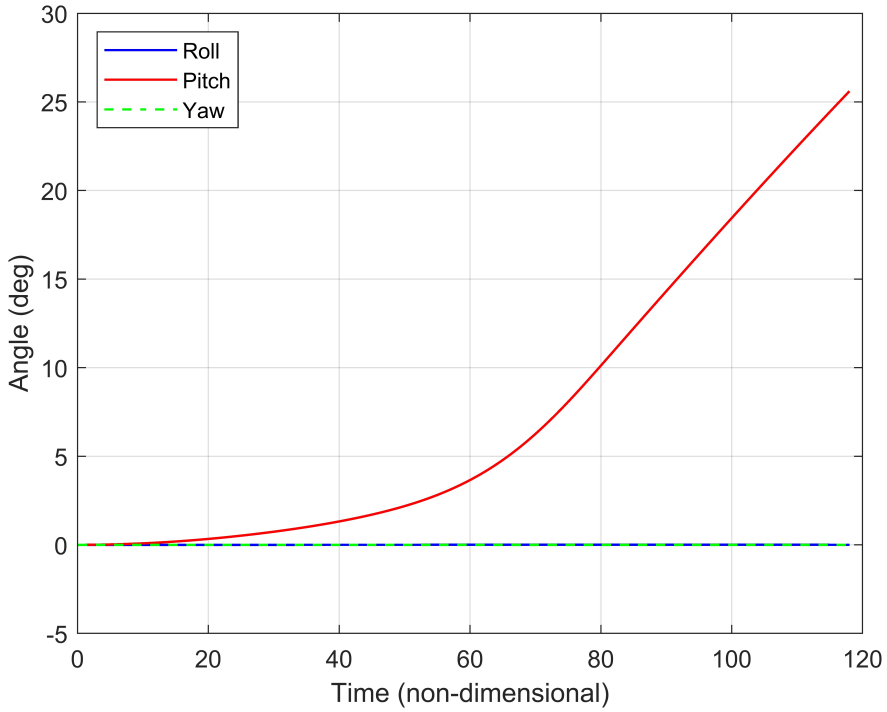

Figure 27: Dynamic Simulation Vehicle Attitude

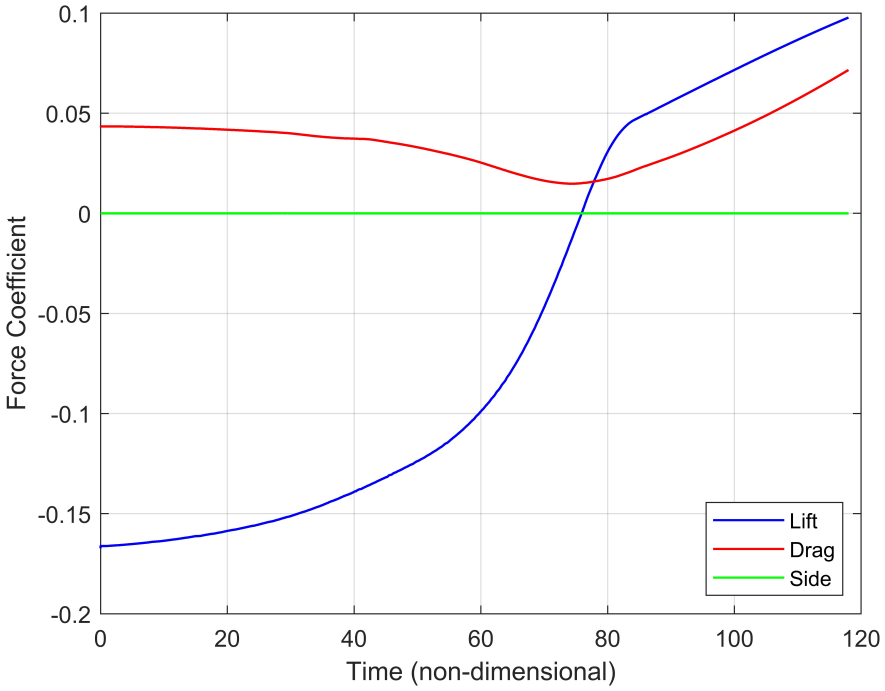

Figure 28: Dynamic Simulation Force Coefficients

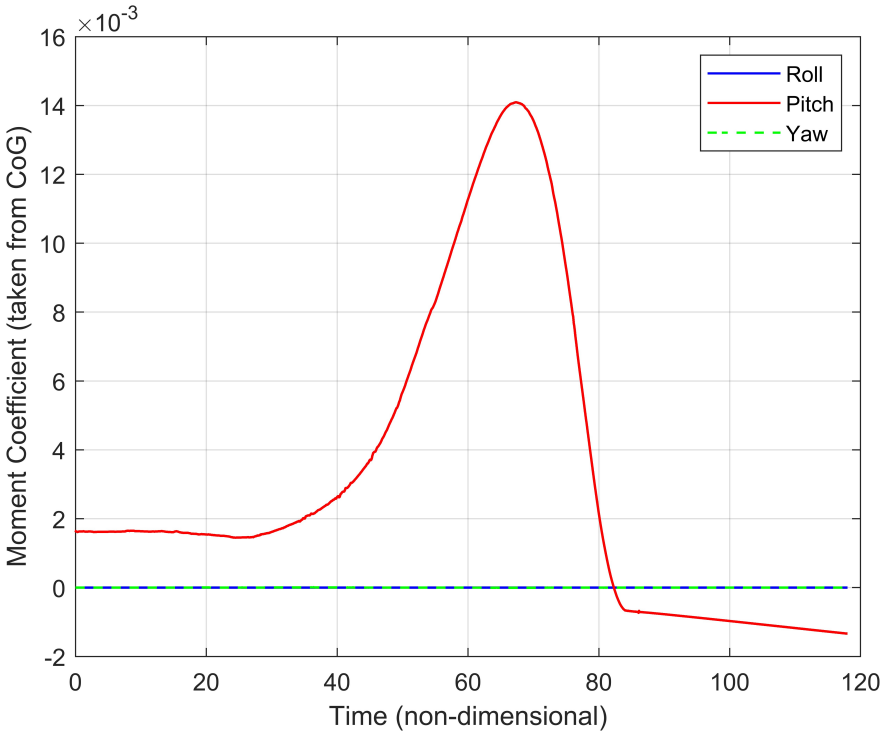

Figure 29: Dynamic Simulation Moment Coefficients

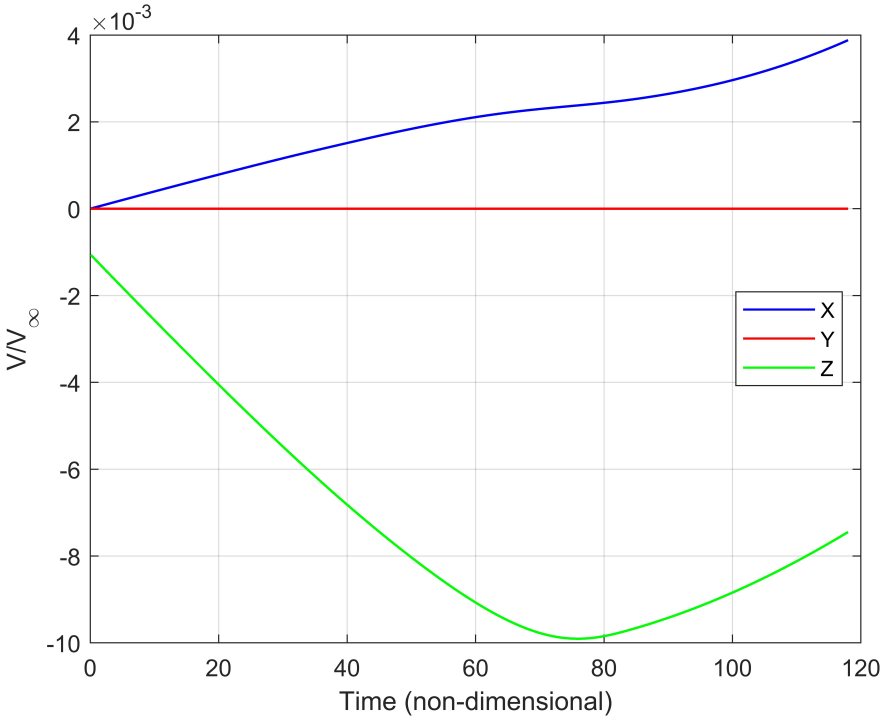

Figure 30: Dynamic Simulation CoG Velocity

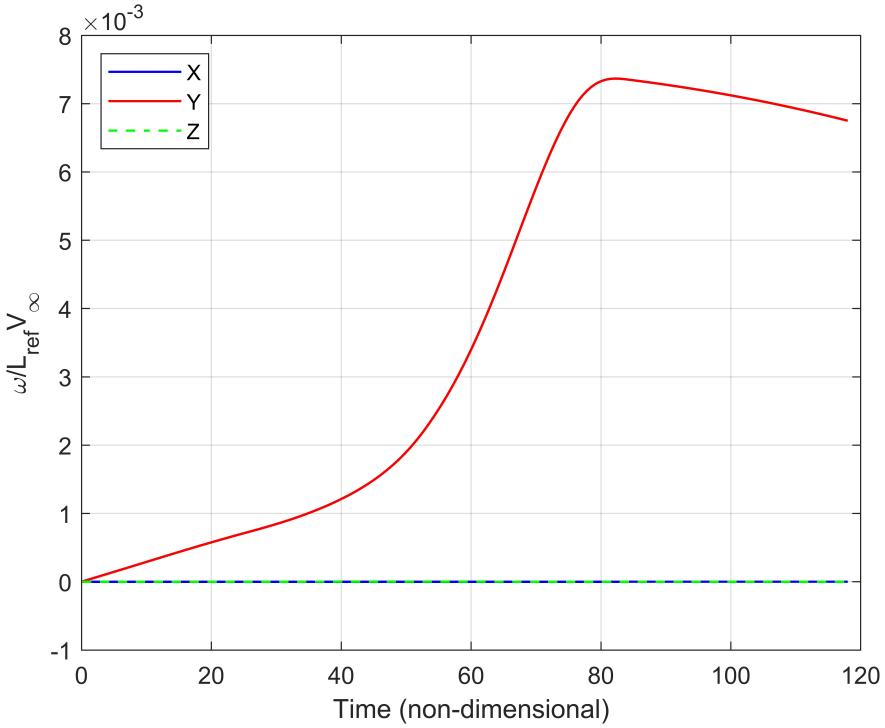

Figure 31: Dynamic Simulation Vehicle Angular Velocities

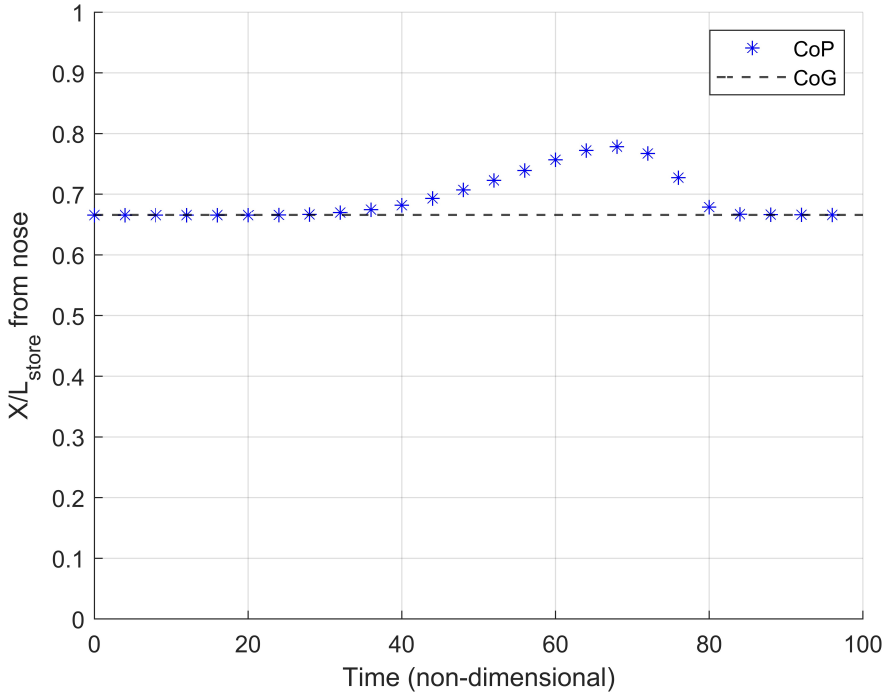

Figure 32: Dynamic Simulation Vehicle CoP

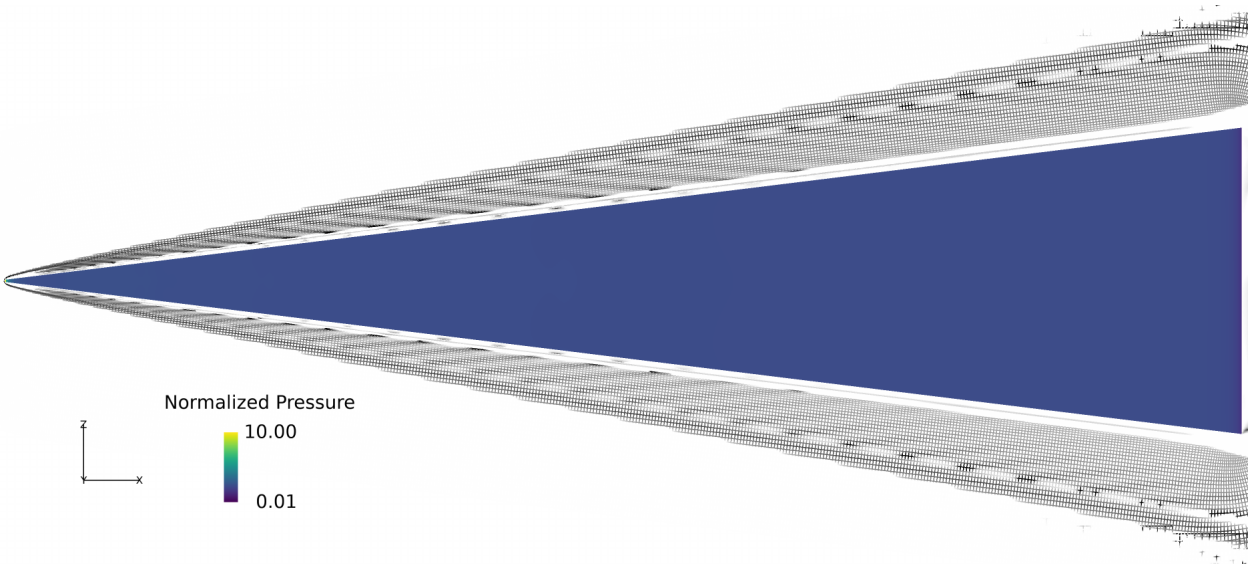

Figure 33: Static Simulation at 0° AoA: Normalized Surface Pressures and Shock Location

Table 3: RANS and DDES Force and Moment Coefficients

	RANS	DDES	Difference (%)
Lift Coefficient	-6.6636E-2	-6.6621E-2	0.2248
Drag Coefficient	1.7589E-2	1.7510E-2	0.4507
Pitch Moment Coefficient	1.4943E-2	1.4946E-2	0.0261
CoP (X/L from nose)	0.7790	0.7791	0.0951

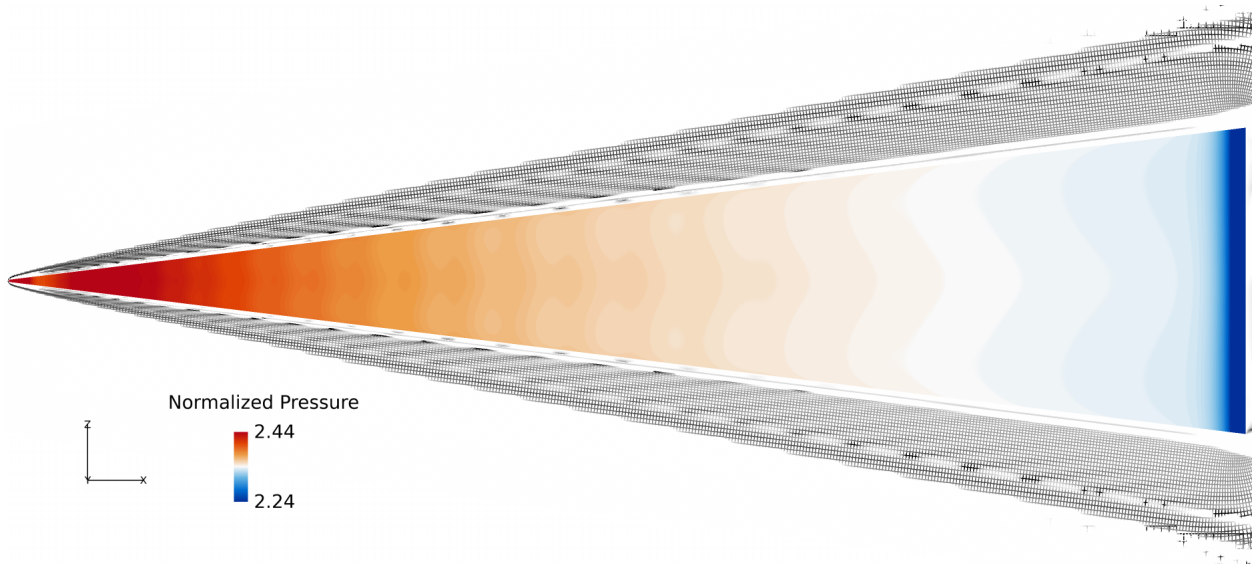

Figure 34: Static Simulation at 0° AoA: Specified Range of Normalized Surface Pressures and Shock Location

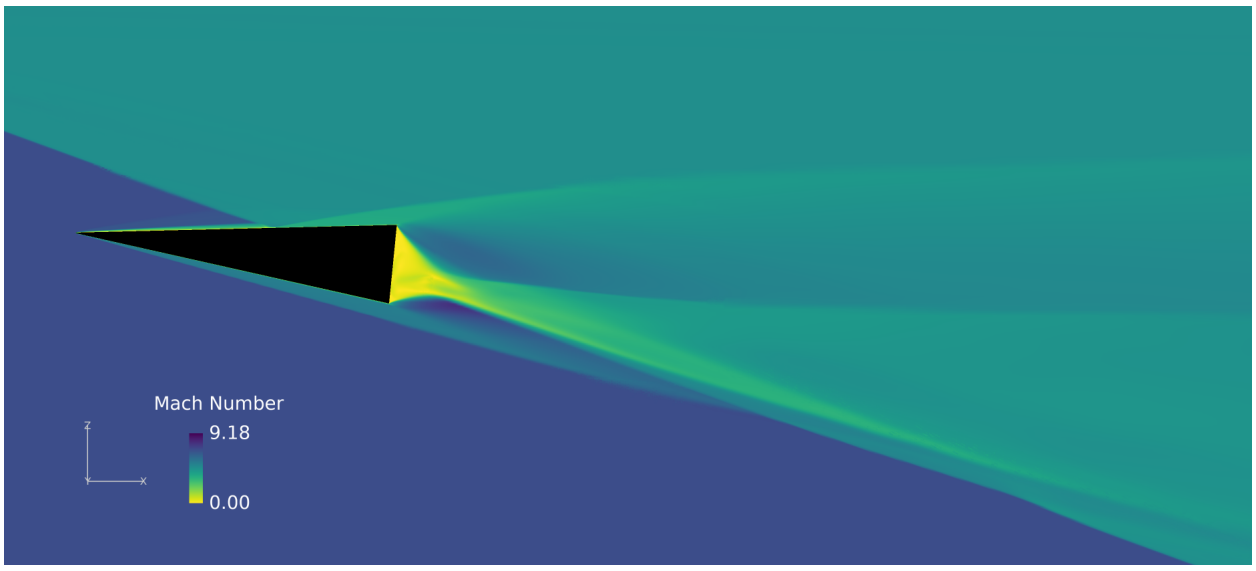

Figure 35: Instantaneous Mach Number in $y = 0$ Plane Showing Analysis Location

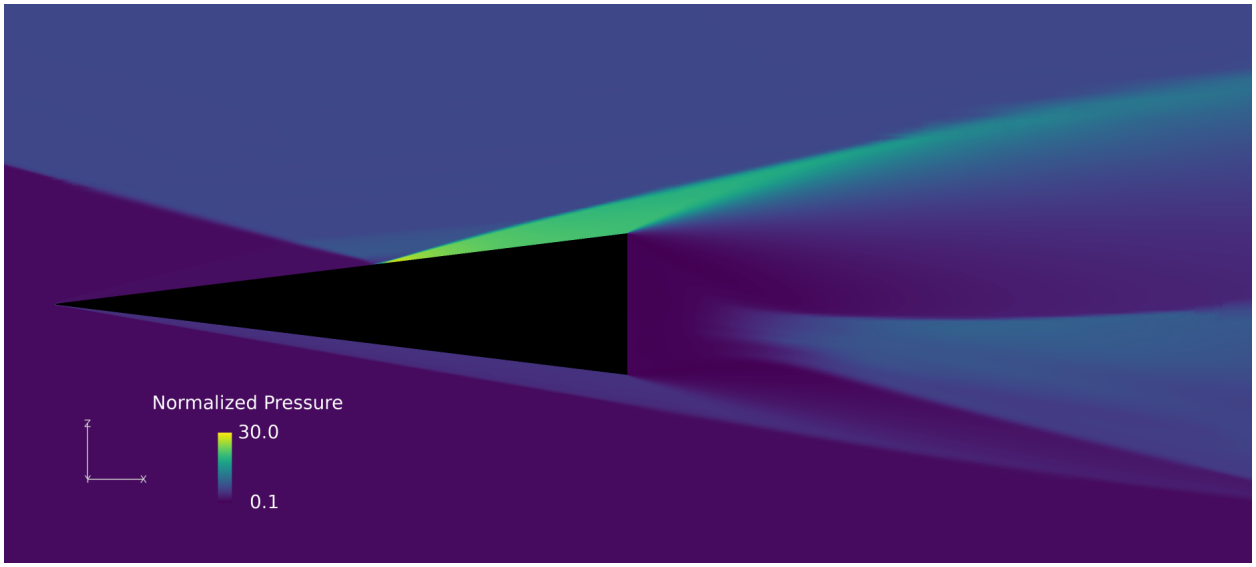

Figure 36: Instantaneous Normalized Surface Pressure

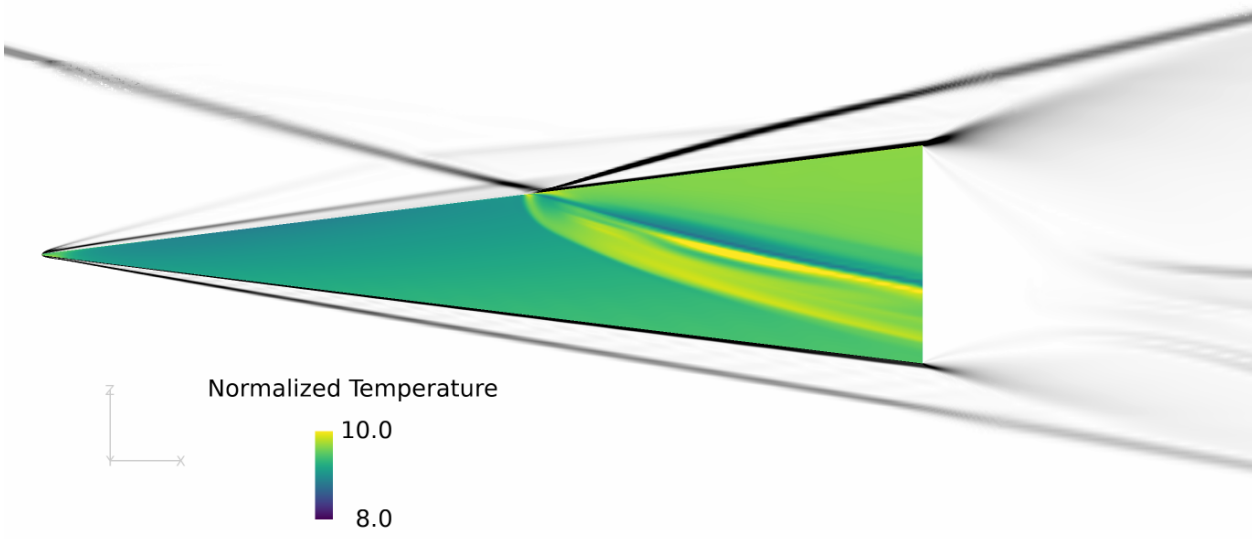

Figure 37: Instantaneous Normalized Surface Temperature

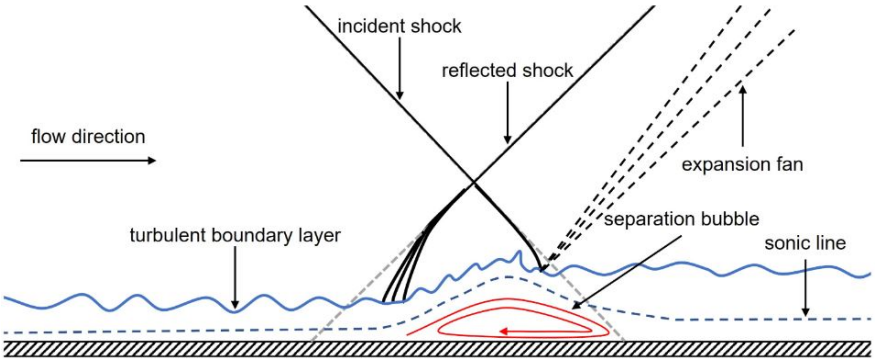

Figure 38: Oblique Shock Wave Boundary Flat Plate Boundary layer Interaction Structure [93]

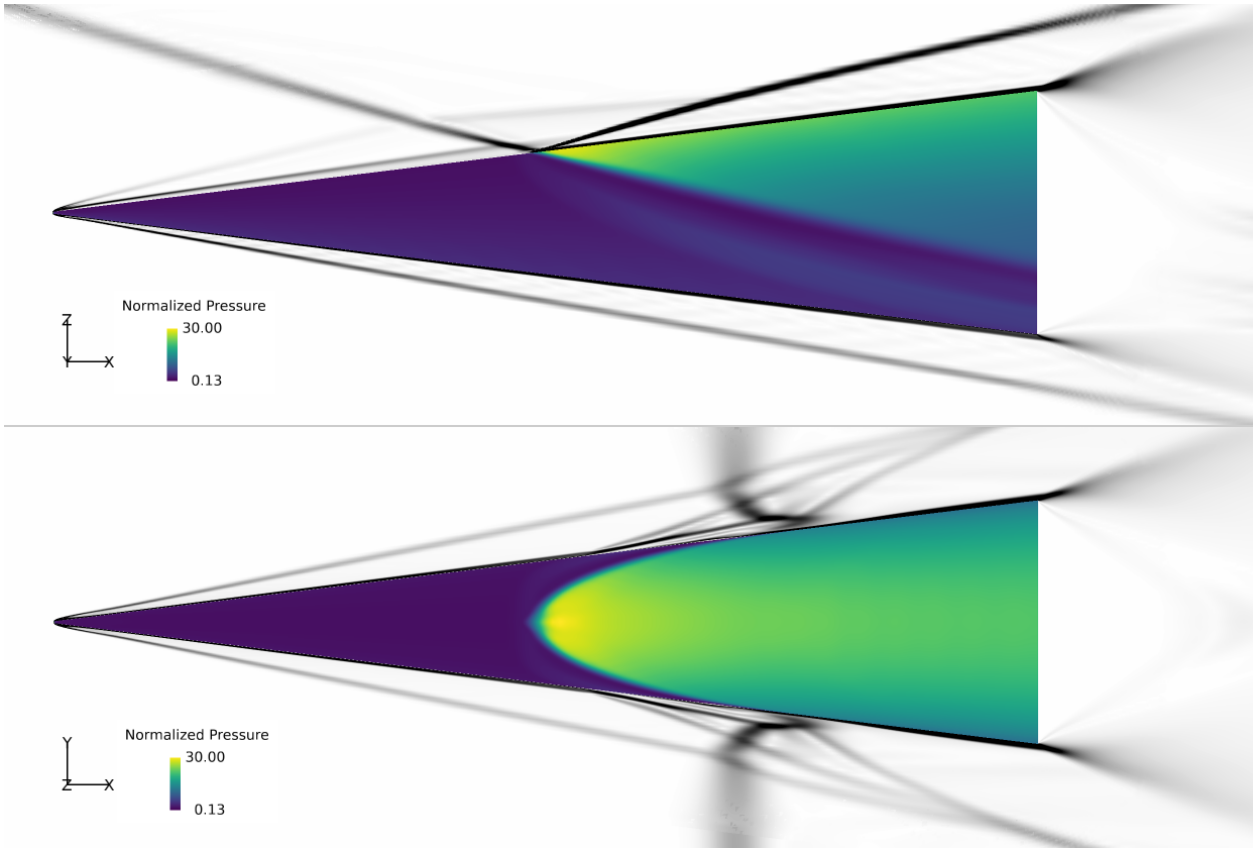

Figure 39: Instantaneous Normalized Surface Pressures and SBLI Structure in y and z planes

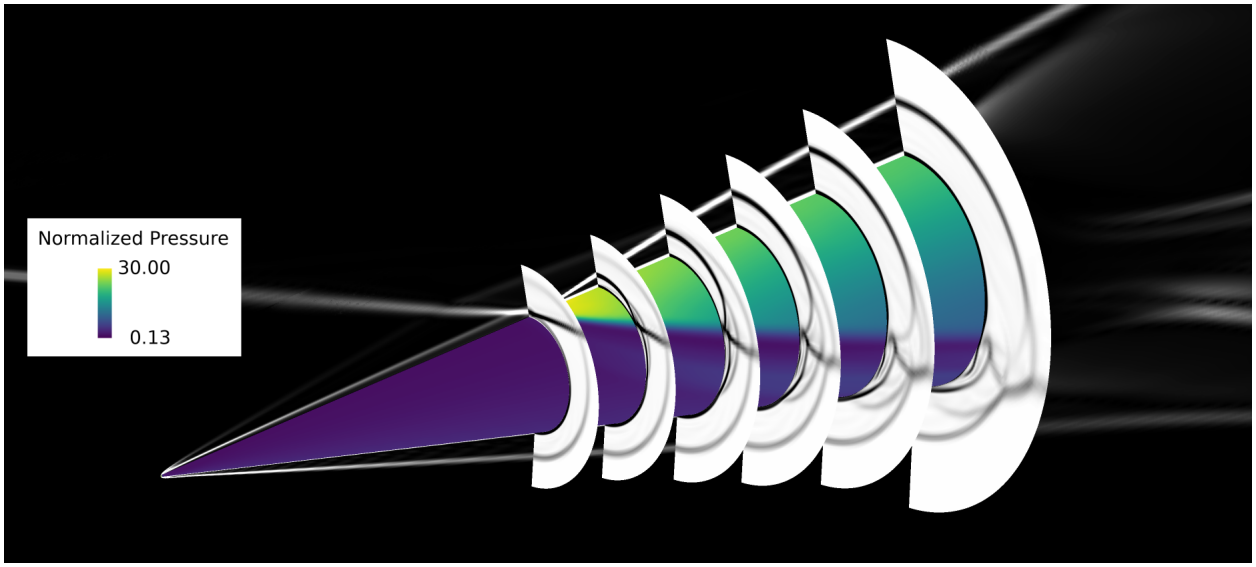

Figure 40: Instantaneous Normalized Surface Pressures and SBLI Structure Propagation Along the Store's Surface

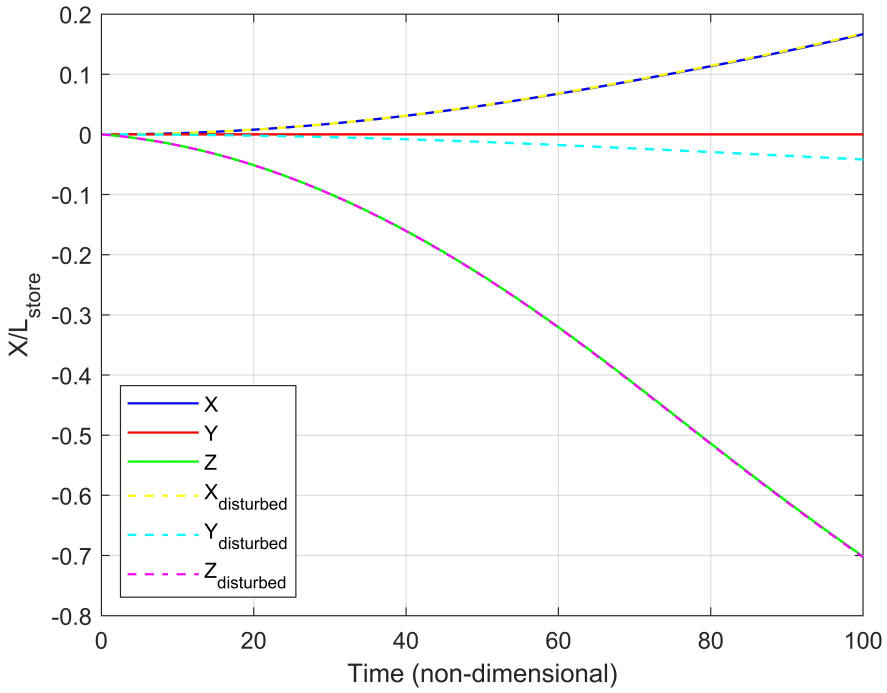

Figure 41: Center of Gravity Location for Sensitivity Analysis

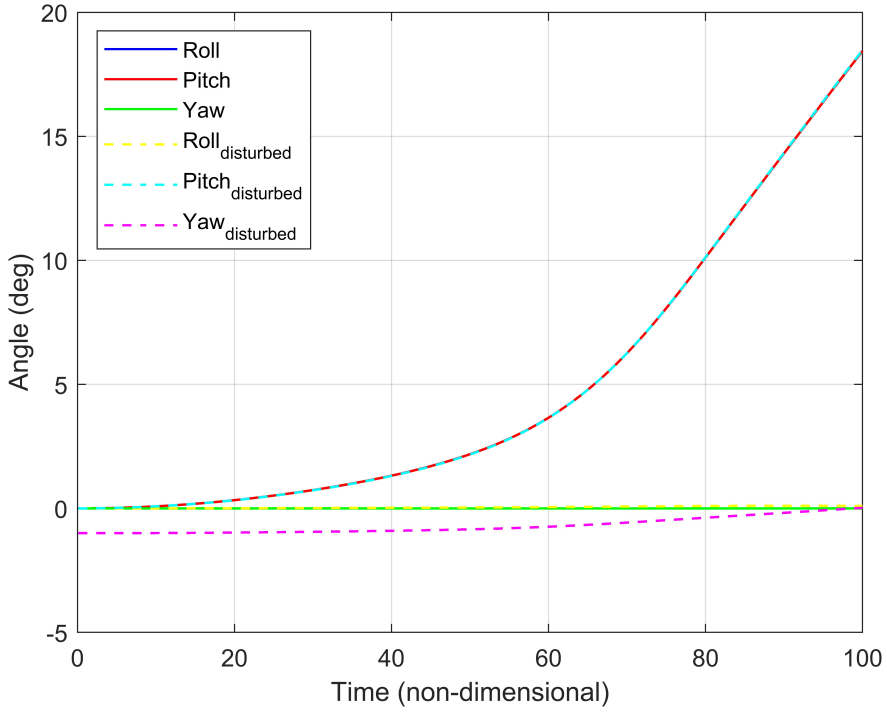

Figure 42: Store Attitude for Sensitivity Analysis

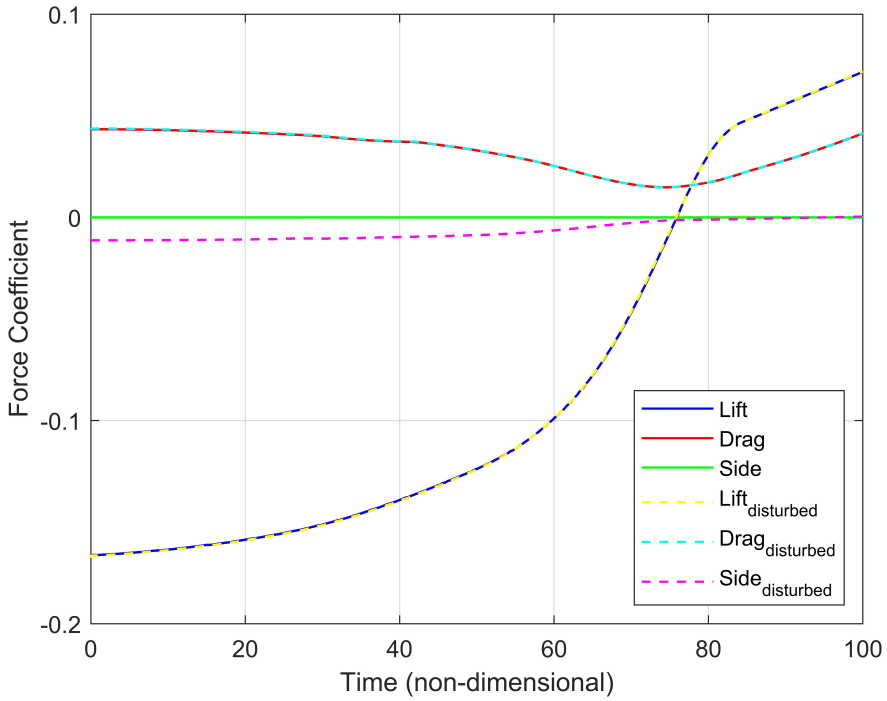

Figure 43: Force Coefficients for Sensitivity Analysis

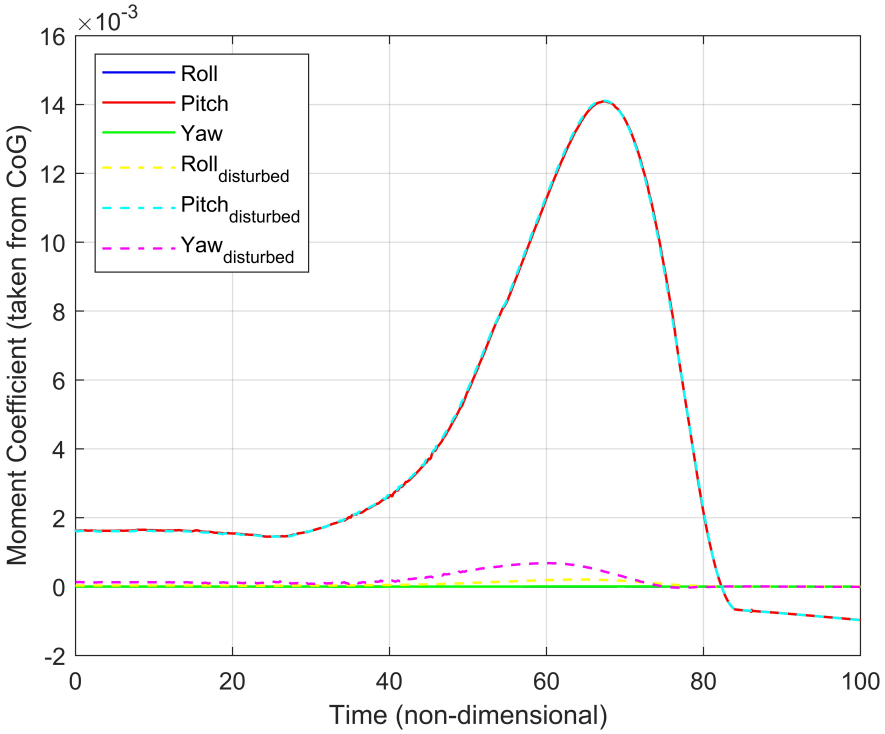

Figure 44: Moment Coefficients for Sensitivity Analysis

Vita

Ryan Savery was born in April of 1996 in Knoxville, Tennessee, where he would be raised and attend high school. He would go on to pursue his Bachelor's degree in Mechanical Engineering at The University of Tennessee, Knoxville, where his interest in aerospace related topics would start. After graduation, he traveled the United States for a year until landing at a company where he would preform guidance, navigation, and control research and development. He returned to The University of Tennessee in 2021 to pursue Aerospace Engineering, graduating in 2023 with a Master's of Science under his advisor Dr. James Coder. Outside of school, Ryan enjoys rock climbing, mountain biking, reading, and baking.